Structural and functional features of the C-terminal domain of ZnT8

Parsons, Douglas Scott

Awarding institution:
King's College London

Structural and functional features of the C-terminal domain of ZnT8

Douglas Parsons

King's College London

A thesis submitted in the fulfilment of the requirements for the degree of

Doctor of Philosophy

2019

I. Abstract

The correct compartmentalisation of cellular zinc is critical to its homeostasis in Eukarya. The vesicular subfamily of mammalian ZnTs mediates the transport of zinc from the cytosol into secretory vesicles in endocrine tissues and the brain. ZnT8 supplies the millimolar zinc concentrations of insulin granules in pancreatic β-cells, affecting insulin processing, crystallisation and secretion. In common with its bacterial homologue YiiP, ZnT8 is formed of a transmembrane and a cytosolic C-terminal domain (CTD). The mechanism of zinc transport in the bacterial proteins is well-described. While the transmembrane domain and the overall protein topology of the mammalian ZnTs is largely conserved from bacteria, there are significant differences in primary sequence in the metal-binding CTD. This domain has been shown to mediate protein-protein interactions in other mammalian ZnTs. A common mutation causing W325R in the CTD of ZnT8 increases the risk of developing type 2 and gestational diabetes, and affects autoantibody specificity in type 1 diabetes. This thesis details the purification and biophysical characterisation of the two common variants of the ZnT8 CTD. Both domains exhibit soluble recombinant protein expression in *Escherichia coli*. The domains form the ferredoxin-like fold elucidated for the bacterial homologues. Zinc binds to the conserved interface site and to the novel cysteine-rich tail, suggesting that there is a different zinc:protein stoichiometry than is found in the bacterial homologues. The cysteine motifs are conserved in the vesicular ZnTs and may represent a specific metal uptake strategy by this subfamily. The W325R mutation affects dimer formation and stability of the ZnT8 CTD. Dimer formation is not reliant on disulphide formation or divalent metal coordination. The data presented herein begin to provide a molecular basis for the different diabetes susceptibility caused by the full-length ZnT8 proteins.

II. Table of contents

III. List of figures

IV. List of tables

V. List of abbreviations

α2 Alpha helix 2

β2 Beta sheet 2

ΔCterm Missing some part of the C-terminal section

ε Extinction coefficient

λ_{max} Wavelength of maximal emission

τ Lifetime of the fluorophore

A Absorbance

AP-3 Adaptor protein 3

Apo Free of metal

ATP Adenosine triphosphate

BME Basal medium eagle vitamins

BSA Bovine serum albumin

CD Circular dichroism

CDF Cation diffusion facilitator

Cryo-EM Cryogenic electron microscopy

CTD C-terminal domain

DMSO Dimethyl sulfoxide

DTNB 5,5'-dithiobis-(2-nitrobenzoic acid)

DTT Dithiothreitol

EDTA Ethylenediaminetetraacetic acid

EMBL European Molecular Biology Laboratory

FRET Förster resonance energy transfer

GSIS Glucose-stimulated insulin secretion

GWAS Genome-wide association study

HEPES (4-(2-hydroxyethyl)-1-piperazineethanesulfonic acid)

HPLC	High performance liquid chromatography
HRP	Horseradish peroxidase
HSQC	Heteronuclear single quantum coherence
ICP-MS	Inductively coupled plasma-mass spectrometry
IL	Intracellular loop
Ins	Insoluble
IPTG	Isopropyl β-D-1-thiogalactopyranoside
ITC	Isothermal titration calorimetry
k	Bimolecular quenching rate constant
K_d	Dissociation constant
kDa	Kilodaltons
K_m	Michaelis constant
K_{Me}	Affinity constant for metal
K_{sv}	Stern-Volmer constant
LB	Lysogeny broth
MST	Microscale thermophoresis
MTF-1	Metal-response element-binding transcription factor 1
MW	Molecular weight
nDSF	Nano differential scanning fluorimetry
NI	Not induced
NMR	Nuclear magnetic resonance
NTD	N-terminal domain
PAGE	Polyacrylamide gel electrophoresis
PBS	Phosphate buffered saline
PDB	Protein Data Bank
pK	Stability constant

pK_a	Acid dissociation constant
PMSF	Phenylmethylsulphonyl fluoride
ppm	Parts per million
PVDF	Polyvinylidene difluoride
Q	Quencher
Q-ToF	Quadrupole time-of-flight
R325	ZnT8 expressing arginine at position 325
ROS	Reactive oxygen species
S	Soluble
S^-	Deprotonated sulfyhdryl
SDS	Sodium dodecyl sulphate
Sol	Soluble
TBS-T	Tris buffered saline containing 0.1% (v/v) Tween-20
TCEP	Tris (2-carboxyethyl)phosphine hydrochloride
TEV	Tobacco etch virus
TFA	Trifluoroacetic acid
TM	Transmembrane helix
TMD	Transmembrane domain
TNB	2-nitro-5-thiobenzoate
TNZD	Transient neonatal zinc deficiency
UV	Ultraviolet
v/v	Volume per volume
w/v	Weight per volume
W325	ZnT8 expressing tryptophan at position 325
W325R	Mutation in ZnT8 encoding tryptophan replacing arginine at position 325
WELQ	‘WELQ protease’ cleavage recognition site

ZIP	Zrt- Irt-like protein (gene *SLC39A*)
ZnT	Mammalian zinc transporter family (gene *SLC30A*)
ZnT8	Member 8 of the ZnT family
ZnT8c	C-terminal domain of ZnT8 (residues 267 - 369)
ZnT8cR	C-terminal domain of ZnT8 expressing arginine at position 325
ZnT8cW	C-terminal domain of ZnT8 expressing tryptophan at position 325

VI. Acknowledgements

First and foremost I must thank my supervisors Wolfgang Maret and Christer Hogstrand. Thank you for believing in me and helping me to grow into a decent scientist. In particular, thank you Wolfgang for your constant support and advice - working with you and feeling your passion for learning has made me sure that I want to pursue a career in science. You both should know that I am extremely proud to have graduated from your lab and my career will be all the better for it.

I may not have stayed the course if it were not for those with me in the lab every day; Elisa, Sabine and Elisabeth each made my life easier and better in their own inimitable ways. A special thanks must go to Dr. Song, who brightened up my day every time I saw her.

1. General Introduction

1.1 Zinc homeostasis

Zinc is an essential element for all forms of life. Originally identified as indispensable in fungi in 1869 (Raulin, 1869), and rats in 1934 (Todd et al., 1934), it was not until 1961 that the drastic developmental effects of severe zinc deficiency in humans would be described (Prasad et al., 1961). Speaking to its myriad important roles in the body, even mild zinc deficiency has detrimental consequences for many aspects of human health (Rink, 2011). Zinc deficiency of varying severity is purported to currently affect two billion humans worldwide (Prasad, 2013).

Zinc is the second most abundant 'trace' metal in the human body after iron, with an average 70 kg human containing 2-3 g of zinc (Wastney et al., 1986). The majority of this zinc is stored within the skeletal muscle (~60%), while other major stores are bone (~30%), liver (~5%) and skin (~5%), with the remainder distributed to other tissues such as brain, pancreas and kidney (Jackson, 1989). Only ~0.1% of the body's zinc is contained within the plasma, where it is bound by albumin (~80%) and α2-macroglobulin (~20%) (Barnett et al., 2013). Dietary zinc absorption is regulated by the duodenum and jejunum (Steel & Cousins, 1985), while excretion of excess zinc is achieved through gastrointestinal secretion, sloughing of mucosal cells and integument, and renal excretion (Hambidge & Krebs, 2002). Zinc nutriture is dependent on the quantity and bioavailability of zinc in food (Maret & Sandstead, 2006). Foods rich in zinc include red meat and pulses, while cereals containing non-digestible plant ligands such as phytate reduce zinc availability (Sandstead & Smith, 2018). Zinc deficiency can be caused by insufficient dietary intake and/or as a secondary symptom of diseases which impair either intestinal control of zinc uptake, for example in acrodermatitis enteropathica or cystic fibrosis (McClain, 1985), or intestinal release, for example in inflammatory bowel diseases such as Crohn's disease (Solomons et al., 1977).

Zinc deficiency can manifest in various symptoms. The first described cases of severe zinc deficiency in humans were of Iranian adolescents suffering from dwarfism, hypogonadism, poor appetite, mental lethargy and rough skin, all of which were alleviated upon zinc supplementation (Prasad et al., 1963). Due to its proliferative nature, the immune system is particularly susceptible to zinc deficiency (Prasad, 2013). Zinc regulates several crucial processes in innate immunity, including phagocytosis, intracellular killing and cytokine production, while in the adaptive immune system, zinc deficiency results in reduced T cell development and function and B cell antibody production (Maywald et al., 2017). Other symptoms can include impaired brain function (Sandstead et al., 1998) and poor pregnancy outcomes (Goldenberg et al., 1995). Zinc supplementation is effectively used to treat acrodermatitis enteropathica and Wilson's disease (to prevent tissue copper overload) and is important to reduce the mortality of diarrhea and pneumonia (Maret & Sandstead, 2006). Zinc excess or toxicity is rarely described in humans, however incidents of zinc poisoning resulted in nausea, vomiting and diarrhea (Brown et al., 1964). However, zinc supplementation must be accompanied by copper, otherwise the excess zinc can lead to copper deficiency (Sandstead, 1995).

Unlike iron or copper, zinc is redox inert and is a Lewis acid (Williams, 1987). These properties are integral to zinc having structural and catalytic roles in proteins, and cellular signalling functions (Maret, 2013; Maret & Li, 2009). Confirmation as a structural cofactor in proteins came in 1938 when insulin was crystallised with zinc (Scott & Fisher, 1938), while the first catalytic function of zinc was described for carbonic anhydrase in 1939 (Keilin & Mann, 1939). Zinc has since been shown to be a cofactor in all six enzyme classes (Vallee & Falchuk, 1993). The identification of zinc-binding residue repeats in *Xenopus laevis* transcription factor TFIIIA (Miller et al., 1985), i.e. the zinc-finger motif, laid the foundation to search genomes for zinc proteins. Zinc proteins make up 4-5% of bacterial and archaeal proteomes (Andreini et al., 2006b), with the proportion correlating with organism complexity; at least 10% of the human proteome is comprised of zinc proteins (Andreini et al., 2006a).

Another property of zinc critical for its biochemistry is the relative stability formed by zinc complexes, as described by the Irving-Williams series of transition divalent metal ions (Irving & Williams, 1948): Mn < Fe < Co < Ni < Cu > Zn. This series indicates that complexes formed by zinc are second only to copper(II) in their strength. The high affinity of structural and catalytic protein-zinc complexes is one of the reasons for the large disparity between cellular total and free zinc; while the average total cellular zinc content is hundreds of micromolar, the free cytosolic zinc concentration is approximately picomolar (Krężel & Maret, 2006, 2016). The total and free zinc concentrations vary between tissues, cells and organelles. For instance, elevated zinc levels are typically found in endocrine tissues such as the prostate and pancreas (Franklin, 2007; Zalewski et al., 1994). In the pancreas, zinc is concentrated in β-cells, in which insulin secretory vesicles contain total zinc concentrations of approximately 20 mM (Foster et al., 1993). The free zinc in these vesicles has been measured as between 1-100 µM (Vinkenborg et al., 2009), whereas the free zinc in the endoplasmic reticulum (ER) and Golgi of HeLa cells, for instance, is 0.9 and 0.6 pM respectively (Qin et al., 2011), although absolute measurements of such low concentrations must be interpreted carefully (Maret, 2015). The tight control of cytosolic zinc(II) ion concentrations in mammalian cells underpins the significance of zinc as a signalling ion akin to calcium and magnesium (Maret, 2017). For instance, the inhibition of protein tyrosine phosphatase PTP1B by zinc with picomolar to nanomolar affinity is purportedly caused by specific spatiotemporal zinc signals (Bellomo et al., 2014). For zinc signals to exist, the background free zinc must be tightly controlled.

Cells have three main tools for regulating zinc homeostasis: zinc-binding proteins, zinc sensors, and zinc transporters. The critical function of this repertoire is to be able to deal with both long and short-term zinc stimuli (Maret, 2009). For instance, long term stimuli such as culturing cells in zinc-rich medium will cause sensor proteins to become activated and upregulate the expression of efflux transporters and zinc binding proteins. Short term stimuli such as the release

of zinc from an intracellular store, for example the ER, will be buffered by cytosolic zinc binding proteins, such as metallothioneins.

Metallothioneins are small, cysteine-rich cytosolic proteins (Vašák & Meloni, 2011). Mammalian metallothioneins can bind up to seven zinc(II) ions with differing affinity, linking the zinc occupancy of metallothionein with the zinc status of the cell; during cytosolic zinc deficiency the zinc bound to low affinity sites in metallothionein will become displaced and available, whereas during high cytosolic zinc concentrations, zinc will occupy these low affinity sites, reducing the cytosolic free zinc (Krężel & Maret, 2007). Therefore, a major cytosolic store of zinc is bound by cysteine residues, meaning that cellular zinc homeostasis is inextricably linked to the redox state of the cell (Maret, 2009), despite zinc itself being redox neutral.

The expression of metallothioneins and other zinc homeostatic proteins is driven by metal responsive sensors and transcription factors. The expression of such bacterial metal sensor protein pairs, and the subsequent metal buffering, shows that the free cytosolic concentrations of transition metals mirrors that of the Irving-Williams series (Fig. 1.1), with only copper having lower free concentrations than zinc (Reyes-Caballero et al., 2011). For example, the *Escherichia coli* zinc sensor Zur is a repressor in its zinc-bound form (Patzer & Hantke, 1998). When free zinc concentrations drop below a threshold, zinc dissociates from Zur, preventing Zur binding to its target gene *ZnuABC,* and thus promoting the expression of uptake transporters and other proteins which reduce the zinc requirement of the bacterium (Outten & O'Halloran, 2001). Conversely, the zinc sensor ZntR binds to its target gene *zntA* in its zinc-bound form and promotes the expression of efflux transporters and metal binding proteins to protect the cell from zinc excess (Outten et al., 1999). The effect is that cellular free zinc levels, and the free concentrations of other metals, are buffered in a range dictated by the affinity of these sensors for the metals (Fig. 1.1). In addition to their roles being defined by affinity, some metal sensors are regulated through allostery; while a more abundant metal ion may bind, only the correct ion will bind optimally and allow DNA binding (Waldron et al., 2009). In *Saccharomyces cerevisiae*

the zinc excess sensor Zap1 acts as a repressor upon zinc binding (Rutherford & Bird, 2004). Such sensing systems are less well described in plants, however the transcription factors bZIP19 and bZIP23 have been identified as regulating zinc uptake transporters in *Arabidopsis thaliana* (Assuncao et al., 2010).

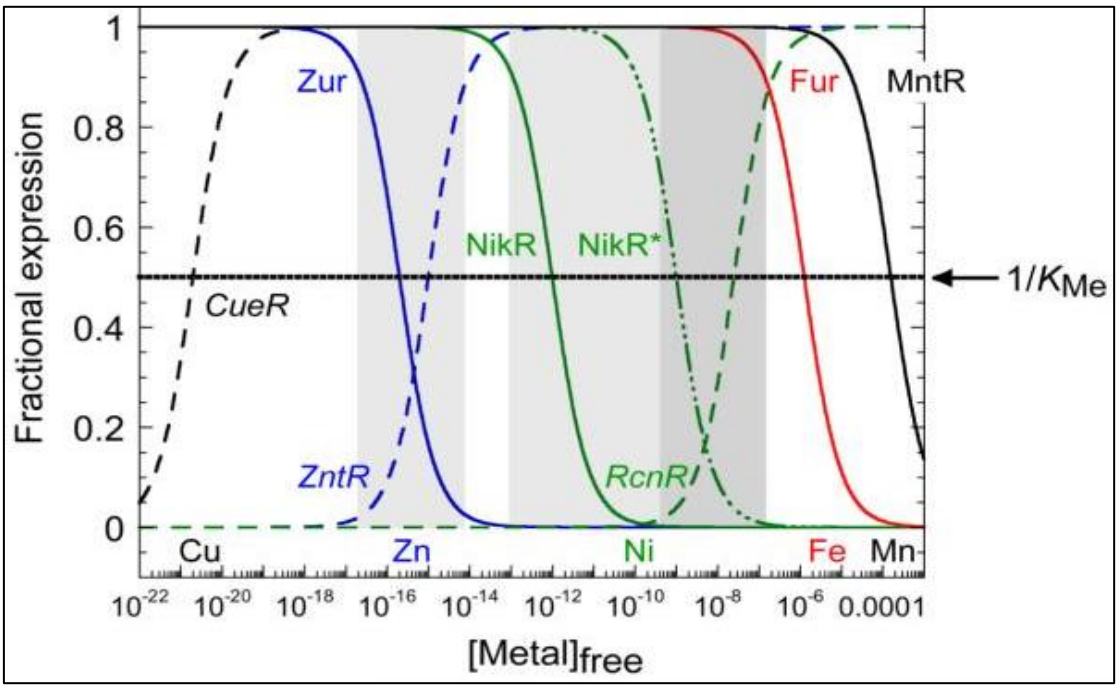

Figure 1.1. Cytosolic free metal buffering by metal sensor proteins. Fractional expression of *E. coli* metal sensors is dependent on the concentrations of free metal ions and thus dictate their buffered ranges (grey areas). The functions of the sensors are inextricably linked to their dissociation constants for the metals ($1/K_{Me}$). For zinc, the sensor Zur is a repressor in its zinc-bound form, and so its target gene *ZnuABC* only becomes activated at low zinc concentrations. When activated, *ZnuABC* expresses cellular uptake machinery. Conversely, ZntR is inactive in its apo-form, and therefore binds to its target gene *zntA* at higher zinc concentrations. Activated *zntA* expresses efflux machinery and metal binding proteins. Figure modified from (Reyes-Caballero et al., 2011).

The only zinc(II) sensor identified in animals to date is metal-response element-binding transcription factor 1 (MTF-1) (Laity & Andrews, 2007). Deletion of MTF-1 is embryonically lethal in mice (Günes et al., 1998). MTF-1 typically acts as a transcriptional activator in its zinc-bound state, binding to the metal response element (MRE) in target genes expressing zinc excess

machinery (Li et al., 2006). The affinity of purified MTF-1 for zinc is approximately 31 pM (Guerrerio & Berg, 2004). The only direct targets of MTF-1 identified to date are *SLC30A1*, encoding the ubiquitous zinc exporter ZnT1, and genes encoding metallothioneins (Radtke et al., 1993). In Eukarya, response to cellular metal level also occurs post-transcriptionally, such as adjusting mRNA stability or translation, and post-translationally, such as modulation of protein trafficking or degradation (Waldron et al., 2009). It has been proposed that MTF-1 heads a direct and indirect hierarchy of zinc sensors through control of its target genes (and their downstream effects), although much remains to be discovered about the mechanisms of such regulation (Hardyman et al., 2016).

The third set of tools available to cells for zinc homeostasis are transporters, which enable the flux of zinc and other metals across biological membranes (Nies, 2007). There are several different families of transporters split into two groups, mediating transport into and out of the cytosol, although some transporters have been reported as bidirectional (Valentine et al., 2007). Families of zinc efflux transporters include RND transporters in bacteria, P-type ATPases in bacteria and plants, and cation diffusion facilitators (CDFs), which are ubiquitous to all forms of life (Blindauer, 2015). Zinc influx transporters include ABC transporters and TonB-dependent receptors in bacteria, and Zrt/Irt-like proteins (ZIP), which are also ubiquitous to all forms of life. These protein families have significant structural differences, but most zinc transporters that have been studied are either primary or secondary active transporters, driven by ATP hydrolysis or electrochemical gradients (Blindauer, 2015), meaning that zinc is typically transported against a concentration gradient. The ZIPs appear to be an exception, as the bacterial ZIPB functions as a Zn^{2+} selective channel, through which extracellular Zn^{2+} diffuses into the tightly controlled intracellular lumen (Wei Lin et al., 2010).

While bacteria and plants express several different zinc transporter families, mammals are limited to CDF exporters and ZIP importers (Blindauer, 2015). However, there is a large degree of specialisation in mammals, with 14 ZIPs (gene family *SLC39A*) and 10 CDFs (*SLC30A*; known as

ZnTs in mammals) in humans that have specific tissue and intracellular localisations (Kambe et al., 2015). In common with ZnTs, there is no 3D structure of a mammalian ZIP, indeed there is no 3D structure of any full-length ZIP protein from any organism. However, the structure of the large extracellular domain of a mammalian ZIP4 has recently been elucidated (Tuo Zhang et al., 2016). This thesis will predominantly focus on CDF/ZnT proteins.

The CDF family is split into three major clades which reflect their substrate specificity; Mn-CDF, Fe/Zn-CDF and Zn-CDF (Montanini et al., 2007). Examples of bacterial Zn-CDFs include *E. coli* ZitB, which confers zinc resistance to zinc-sensitive *E. coli* (Grass et al., 2001), *Ralstonia metallidurans* CzcD, which mediates the efflux of cobalt, cadmium and zinc (Anton et al., 1999), and *Thermus thermophilus* CzrB, which effluxes cadmium and zinc (Spada et al., 2002). The only elucidated 3D structure of a full length CDF is that of the Fe/Zn-CDF *E. coli* YiiP (also known as FieF) (Lu & Fu, 2007). The current structural and mechanistic models applied to the mammalian ZnTs are based on the elucidated properties of *E. coli* YiiP.

1.2 CDF structure

E. coli YiiP is formed of a transmembrane domain (TMD) consisting of six helices connected by loops of varying length, and a C-terminal domain (CTD) which forms a conserved ferredoxin fold (Fig. 1.2A; Lu and Fu 2007). YiiP is an integral cytoplasmic membrane protein in *E. coli*, and functions as a homodimer to export zinc(II) ions from the cytoplasm into the periplasmic space (Lu et al., 2009).

A

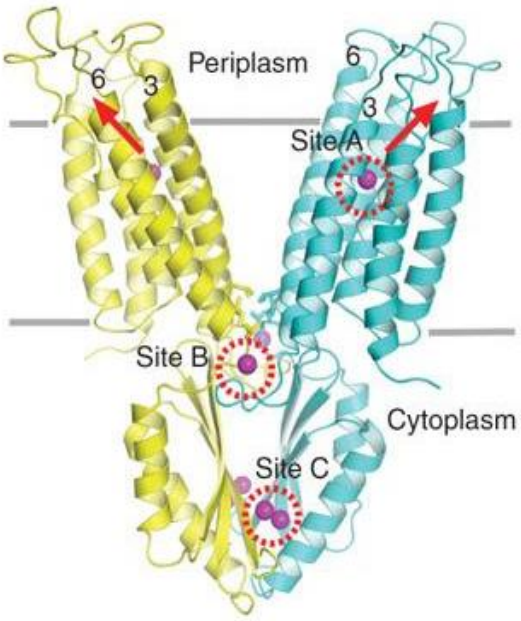
Periplasm
6
3
6
3
Site A
Site B
Cytoplasm
Site C

B

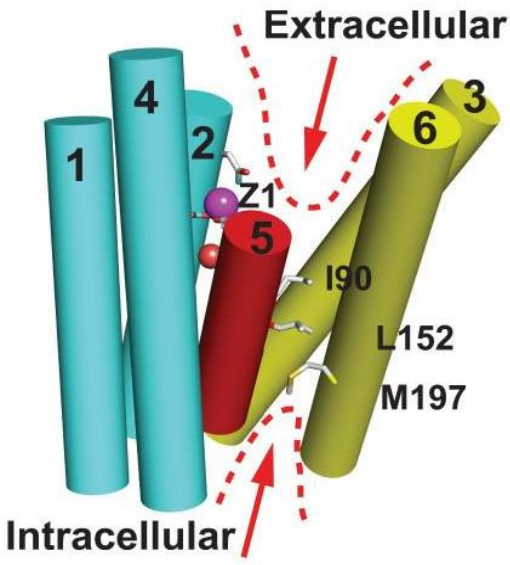
Extracellular
4
1
2
3
6
Z1
5
I90
L152
M197
Intracellular

C

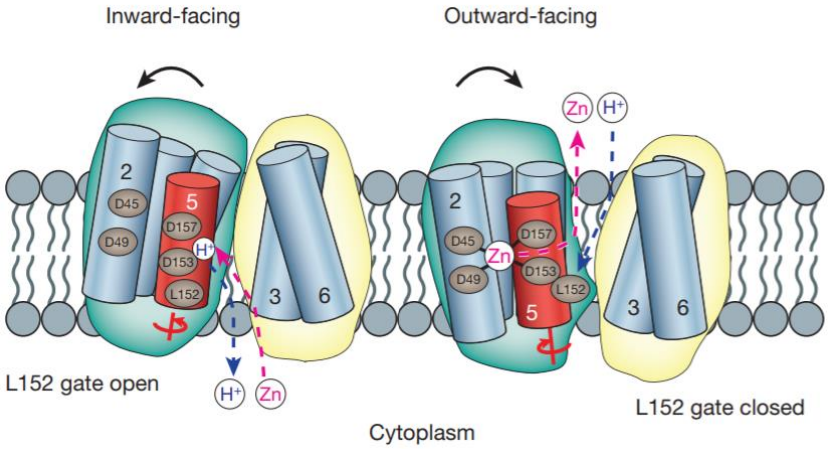
Inward-facing
Outward-facing
2
D45
D49
5
D157
D153
L152
H+
3
6
Zn
H+
L152 gate open
H+
Zn
Cytoplasm
L152 gate closed

D

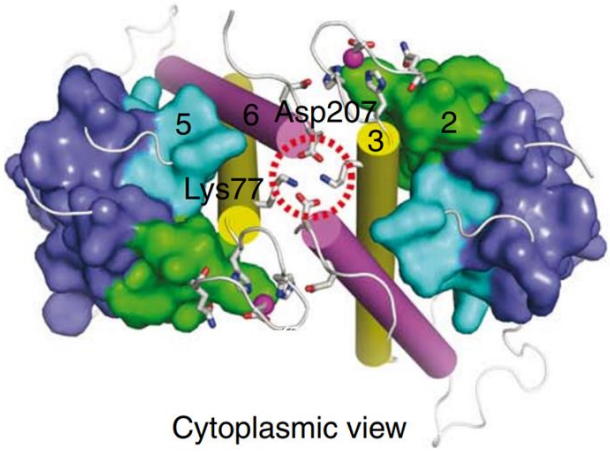

Figure 1.2. 3D structure and zinc binding sites of *E. coli* YiiP. *A*, each YiiP monomer binds four zinc ions, one in the transport site (Site A), one in the hinge region (Site B) and two in a binuclear site in the CTD (Site C). Red arrows indicate movement of the zinc(II) ions into the periplasm during transport. B, the YiiP transmembrane helical (labelled 1-6) orientation results in two solvent accessible cavities on either side of the membrane. Entrance to these cavities is gated by hydrophobic residues I90, L152 and M197. Accessibility to the cavities is altered upon zinc binding (Z1), according to the alternate access mechanism. *C*, schematic of single YiiP protomers showing the tilting of the helix 3/6 bundle (yellow) in combination with the conserved hydrophobic residue L152 from the 1/2/4/5 bundle (green) alternately provides the 'top' or 'bottom' of the solvent accessible cavity during transport, permitting solvent access to the Asp residues constituting Zn^{2+} site A. *D*, the cytoplasmic view shows the 'charge interlock' formed by the two pairs of Lys77 and Asp207 residues in the YiiP dimer which stabilise the helix 3/6 bundle orientations. Water molecules are shown as red spheres. Zn^{2+} ions are shown as magenta spheres; their ligands as sticks. In *B*, *C* and *D* the CTD is not shown for simplicity. Figures modified from (Lu et al., 2009) and (Gupta et al., 2014).

1.3 TMD structure and function

The overall architecture of *E. coli* YiiP is of a Y-shape dimer, with the two TMD protomers splayed apart and the two CTD protomers protruding into the cytosol (Fig. 1.2A; Lu and Fu 2007). The six transmembrane helices form two subdomains, in which TMs 1,2 4 and 5 form a tight bundle, and TMs 3 and 6 are somewhat separate (Lu et al., 2009). The tilting of this TM3/6 pair relative

to the tight bundle in each protomer presents a loop containing conserved hydrophobic residues at the bottom of the V-shape structure, toward the CTD (Fig. 1.2B and C; (Lu et al., 2009). The orientation of the TM3/6 pair is stabilised by hydrophobic contacts and salt bridges between Lys77 in this loop and Asp207 in the CTD (the 'charge interlock', Fig. 1.2D). The charge interlock is necessary for zinc transport function (Lu et al., 2009), although a recent study with a cryo-EM structure of *Shewanella oneidensis* YiiP (45% identity) suggests that it is not critical for the conformational changes occurring during transport (Lopez-Redondo et al., 2018). The relatively short length of TM5 (18 residues compared to average YiiP TM length of 22) results in an extracellular and an intracellular solvent-accessible cavity in each TMD protomer (Fig. 1.2B; (Gupta et al., 2014). The extracellular-facing cavity is lined with negatively charged residues which provide a favourable environment for Zn^{2+} binding (Lu et al., 2009). The intracellular-facing cavity is gated by a highly conserved hydrophobic residue in TM5, provided by L152 in YiiP (Fig. 1.2C; (Gupta et al., 2014).

The membrane topology of YiiP dictates that, in addition to the cytosolic N-terminal peptide (not resolved in the 3D structure) and CTD, the protein contains three extracellular and two intracellular loops, with an additional intracellular peptide connecting the TMD to the CTD (Lu & Fu, 2007). One of the two intracellular loops, IL2, is located at the entrance to the intracellular-facing cavity produced by the shortened TM5. This loop, commonly referred to as the His-rich loop, is typically enriched with histidine residues in the Zn-CDF clade, suggesting a role in determining metal specificity (Kambe et al., 2006). In the Fe/Zn-CDF YiiP, this loop is relatively short and does not contain histidine residues. However, even amongst Zn-CDF proteins, the His-rich loop varies greatly in length, sequence and purported function. There is no 3D structure available of this His-rich loop. CDFs which have had their structure fully elucidated, such as *E. coli* YiiP, do not contain such a loop. In other CDFs, the structure of this loop could not be resolved, for instance in *E. coli* ZnuA (Chandra et al., 2007) and *Salmonella enterica* ZinT (Ilari et al., 2014). An isolated fragment of *A. thaliana* MTP1 encapsulating IL2 contained little secondary

structure, further indicating that this loop may be disordered and difficult to structurally resolve (Tanaka et al., 2013). Mutating residues in the His-rich loop in *A. thaliana* MTP1 caused the protein to confer resistance to both cobalt and zinc, while the wild type protein could only transport zinc (Podar et al., 2012). Interestingly, the residues indentified in the His-rich loop in AtMTP1 as conferring zinc specificity, VTVTT, do not bind Zn^{2+} themselves (Podar et al., 2012), and mutation of these residues may alter the membrane topology of the transporter (Wang et al., 2018). Several other plant Zn-CDFs are highly specific for zinc, including *Populus trichocarpa* × *Populus deltoides* MTP1 (Blaudez, 2003), and *Arabidopsis halleri* MTP1 (Dräger et al., 2004), whereas others are less specific; MTP1 protein from both *Nicotiana glauca* and *Nicotiana tabacum* transport both Zn^{2+} and Co^{2+} (Shingu et al., 2005), despite containing large His-rich loops. The effects on metal specificity of the His-rich loop in plant Zn-CDFs have not been found in the mammalian proteins. The loop is typically shorter in mammalian ZnTs than in plant CDFs, and likely has a role in regulating transport activity (Blindauer, 2015).

E. coli YiiP contains four zinc binding sites per monomer; one at site A in the TMD, one at site B in the hinge region, and two at site C in the binuclear site in the CTD (Fig. 1.3). Site A is the active site for zinc transport and is highly conserved, consisting of Asp45 and Asp49 from TM2 and His153 and Asp157 from TM5 (Fig. 1.3A; (Lu et al., 2009). Non-functional mutations of these residues (e.g. Asp49Ala) ablate zinc transport function (Wei & Fu, 2006). The tetrahedral geometry formed by the site A ligands in the crystal structure of YiiP is preferred by Zn^{2+} and Cd^{2+}, but not other divalent cations, including Fe^{2+} (Wei & Fu, 2005). Mutation of Asp45 in site A to histidine limits YiiP to transporting Zn^{2+} only, and the opposite mutation in ZnT5 (His451Asp) and ZnT8 (His106Asp) permits the mammalian ZnTs to transport Cd^{2+} in addition to Zn^{2+} (Hoch et al., 2012). Therefore, as with all metal-binding proteins, the coordination geometry of the active site provides the major selectivity filter, while small changes can be enacted by substituting similar residues in the site. Crucial to the function of site A as the transport site is that the ligating residues are not constrained by secondary coordination (Fig 1.3A; (Lu et al.,

2009), meaning that they are flexible and can receive and release Zn^{2+} with a fast turnover rate (Maret & Li, 2009). Site B in YiiP (Fig. 1.3B) is not conserved even amongst bacterial CDFs, and mutation of the site did not affect transport function (Lu et al., 2009).

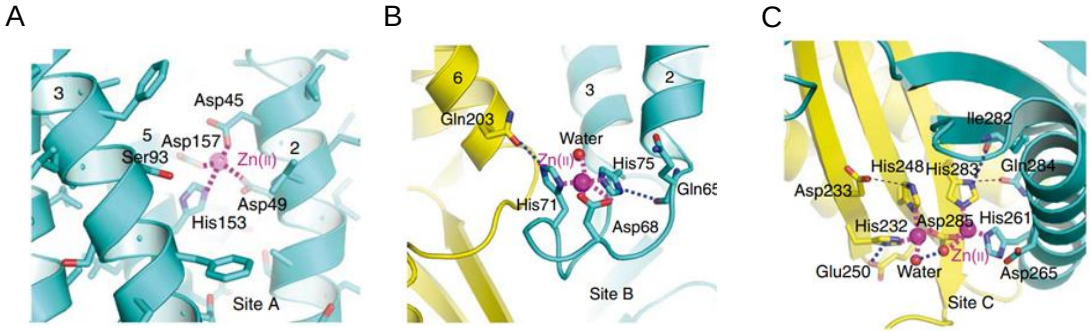

Figure 1.3. *E. coli* YiiP zinc binding sites. *A*, site A is the conserved transport site formed of residues located in helices 2 and 5. *B*, site B is in a loop between helices 2 and 3 and is not conserved in other CDFs. *C*, the binuclear site C is in the CTD. Notably, His261 is provided by the second protomer in the dimer, providing a Zn^{2+}-regulated dimerisation contact. Separate protomers in the dimer are coloured yellow and teal, Zn^{2+} ions are depicted as magenta spheres, metal ligand contacts in magenta dotted lines, and intra-residue hydrogen bonding as black dotted lines. Figures modified from (Lu et al., 2009).

1.4 CTD structure and function

The 3D structure of full-length *E. coli* YiiP is complemented by the crystal structures of the CTDs of the bacterial CDFs *T. thermophilus* apo- and zinc-bound CzrB (Cherezov et al., 2008), *Thermotoga maritima* apo-TM0876 (Higuchi et al., 2009), and *Magnetospirillum gryphiswaldense* apo-MamM (Zaytuni et al., 2014). Despite only sharing ~30% identity, the domains all form a conserved αββαβ structure, also known as a ferredoxin fold. Originally identified in iron-sulfur cluster proteins (Orme-Johnson, 1973), this fold type has been identified in many metal binding domains, including globular cytosolic proteins such as the yeast copper chaperone Atx1 (Pufahl et al., 1997), and the metal binding domains of zinc-transporting ATPases such as *E. coli* ZntA (Banci et al., 2002) and *A. thaliana* HMA4 (Zimmermann et al., 2009).

Each protomer of the YiiP CTD binds two Zn^{2+} ions in the binuclear site C (Fig. 1.3*C*). One Zn^{2+} ion is tetracoordinated by His232, His248, Asp285 and a water molecule, while the second is tetracoordinated by a water molecule, His283, Asp285 and His261 (Lu et al., 2009). His261 is provided from the second protomer (Lu et al., 2009). The carboxyl of Asp285 therefore coordinates both Zn^{2+} ions, and His261 provides a link from one CTD protomer to the other (Fig. 1.3C). His261 is located in helix α2, whereas all the other amino acid ligands are located in the β-sheets which form the CTD dimer interface (Lu & Fu, 2007). There are considerable secondary coordination contacts for the residues forming site C; His232, His248 and His261 all form hydrogen bonds with Glu250, Asp233 and Asp265 respectively, while His283 forms a hydrogen bond with Gln284 from the second protomer (Fig. 1.3C; (Lu et al., 2009). These two zinc sites are conserved in *T. thermophilus* CzrB, albeit with Glu replacing Asp285 (Cherezov et al., 2008). However, the protomer bridging Zn^{2+} is coordinated with octahedral geometry by an additional two water molecules (Cherezov et al., 2008). CzrB also binds an additional Zn^{2+} at this interface site, although the coordination is not clearly defined and is not likely to be occupied at low concentrations of Zn^{2+} (Cherezov et al., 2008). Zinc binding to *T. maritima* TM0876 has not been characterised, however the zinc binding residues from YiiP are conserved (Higuchi et al., 2009). The zinc binding sites in *M. gryphiswaldense* MamM are in different locations to YiiP, but are still localised to the CTD interface (Zaytuni et al., 2014).

In YiiP, the β-sheets of the CTD form a dimer interface which is highly charged, with a cluster of positive charges close to the membrane, and a negatively charged cluster at the base (Lu et al., 2009). This charged interface was also found in the CTD of CzrB (Fig. 1.4; (Cherezov et al., 2008). In the homodimer, these pockets of like-charges repulse each other. In full-length YiiP, the top of the CTD (close to the membrane) is stabilised by the charge interlock between Lys77 in the TMD and Asp207 in the CTD. However, in the CTD of CzrB there is no charge interlock as the CTD is isolated separately from the TMD, and the apo-protein forms a V-shape dimer (Fig. 1.4). This V-shape conformation was also elucidated for the CTDs of apo-TM0876 (Higuchi et al., 2009)

and apo-MamM (Zaytuni et al., 2014). In contrast to YiiP, the dimeric conformation of these apo-CTDs is stabilised by interprotomer hydrogen bonding formed between residues in a loop between sheet β2 and helix α2, at the bottom of the CTD (hence the V-shape).

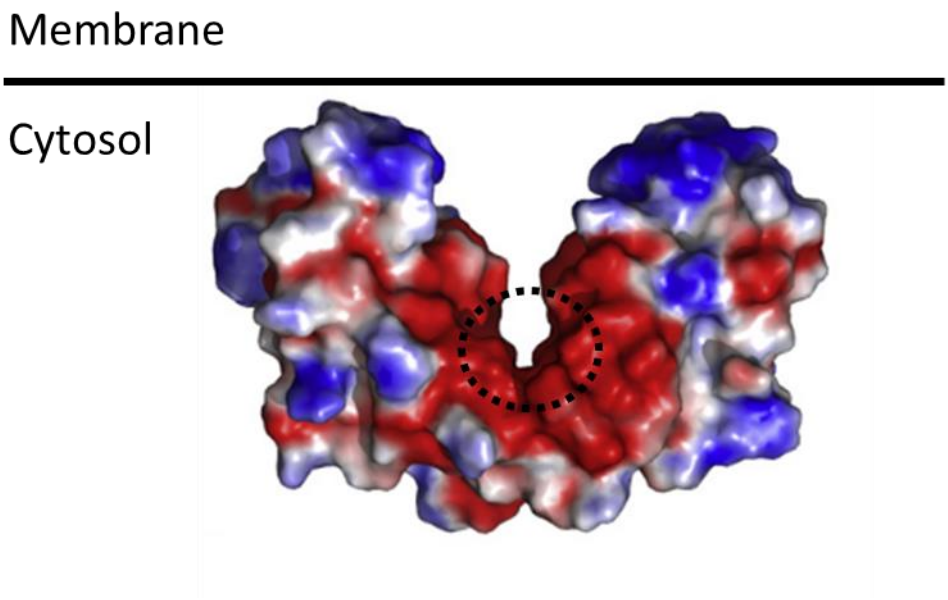

Figure 1.4. The V-shape dimer formed by the CTD of *T. thermophilus* CzrB contains charged regions. Negatively charged regions are red, positively charged regions are blue, while neutral regions are white. Zinc binding site C is located in the negatively charged cleft at the base of the V. The approximate location of Zn^{2+} binding site C is indicated by a dashed black circle. Figure modified from (Cherezov et al., 2008).

In YiiP and CzrB, the cluster of negative charges at the bottom of the CTD surrounds zinc binding site C (Fig. 1.4). Occupancy of this site with zinc negates the charge repulsion between the two CTD protomer interfaces, and thus stabilises the dimeric conformer (Lu et al., 2009). The resultant conformational change in YiiP, from an apo-X-shape to a zinc-bound Y-shape (Fig. 1.5), was elegantly highlighted by FRET-labelling the bottom of the YiiP CTD and titrating in Zn^{2+} (Lu et al., 2009). Non-functional mutation of His232, which provides the CTD interprotomer ligand to zinc binding site C, ablates this movement, and reduces transport activity (Lu et al., 2009). However, upon Zn^{2+} binding to the CTD of CzrB, the structure undergoes a 40^{O} transition from a

V-shape to a closed II-shape (Cherezov et al., 2008). This zinc-induced conformational change is also shown for MamM using small angle X-ray spectroscopy (SAXS) and by a blue-shift in the fluorescence of an interfacial Trp residue (Zaytuni et al., 2014). This difference in conformational change (CzrB and MamM CTDs changing from a V-shape to a closed II-shape, while YiiP CTD starts in a Λ-shape and changes to a closed II-shape) may be due to the lack of charge interlock in the isolated CTDs, which is necessary for YiiP transport function (Lu et al., 2009), or may represent a true difference in mechanism. It is possible that the V-shape dimer formed by the isolated CTDs may not be physiologically relevant, and the dimer interface formed between the β2-α2 loops may only be energetically favourable without the presence of the TMD. Elucidation of the 3D structures of full-length CzrB, or studies using the isolated CTD of YiiP, would aid in answering this question.

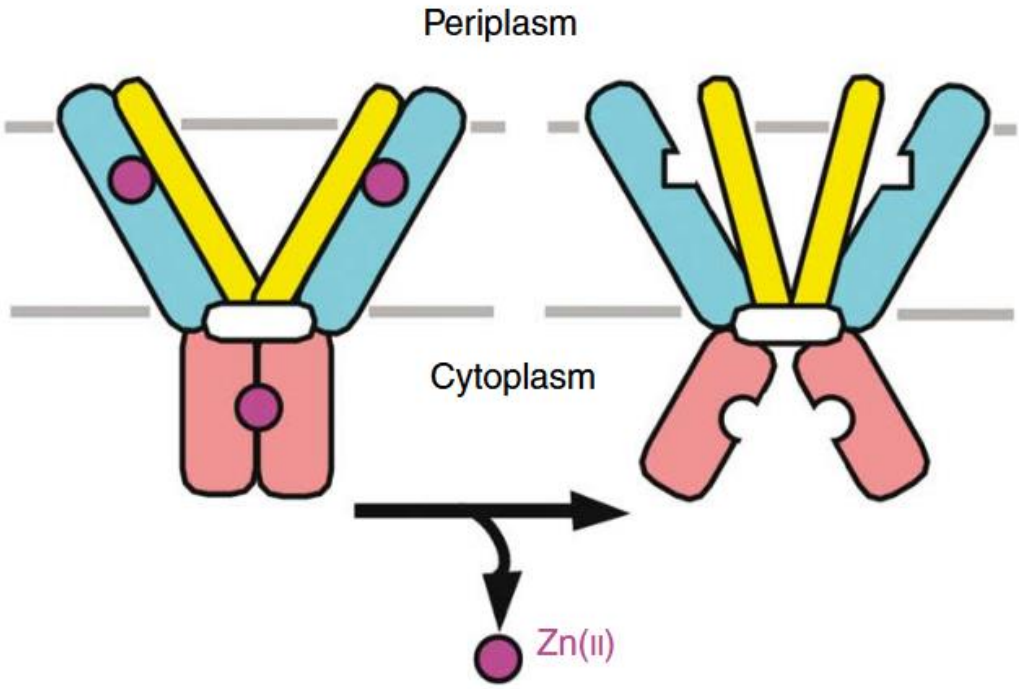

Figure 1.5. Allosteric regulation of E. coli YiiP by the CTD. Occupancy of site C in the CTD (pink) with zinc (purple circles) causes a conformational change in the TMD (blue and yellow), from an X-shape to the zinc-bound Y-shape, which allows zinc binding to the TMD transport site. Figure modified from (Lu et al., 2009).

1.5 Bacterial CDF transport mechanism

YiiP is a secondary active transporter, requiring a proton gradient to transport zinc, and functions with an alternating access mechanism (Coudray et al., 2013; Gupta et al., 2014; Lu et al., 2009). In the YiiP crystal structure, the crystals were grown in a liquor containing excess zinc, and the four zinc binding sites per monomer were occupied (Lu & Fu, 2007). This structure, with the TMDs splayed apart, is the outward-facing conformation (toward the periplasm) (Coudray et al., 2013). A cryo-EM structure of *S. oneidensis* YiiP, in which the protein was incubated with much lower concentrations of zinc, elucidated the inward-facing conformation (toward the cytosol) (Coudray et al., 2013). In this conformation, the CTD zinc sites were still occupied but the transport site (site A) was not (Coudray et al., 2013). Switching between the inward- and outward-facing conformation involves a pivot of the TMDs about the point of zinc binding at site A (Coudray et al., 2013). Specifically, the binding of Zn^{2+} to site A displaces a bound proton, and the energy released by the favourable Zn^{2+} coordination geometry causes a pivot in TM5 orientation (Gupta et al., 2014). This causes the entrance to the cytosolic facing cavity, gated by conserved hydrophobic residue Leu152, to be closed (Fig. 1.2B and C). The periplasm-cytosol pH gradient is one to two units (Ramos et al., 1976). Therefore, when the zinc-bound YiiP is in the periplasm-facing conformation, the coordinating His153 may become protonated, causing release of Zn^{2+} into the periplasm (Gupta et al., 2014). The loss of the zinc coordination then reverses the TM5 pivot, opening the L152 hydrophobic gate and exposing His153 to the cytosol with a higher pH value (Gupta et al., 2014). Subsequent deprotonation of His153 would then encourage binding of Zn^{2+} from the cytosol, completing the transport cycle. This model dictates that the presence in site A of a His residue, with a side chain pK_a of ~6, is critical to the transport mechanism.

The role of the CTD in the mechanism of CDF transport is less clear. The model for *E. coli* YiiP is that the CTD acts as a cytosolic metal sensor and allosterically regulates transport function, similar to the mechanisms elucidated for magnesium and calcium transporters (Lu et al., 2009;

Nies, 2007). Occupancy of site C by Zn^{2+} stabilises the CTD dimer interface and causes the X to Y transition (Fig. 1.5), which is transmitted to the TMD through the charge interlock hinge (Lu et al., 2009). Ablation of the inter-protomer His261 in *E. coli* YiiP indicates that the zinc-induced CTD conformational change observed is not required for transport, but the kinetics are negatively affected (Lu et al., 2009). Precisely how this movement relates to Leu152 and the opening of the cytosolic-facing cavity is not clear. Interestingly, the *Maricaulis maris* CDF MmCDF3 does not encode a CTD at all and is able to confer zinc resistance to a zinc-sensitive *E. coli* strain (Russell & Soulimane, 2012), suggesting that the CTD is not required for transport in CDFs.

The function of a zinc sensor protein is necessarily dictated by its affinity for Zn^{2+} and its relation to the concentration of free Zn^{2+} in a particular compartment (Fig. 1.1). The presence of significant secondary shell coordination in site C indicates that zinc binding to this site would be stronger than that of site A, which requires weaker binding for faster on/off kinetics (Lu et al., 2009). The K_d for the CTD conformational change in *E. coli* YiiP reconstituted in proteoliposomes, as measured using FRET-labelled protein pairs, is 24 µM (Lu et al., 2009). Earlier binding measurements using isothermal titration calorimetry (ITC) measured a K_d of 3 µM, although it is not clear to which zinc binding site in YiiP this refers (Wei & Fu, 2006). ITC measurements indicate that MamM CTD dimers have an affinity for Zn^{2+} of 16 µM (Zaytuni et al., 2014). The cryo-EM structure of *S. oneidensis* YiiP suggests that the CTD is a static element, with such a strong affinity for Zn^{2+} that the CTD is essentially constitutively occupied (Coudray et al., 2013; Lopez-Redondo et al., 2018). However, the only evidence for this statement is that in that study, CTD zinc sites remained occupied when the protein was incubated in relatively low concentrations of zinc, whereas the transport sites were not occupied, and that addition of 0.5 mM EDTA probably did not strip the CTD sites of their zinc (Coudray et al., 2013). Nevertheless, the free zinc concentration in the *E. coli* cytosol is maximally pM (Outten & O'Halloran, 2001). Therefore, under normal conditions, the CTD of YiiP cannot act independently as a zinc sensor

to drive zinc transport in the TMD. Additionally, the transport K_m value of full-length YiiP reconstituted in liposomes is hundreds of micromolar (Coudray et al., 2013; Lu et al., 2009). One argument in favour of the CTD-sensing model is that the bacterial exporters seem to function as simple regulators of zinc excess, in that there is no functional requirement for zinc to be trafficked into the periplasm by YiiP (although periplasmic zinc concentrations are still regulated (Blindauer, 2015). Therefore, as the numbers dictate, YiiP would not be functional under normal zinc homeostatic conditions, and would only become activated during episodes of severe cytosolic zinc excess. However, the function of many CDFs in higher organisms is to transport functionally significant zinc into subcellular compartments (Kambe et al., 2014). These proteins need to be able to transport zinc under normal (i.e. very low free zinc) conditions. How these proteins get their zinc is an unresolved biochemical issue. The main hypothesis to overcome this disparity in demand over supply is through delivery of zinc via a chaperone.

1.6 Metal delivery to transporters

The conserved ferredoxin fold formed by the CTDs of CDF proteins provides the basis for the theory of metal delivery. In copper transport, there are several well-characterised metallochaperone-transporter pairs in which a copper-bound cytosolic chaperone, formed of a ferredoxin fold, interacts with and delivers copper to the metal binding domain of its partner transporter, which is also formed of a ferredoxin fold (Rosenzweig & O'Halloran, 2000). The metal is then delivered to the active site of the transporter and transport of this tightly controlled metal ion can then occur. In bacteria, the CopZ chaperone delivers copper(I) to its Cu(I)-ATPase partner CopA (Multhaup et al., 2001; Rensing et al., 2000). In yeast, the Atx1 chaperone delivers copper(I) to its partner Ccc2 (Pufahl et al., 1997). In humans, the Cu(I)-ATPases ATP7A and ATP7B (Menkes' and Wilson disease proteins) are supplied by the chaperone Hah1 (Klomp et al., 1997; Rosenzweig et al., 2000). In all these chaperone/binding domain pairs, the metal binding and transfer is mediated by CXXC motifs. The residues surrounding the cysteines are critical for ion selectivity (Rosenzweig & O'Halloran, 2000). Such motifs have also

been identified in zinc transport proteins, including the metal binding domain of *E. coli* Zn-ATPase ZntA (Banci et al., 2002), and in the vesicular subfamily of mammalian ZnTs (Fig. 1.9; (Parsons et al., 2018). However, to date no partner chaperone has been identified for any zinc transporter.

The bacterial CDFs do not contain these cysteine motifs. The models of zinc delivery for *E. coli* YiiP and *T. thermophilus* CzrB suggest that upon the zinc-induced conformational change in the CTD, a docking pocket in close proximity to the cytosol-facing cavity will become available (Cherezov et al., 2008). The putative chaperone could then bind and deliver its cargo directly to the active transport site (Fig. 1.6). The His-rich loop found in many other CDF proteins is predicted to be localised in this region, and thus may provide regulation of the docking procedure. However, there is no proof of this mechanism occurring. It is worth reiterating that these models necessitate the CTD of the transporters bind Zn^{2+} to allow the chaperone to bind, which appears to occur with low affinity in the bacterial CDFs. However, this model is supported by the cryo-EM structure of *S. oneidensis* YiiP, in which the constitutively zinc-bound CTD would allow the transporter to interact with the putative chaperones (Coudray et al., 2013).

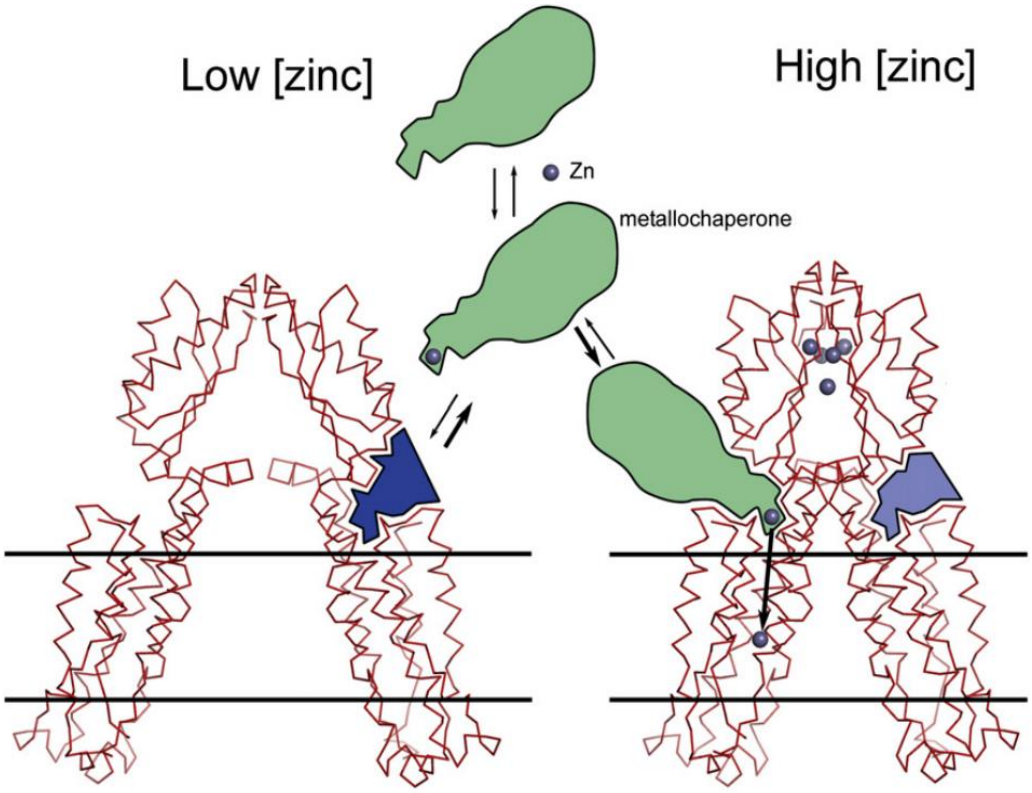

Figure 1.6. Proposed model for delivery of zinc(II) ions to bacterial CDFs. In low [zinc], the CTD of the transporter does not bind Zn^{2+}, and thus the cytosolic metallochaperone (green) cannot bind. In high [zinc], the conformational change in the CTD elicited by Zn^{2+} binding allows the chaperone to bind and deliver Zn^{2+} to the transporter. Figure modified from (Cherezov et al., 2008).

As stated above, additional mechanisms for zinc acquisition may not be required in the relatively simple export systems of bacteria. However, there are pathophysiological consequences if mammalian ZnTs cannot transport zinc (Kambe et al., 2014). Identifying the similarities and differences in zinc transport pathways between these disparate organisms is critical.

1.7 Mammalian zinc transporters

Mammalian zinc transport is largely mediated by two protein families; the ZIPs (Zrt-, Irt-related proteins, *SLC39A*) transport Zn^{2+} into the cytosol (Jeong & Eide, 2013), either from the extracellular space or from intracellular organelles, and the ZnTs (Zn Transporters, *SLC30A*) are

responsible for cytosolic Zn^{2+} efflux (Palmiter & Huang, 2004). In humans there are 14 ZIPs and 10 ZnTs (Lichten & Cousins, 2009). The relatively large number and variety of zinc transporters indicates their specialised roles, and members of both families have specific tissue, cellular and subcellular distributions (Fig. 1.7; (Kambe et al., 2015). As mentioned above, both families have homologues in all forms of life, and there are significant structural and functional differences between the two families. Having outlined the structure and function of the bacterial homologues of the ZnTs, specific details of this mammalian protein family will now be discussed.

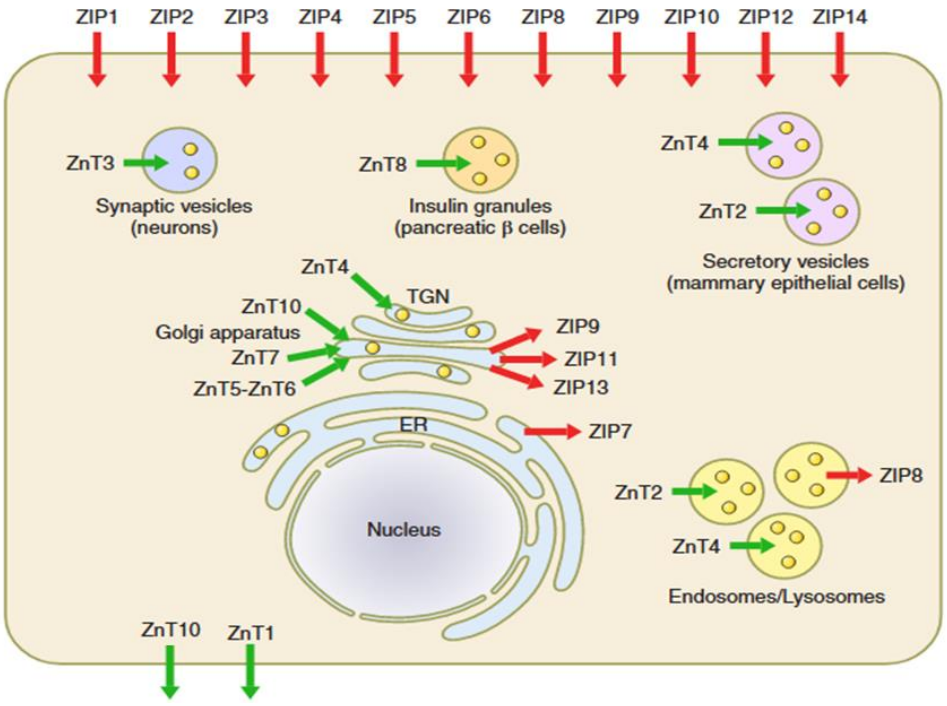

Figure 1.7. Localisation of the 14 ZIPs and 10 ZnTs found in mammalian cells. Simplified mammalian cell indicating the localisation and transport direction of mammalian zinc transporters. Figure modified from (Kambe et al., 2015).

The mammalian ZnTs can be roughly split into two subfamilies; the first, formed of ZnT2, 3, 4 and 8, are typically restricted to expression on membranes of subcellular vesicles, such as secretory granules, endosomes and lysosomes. Members of this subfamily are also typically

expressed in specific tissues and cell types. The second subfamily, containing ZnT1, 5, 6, 7 and 10, are typically expressed more ubiquitously and are localised to non-vesicular membranes (Fig. 1.7). Generally the ZnTs function as homodimers as in the bacterial homologues, however heterodimerisation of ZnT5 and ZnT6 is critical to their function (Fukunaka et al., 2009), and heterodimers between ZnT10 and several vesicular ZnTs are implicated in signal transduction (Zhao et al., 2016).

The first mammalian zinc transporter, dubbed ZnT1, was identified and described in 1995 (Palmiter & Findley, 1995). ZnT1 is ubiquitously expressed and is the only ZnT for which deletion of its gene is embryonically lethal in mice (Andrews et al., 2004). This lethality is likely due to the fact that ZnT1 is the only zinc-transporting ZnT that is predominantly localised to the plasma membrane (Fig. 1.7; ZnT10 has been found at the plasma membrane, but is a manganese transporter; (Zogzas et al., 2016). ZnT1 is implicated in signal transduction, and interactions with several intracellular proteins have been identified. Through its CTD, ZnT1 binds and activates Raf-1, a member of the Ras-ERK cascade (Jirakulaporn & Muslin, 2004). ZnT1 also modulates the activity and localisation of both L-type (Levy et al., 2009) and T-type calcium channels (Mor et al., 2012). Surprisingly, no disease-causing mutations have been described for ZnT1. Expression of ZnT1 is mediated by the Zn^{2+}-responsive transcription factor MTF-1, which also controls the levels of many other proteins involved in zinc homeostasis (Laity & Andrews, 2007; Langmade et al., 2000).

ZnT5, 6 and 7 are all localised to the Golgi and the early secretory pathway (Fig. 1.7; (Kambe, 2011). ZnT5 has several unique structural features, including an extended NTD containing an additional nine membrane spanning helices. Interestingly this NTD shares little similarity with the canonical TMD helices, and the function of this component is not clear (Fukunaka et al., 2009). A splice variant of ZnT5 (ZnT5B) is capable of bidirectional zinc transport (Valentine et al., 2007). High expression of ZnT5 in pancreatic β-cells (Kambe et al., 2002), and its role in regulating growth hormone secretion (Petkovic et al., 2014), underline the purported

importance of Golgi zinc levels in modulating vesicular zinc secretion. Similarly, Golgi zinc-loading by ZnT7 appears to provide a compensatory mechanism for zinc deficiency in the β-cell caused by knockout of ZnT8 (Syring et al., 2016). ZnT6 is missing key residues in the transport zinc site and purportedly functions as a regulator of ZnT5 in the heterodimer (Fig. 1.8; (Fukunaka et al., 2009). ZnT10 expresses an asparagine in the transport site and consequently functions as a manganese transporter (Fig. 1.8 (Nishito et al., 2016).

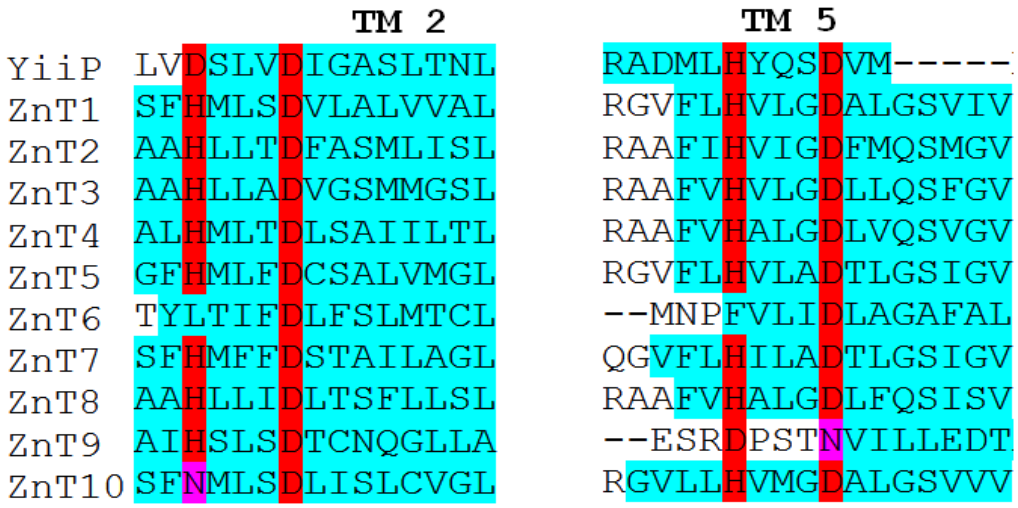

Figure 1.8. Conservation of the residues forming the zinc-binding ligands in transport site A. Blue highlighting denotes transmembrane helix, red highlighting denotes conserved zinc ligands, magenta highlighting denotes non-conserved residues with other metal binding capacity. Critical residues in the transport site of ZnT6 are not conserved, and ZnT6 consequently does not transport zinc (Fukunaka et al., 2009). The asparagine in TM2 of ZnT10 causes this protein to transport manganese (Nishito et al., 2016). The metal transport activity of ZnT9 has not been elucidated fully.

All of the ZnT family members, with the exception of ZnT5 (Kambe et al., 2002), contain similar basic architecture to the bacterial CDFs, and are predicted to form a TMD containing six transmembrane helices and a cytosolic CTD. However, most of the mammalian ZnTs contain additional structural features compared to *E. coli* YiiP. For instance, as with other members of the Zn-CDF clade, ZnTs contain His-rich loops between TM4/5. While this loop is involved in

ZnT5/6 heterodimerisation (Suzuki et al., 2005), the critical role in metal specificity elucidated for plant MTPs has not been demonstrated in mammals to date. Mutation of a Ser residue in this loop in ZnT5 has been associated with autism (O'Roak et al., 2011). A recent report indicated that the Ala-substitution of the His residues in this loop in ZnT2 did not prevent Zn^{2+} transport, but may have a regulatory effect (Fukue et al., 2018). Similarly to *E. coli* YiiP, the metal specificity of mammalian ZnTs relies on the identity of the ligands in the TMD transport site (Hoch et al., 2012).

A unique characteristic of the vesicular subfamily of mammalian ZnTs (ZnT2, 3, 4 and 8) is their ~80-100 residue N-terminal domain (NTD). These proteins are highly expressed in secretory tissues, such as the endocrine system, brain, mammary and prostate and are localised to the membranes of intracellular granules. ZnT4 has a longer NTD than the other members, and is also found in the Golgi and the *trans*-Golgi network. The function of the NTD in vesicular ZnTs is not clear. It is not required for transport in ZnT2 (Fukue et al., 2018). One might expect the NTD to act as a localisation signal to vesicles, but no clear evidence of this has been discovered so far. For instance, two isoforms of ZnT2 are expressed in human mammary cells. The long isoform is expressed on secretory vesicle membranes, while the short isoform, which contains a 49 residue deletion in the TMD but still contains the NTD, is functional as a zinc transporter at the plasma membrane (Lopez & Kelleher, 2009). However, a HHCH motif in the ZnT2 NTD, which is conserved in ZnT3 and partially conserved in ZnT8, has been implicated in targeting ZnT2 to mitochondria (Seo et al., 2011). Intriguingly, a peptide containing this motif binds Zn^{2+}, although the functional significance of this fact is not clear (Árus et al., 2013). The NTD of ZnT4 contains many residues capable of coordinating Zn^{2+}, including a CXXC motif. Predictions indicate that these NTDs are unstructured and it is tempting to speculate that Zn^{2+} binding to these sites stabilises the NTD and enables some function. ZnT8 also has two splice variants; the short isoform is missing the N-terminal 49 residues; almost the entire NTD (Carvalho et al., 2017). When overexpressed in HEK293 cells, the long isoform localises to intracellular organelles and

the plasma membrane, while the short isoform only localises intracellularly (Carvalho et al., 2017), the opposite to the expected result if the NTD targets to vesicles. The localisation of ZnT3 to a subset of synaptic vesicles is dependent on the interaction between its CTD and adaptor protein 3 (AP-3) (Salazar et al., 2004). Dephosphorylation of Ser296 in the loop connecting TM6 to the CTD of ZnT2 by tumour necrosis factor-α activates AP-3 binding and thus alters ZnT2 targeting (Hennigar & Kelleher, 2015). Mutation of the dileucine motif uncovered by the dephosphorylation prevents AP-3 binding to ZnT2 (Hennigar & Kelleher, 2015). This motif is conserved in ZnT3 but not ZnT4 or ZnT8. These somewhat disparate results indicate that the localisation signals in the vesicular ZnTs are not elucidated completely.

The overall structure of the CTDs of ZnTs is largely conserved (Fig. 1.9) except for ZnT9, which, until recently (Perez et al., 2017), was not considered to be a zinc transporter at all due to previously being identified as a transcription factor (Sim & Chow, 1999). A major difference between the mammalian ZnT CTDs and those of the bacterial CDFs is the loss of the protomer bridging His residue (His261 in *E. coli* YiiP; Fig. 1.9). His261 is critical to the CTD conformational change which forms the basis of the model for allosteric regulation of transport by CTD metal sensing in bacterial CDFs (Lu et al., 2009). Determining the role of the CTD of mammalian ZnTs in the likely absence of this mechanism is an active research area, and one of the objectives of this research project. Interestingly, despite ZnT10 being a manganese transporter, the metal binding residues in the CTD are conserved with the zinc transporting isoforms (Fig. 1.9).

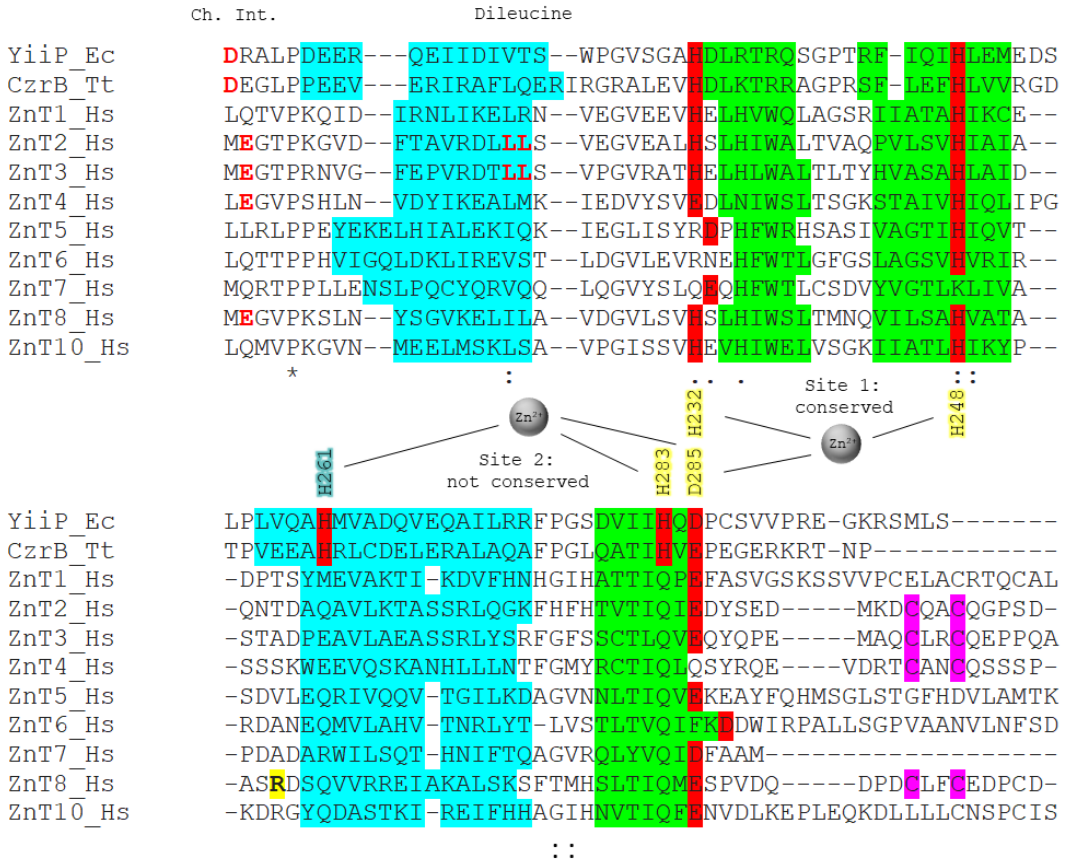

Figure 1.9. Metal binding and structural motifs in the CTDs of ZnTs and the bacterial homologues. Prediction of secondary structures in the CTDs of human ZnTs indicates that the ferredoxin fold elucidated for the bacterial homologues is conserved (α-helix in blue, β-sheet in green). Metal binding residues are highlighted in red with black text. The residues for zinc site 2 are not conserved in the mammalian ZnTs. Residue numbering is based on *E. coli* YiiP; annotated metal-binding residues highlighted in yellow are from one protomer in the dimer, H261 highlighted in blue is donated from the second protomer. Critically, H261 is not conserved in mammalian ZnTs. Residues involved in the charge interlock ("Ch. Int.") are only conserved in the vesicular ZnT subfamily (ZnT2, 3, 4 and 8). The dileucine motif is conserved in ZnT2 and 3 and is purported to regulate localisation. The CXXC motif (highlighted in purple) is also only conserved in vesicular ZnTs. The R325 residue linked to altered diabetes susceptibility in ZnT8 is highlighted in yellow.

Mutations in the CTDs of mammalian ZnTs are purported to affect transport function. The L349P mutation in the CTD of ZnT10 likely disrupts the conserved β-sheet structure and leads to hypermanganesemia (Tuschl et al., 2012). Several mutations in the conserved secondary

structures of the CTD of human ZnT2 alter zinc transport into mammary gland vesicles and cause transient neonatal zinc deficiency (TNZD) (Alam et al., 2015). Transient overexpression of ZnT2 constructs in zinc-sensitive chicken bursa lymphoma DT40 cells reveals that residues G280, T312 and E355 in the CTD of ZnT2 are critical to transport function (Golan et al., 2016). The R298C mutation in the CTD of ZnT3 increases the risk of febrile seizures (Hildebrand et al., 2015). The W325R mutation in the CTD of ZnT8 affects zinc transport (Merriman et al., 2016) and increases the risk of developing both type-2 (Rutter & Chimienti, 2015) and gestational diabetes (Ziqi Lin et al., 2018). Clearly, disrupting the structure of the ferredoxin fold and/or the zinc binding of the CTDs of mammalian ZnTs has a significant effect on the function of the full-length proteins.

1.8 ZnT8 and diabetes

Discovery of the relationship between zinc and diabetes began in 1934, when cadavers from type 1 diabetic patients were found to have 50% less pancreatic zinc than normal (Scott & Fisher, 1938). The majority of pancreatic zinc is contained within the insulin secretory granules in the β-cells, where total zinc reaches approximately 20 mM (Foster et al., 1993). To produce mature insulin, preproinsulin is formed in the rough endoplasmic reticulum and consists of two chains of insulin connected by C-peptide with an attached signalling peptide (Dodson & Steiner, 1998). The signal peptide is cleaved and proinsulin transported to the trans-Golgi network, where it is packaged into immature secretory vesicles (Dodson & Steiner, 1998). Proinsulin is then processed by zinc-dependent enzymes prohormone convertases 1/2 and 3, and carboxypeptidase E, to form mature insulin. Insulin dimers aggregate around two Zn^{2+} ions and a Ca^{2+} ion and form hexamers (Dunn, 2005). Proton-ATPases on the insulin granule reduce the pH of the granule lumen to ~6 (Hou et al., 2009). This increases the activity of the insulin maturation enzymes and stabilises the insulin hexamers (Hou et al., 2009). Insulin hexamers have greatly reduced solubility and crystallise, which is the most space-efficient storage form (Dunn, 2005). The secretion of insulin granules in response to cell membrane depolarisation exposes the insulin hexamers to neutral extracellular pH, causing dissociation into monomeric

insulin and the concomitant release of Zn^{2+} ions (Hou et al., 2009). This secreted zinc has autocrine effects on β-cells and paracrine effects on glucagon release from α-cells (Hardy et al., 2011). Insulin is also co-secreted with amylin. Aggregated fibrillar amylin is a common symptom in type 2 diabetic patients, and Zn^{2+} binding to amylin prevents aggregation (Brender et al., 2010). In mice, co-secreted Zn^{2+} also plays a role in regulating insulin clearance in the liver (Tamaki et al., 2013), although it is not clear whether this is significant in humans.

ZnT8 is a member of the vesicular subfamily of mammalian ZnTs and was identified in 2004 as being highly expressed on the membranes of insulin secretory granules in pancreatic β-cells (Chimienti et al., 2004, 2006). Its function is to supply zinc to the granules, which is critical for the formation of the crystalline storage form of insulin and other granular biochemistry (Davidson et al., 2014). It has since been shown to also be present in several other endocrine cell types (Murgia et al., 2009), including pancreatic α-cells (Solomou et al., 2015) and testicular Leydig cells (Xiuli Zhang et al., 2018). The mRNA of two splice variants of *Znt8* have been detected in human pancreatic islets, but there is only evidence of protein for the long, 369 residue variant (Eizirik et al., 2012). Expression of *Znt8* in β-cells is controlled by the β-cell specific transcription factor Pdx-1 (Pound et al., 2011). *Znt8* is downregulated in β-cells in response to reduced cytosolic zinc concentrations (Lefebvre et al., 2012), but this may be due to β-cell dedifferentiation and loss of β-cell transcription factors in response to the reduced zinc (Lawson et al., 2018), rather than a direct effect on *Znt8* itself. Interestingly, ZnT2 recruits a H^+-ATPase to vesicles in mammary epithelial cells (Lee et al., 2017), suggesting that the pH decrease in insulin granules could be dependent on ZnT8 expression, although there is no direct evidence for this.

In 2007, genome-wide association studies (GWAS) identified the rs13266634 mutation in *Znt8* causing W325R in the CTD as increasing the risk of developing type 2 diabetes by approximately 15% per allele (Saxena et al., 2007; Sladek et al., 2007). A recent meta-analysis has also linked the ZnT8 R325 variant with gestational diabetes (Ziqi Lin et al., 2018). Remarkably, the R325 risk variant is the major ZnT8 variant in human populations (Sladek et al., 2007). This revelation

sparked a great deal of interest, resulting in four global (Lemaire et al., 2009; Nicolson et al., 2009; Pound et al., 2009, 2012) and two β-cell specific (Tamaki et al., 2013; Wijesekara et al., 2010) *Znt8* knockout mouse studies. However, the knockout studies did not indicate the strong phenotype expected and contained few consensus results. All of the studies showed that *Znt8* knockout caused reduced islet zinc content and a marked change in the morphology of the insulin granules (da Silva Xavier et al., 2013). However, in general the studies showed that the islet insulin content did not change (da Silva Xavier et al., 2013). The effects of *Znt8* knockout on common diabetic markers in the mice, such as glucose-stimulated insulin secretion (GSIS), were mixed; GSIS was increased in two studies, did not change in two, and decreased in two (da Silva Xavier et al., 2013). The effects on proinsulin processing were similarly mixed (Davidson et al., 2014). The suggested reasons for the disparate results included differences in animal characteristics and husbandry between the research groups (da Silva Xavier et al., 2013). Later studies using *Znt7*/*Znt8* knockout mice revealed that knockout of *Znt8* is compensated for by the function of the Golgi-localised ZnT7, with GSIS ablated in double knockout mice (Syring et al., 2016). In their mouse knockout paper, the Rutter group showed that the ZnT8 R325 variant resulted in a less active transporter when overexpressed in MIN6 mouse insulinoma cells (Nicolson et al., 2009). At this point in time, the theory was that the increase in diabetes risk caused by the R325 variant was due to a decreased supply of zinc to the insulin granules (Nicolson et al., 2009). However, in 2014, a report detailed the genotyping of over 150,000 people indicating that rare loss-of-function mutations in *Znt8*, which lead to haploinsufficiency, are protective of type 2 diabetes (Flannick et al., 2014). Subsequent transport kinetic studies with full-length ZnT8 reconstituted into proteoliposomes indicated that the R325 variant of ZnT8 has increased transport activity in certain lipid compositions (Merriman et al., 2016). However, a second study investigating ^{65}Zn uptake into *X. laevis* oocytes by the R/W325 ZnT8 variants found no difference in transport activity (Carvalho et al., 2017). These complicated data on the relationship of ZnT8 to type 2 diabetes leave several questions unanswered. How does

haploinsufficiency of *Znt8* protect against type 2 diabetes? Does ZnT8 have additional beneficial functions which have caused it to be evolutionarily conserved among animals? Why is increased zinc transport activity by the R325 variant detrimental? Is there another mechanism which is disrupted by the mutation, for instance a protein-protein interaction? One line of experimentation that could start to answer these questions is biochemical characterisation of ZnT8.

ZnT8 is also one of the five major autoantigens found in type 1 diabetic patients (Wenzlau et al., 2007). The region of ZnT8 which is most often targeted by autoimmunity is in its CTD, and autoantibody specificity is affected by the W325R mutation (Wenzlau et al., 2008). Interestingly, human anti-ZnT8 autoantibodies do not cross-react with other mammalian ZnTs or even murine ZnT8 (Wenzlau et al., 2008), which encodes Gln at position 325. These data indicate that residue 325 is a determinant of autoantibody specificity, although encoding R or W325 does not alter the risk of developing type 1 diabetes (Wenzlau et al., 2008).

1.9 Project aims

Currently the understanding of how the mammalian ZnTs function is largely based on the models of the bacterial CDFs, such as *E. coli* YiiP. However, the bacterial model is not sufficient to describe uptake of Zn^{2+} into functionally critical secretory vesicles, as mediated by ZnT2, 3, 4 and 8. The CTD of mammalian ZnTs has a conserved overall architecture, and many mutations in this domain have pathophysiological consequences in humans. One of these is W325R in ZnT8, which increases the risk of developing type 2 diabetes. The biochemical effect of the mutation is not clear.

Therefore, this project aimed to complete the following objectives:

I. Express and purify the CTD of ZnT8.

II. Elucidate the structural and functional differences between the bacterial CDF CTDs and the CTD of ZnT8.

III. Assess the biochemical effect of the diabetes-risk W325R mutation on the CTD of ZnT8.

2. General Materials and Methods

2.1 Materials

Tris(2-carboxyethyl)phosphine hydrochloride (TCEP), HEPES, iodoacetamide, Zincon sodium salt, NaCl, K_2HPO_4, KH_2PO_4, $MgCl_2$, $ZnCl_2$, KCl, glycine, Na_2HPO_4, KH_2PO_4, $MgSO_4$, Na_2SO_4, sodium citrate, $FeCl_3$, $CuCl_2$, $CoCl_2$, H_3BO_3, α-lactose, HNO_3, KNO_3, HCl, $^{15}NH_4Cl$, methanol, DMSO and N-acetyl-DL-tryptophan were purchased from Sigma Aldrich; Coomassie Brilliant Blue R250, dithiothreitol (DTT), DNase, lysozyme, BPER lysis reagent, HisPur cobalt resin and phenylmethylsulphonyl fluoride (PMSF) from Thermo Fisher; Tris-base, glycerol and sodium dodecyl sulphate (SDS) from Severn Biotech; KI, Tween-20 and $NiSO_4.6H_20$ from Acros Organics; EDTA, NaOH, chloramphenicol from Cambridge Bioscience; LB medium powder, D-glucose and LB agar powder from MP Biomedicals; ampicillin sodium salt, L-rhamnose monohydrate from Alfa Aesar; sucrose from Merck Millipore; isopropyl β-D-1-thiogalactopyranoside (IPTG) from Promega; L,L-dityrosine dihydrochloride from Santa Cruz Biotechnology; 5,5'-dithiobis-(2-nitrobenzoic acid) (DTNB; Ellman's reagent) from Invitrogen; maleimide from Fluorochem Limited; 2-mercaptoethanol from VWR International; and imidazole from Apollo Scientific.

Table 2.1. List of plasmids used in this thesis.

Plasmid	Protein expressed	Source	Map
pM268	Cloning vector	DNA2.0 (Menlo Park, CA)	Appendix I
pET6H-TEV-ZnT8cR	His-TEV-ZnT8cR(267-369)	Protein Production Facility (KCL, London, UK)	Appendix II, III
pET6H-TEV-ZnT8cW	His-TEV-ZnT8cW(267-369)	Mutagenex (Suwanee, GA)	Appendix II, IV
pET6H-WELQ-ZnT8cR	His-WELQ-ZnT8cR(267-369)	Protein Production Facility (KCL, London, UK)	Appendix II, V
pET6H-TEV-ZnT8cRΔ359-369	His-TEV-ZnT8cR(267-358)	Protein Production Facility (KCL, London, UK)	Appendix II

pET6H-TEV-ZnT8cRΔ358-369	His-TEV-ZnT8cR(267-357)	Protein Production Facility (KCL, London, UK)	Appendix II
pET6H-TEV-ZnT8cRΔ356-369	His-TEV-ZnT8cR(267-355)	Protein Production Facility (KCL, London, UK)	Appendix II

Table 2.2. List of oligos used in this thesis.

Oligo sequence	Purpose
5'-TAATACGACTCACTATAGGG-3'	T7 sequencing
5'-CTAGTTATTGCTCAGCGGT-3'	T7_term sequencing
5'-GGATCCTTAGTCGCACGGAT-3'	ZnT8c cloning, forward
5'-TATACCATGCATCACCATC-3'	ZnT8c cloning, reverse

N.B Oligo sequence for mutation of ZnT8cR to ZnT8cW not divulged by Mutagenex, so not listed

Table 2.3. Bacterial strains used in this thesis

E. coli strain	Genotype	Source
DH5α	*F⁻ fhuA2 lac(del)U169 phoA glnV44 Φ80' lacZ(del)M15 gyrA96 recA1 relA1 endA1 thi-1 hsdR17*	Prof. Christer Hogstrand, King's College London
BL21 (DE3)	*F⁻ fhuA2 [lon] ompT gal* (λ DE3) *[dcm] ΔhsdS*	New England Biolabs (Ipswich, MA, USA)
BL21 (DE3) pLysS	*F⁻ fhuA2 [lon] ompT gal* (λ DE3) *[dcm] ΔhsdS/ pLysS(Cam^R)*	Promega (Madison, WI, USA)
ArcticExpress (DE3)	*F⁻ fhuA2 [lon] ompT gal* (λ DE3) *[dcm] ΔhsdS Tetr endA Hte [cpn10 cpn60 (Gent^R)]*	Agilent (Santa Clara, CA, USA)

OverExpress™ C41 (DE3)	*F⁻ fhuA2 [lon] ompT gal* (λ DE3) *[dcm] ΔhsdS **	Cambridge Bioscience (Cambridge, UK)
Lemo21 (DE3)	*F⁻ fhuA2 [lon] ompT gal* (λ DE3) *[dcm] ΔhsdS/ pLemo(Cam^R)*	New England Biolabs (Ipswich, MA, USA)
SoluBL21™	*F⁻ fhuA2 [lon] ompT gal* (λ DE3) *[dcm] ΔhsdS **	AMS Biotechnology (Oxford, UK)

2.2 Expression plasmids

The cDNA sequence encoding residues 267-369 of the ZnT8 R325 variant was optimised for *E. coli* expression using a proprietary tool by DNA2.0 (Menlo Park, CA). This sequence was synthesised and inserted into a pMOTHER Electra™ vector (pM268, Appendix I) by DNA2.0. The cDNA encoding ZnT8cR was then transferred into a pET6H bacterial expression vector (Appendix II, derived from pET11D) encoding an N-terminal hexahistidine tag and a WELQ protease cleavage site by the Protein Production Facility (King's College London, UK) using PCR (pET6H-WELQ-ZnT8cR, Appendix V). This pET6H-WELQ-ZnT8cR plasmid was used to produce ZnT8cR inclusion bodies (section 3.2.1). The cDNA encoding ZnT8cR was also transferred into a pET6H expression vector encoding a TEV protease site by the Protein Production Facility (King's College London, UK) using PCR (pET6H-TEV-ZnT8cR, Appendix III). Mutagenesis of the CGG codon encoding R325 (human *SLC30A8* codes CGT codon for R325, CGG is the 'optimised' codon in *E. coli*: see Appendix VI) to TGG encoding W325 was carried out by Mutagenex (Suwanee, GA) on pET6H-TEV-ZnT8cR to create pET6H-TEV-ZnT8cW (Appendix IV). Unless specified, all expression of soluble ZnT8c protein was conducted using the two variant pET6H-TEV-ZnT8c plasmids (section 2.3). Plasmid isolation was conducted using a GeneJet plasmid midiprep kit (Thermo Scientific). The sequences of all expression plasmids were confirmed with Sanger sequencing using standard T7 and T7_term primers by Eurofins Genomics (Ebersberg, Germany). Several

ZnT8cRΔCterm plasmids were constructed by the Protein Production Facility (King's College London) to test the effects of the cysteine residues on soluble protein expression. These plasmids encoded residues 267-359, 267-358 and 267-356 of ZnT8 R325 variant in the same pET6H-TEV-ZnT8cR backbone (Table 2.4).

Table 2.4. Sequences of the ΔCterm ZnT8cR constructs.

Construct	Sequence
ZnT8cR-WT	267…LTIQMESPVDQDPDCLFCEDPCD-369
ZnT8cRΔ359-369	267…LTIQMESPVDQD-358
ZnT8cRΔ358-369	267…LTIQMESPVDQ-357
ZnT8cRΔ356-369	267…LTIQMESPV-355

2.3 Soluble protein expression and purification

The two pET6H-TEV-ZnT8c plasmids were transformed using standard heat shock protocol into chemically competent *E. coli* strain SoluBL21™ (AMS Biotechnology) and streaked on LB agar plates containing 100 µg/mL ampicillin. Starter cultures of 10 mL were inoculated with either variant and grown in LB medium containing 100 µg/mL ampicillin at 25 °C overnight at 200 rpm on an orbital shaker. Overnight starter cultures were diluted to 2 L with fresh LB medium containing 100 µg/mL ampicillin and incubated at 30 °C at 200 rpm until the OD_{600} reached 0.60. Cells were then kept at 16 °C at 200 rpm on an orbital shaker for 30 min before protein expression was induced with 0.5 mM IPTG and the cells kept at 16 °C and at 200 rpm for an additional 42 h. Cells were harvested by centrifugation and resuspended in 10 mL lysis buffer (50 mM Tris/HCl, pH 8, 100 mM NaCl, 100 mM sucrose, 5 mM DTT, 2 mM $MgCl_2$, 1 mM PMSF, 5 U/ml DNase (Thermo Scientific)) until a homogenous solution was obtained. The homogenate

was diluted 1:6 with equilibration buffer (50 mM Tris/HCl, pH 8, 100 mM NaCl, 100 mM sucrose, 2 mM DTT, 20 mM imidazole, containing one tablet of Complete ULTRA mini EDTA-free protease inhibitors (Roche)), and sonicated (Model 2000U, Ultrasonic Power Corp., +285 output, 0.5 s^{-1} pulse) in an ice-water bath for 20 sec pulse and 40 sec rest settings for a total of 15 min, followed by centrifugation at 45,000 x *g* for 40 min at 4 °C. The 60 mL supernatant was added to 2 mL of pre-equilibrated Ni^{2+} affinity gel (Sigma Aldrich) and incubated end-over-end on a roller at 4 °C for 40 min. After centrifugation at 500 x *g* for 1 min at 4 °C, the pellet was washed three times with equilibration buffer containing 500 mM NaCl. The bound protein was eluted in five 1 mL washes with elution buffer (50 mM Tris/HCl, pH 8, 500 mM NaCl, 100 mM sucrose, 2 mM DTT, 300 mM imidazole). The eluate was loaded onto a Superdex S75 26/60 column (GE Healthcare) equilibrated with purification buffer (50 mM Tris/HCl, pH 8, 300 mM NaCl, 100 mM sucrose, 100 µM TCEP) using a flow rate of 2.2 mL/min and a column temperature of 4 °C. To produce ZnT8c apo-protein, 2 mM TCEP and 1 mM EDTA were added to the 10 mL fractions from size exclusion chromatography and then concentrated to approximately 0.5 mL using a 15 mL 3 kDa MWCO centrifugal concentrator (Merck Millipore). Samples were stored in this state for up to one week at 4 °C. Up to 0.5 mL protein was then diluted 30x with EDTA- and TCEP-free buffer (exact constituents are dependent on assay to be carried out as given in the corresponding methods sections) and concentrated to 0.5 mL with the same centrifugal concentrators, performing this dilution/concentration step at least three times. Reduced apo (zinc-free) protein was then used fresh within one day.

2.4 Determination of protein concentration

The concentration of the protein samples was determined spectroscopically. The extinction coefficients of 13,980 $M^{-1}cm^{-1}$ for ZnT8cW and 8480 $M^{-1}cm^{-1}$ for ZnT8cR were calculated from the primary protein sequences using the ExPASy ProtParam server (Gasteiger et al., 2005). The cysteine residues were assumed to be reduced for these calculations due to the presence of TCEP in all buffers. The accuracy of the determination was corroborated spectrophotometrically

using a modified Bradford assay (Zor & Selinger, 1996) with Bio-Rad protein assay reagent. Bovine serum albumin dissolved in purification buffer was used as the standard. Unless noted otherwise, the protein concentrations stated in this thesis were determined with spectroscopic measurement only. References to 'molar equivalents' of metal added always refer to molar equivalents of the monomeric concentration of ZnT8c.

2.5 Assessing cysteine redox state

After washing the proteins to remove reducing agent, DTNB (Ellman's reagent) was used to quantify the free sulfhydryls present in the protein samples. The reaction buffer was specific to each assay and is specified in the corresponding methods section. Protein was diluted to 2 µM in reaction buffer and the production of TNB measured after 15 min using the extinction coefficient at 412 nm of 14,150 M^{-1} cm^{-1}.

2.6 Blocking of cysteine residues

Both iodoacetamide and maleimide were used to block the three cysteine residues in the ZnT8c proteins. For iodoacetamide, a 0.5 M stock solution was prepared in water. For maleimide, a 0.5 M stock solution was prepared in DMSO. Protein samples of ≤300 µM were incubated with 15 mM of either iodoacetamide or maleimide for 1 hour at 21 ^{o}C. The concentration of DMSO in the protein samples treated with maleimide was therefore approximately 3% (v/v). Successful reaction with the cysteine sulfhydryls and therefore blocking of cysteines was confirmed by DTNB detecting 0 free sulfhydryls in the treated protein.

2.7 Circular dichroism

CD spectra were acquired using a Chirascan Plus spectrometer (Applied Photophysics, Leatherhead, UK). Near-UV CD spectra were acquired between 240-400 nm using a 10 mm path length cuvette. Far-UV CD spectra were acquired between 195-260 nm using a 0.5 mm path length cuvette. All measurements were taken using a bandwidth of 2 nm, a step size of 1 nm

and a time-per-point of 1 s. Far-UV measurements were taken at 20 °C using 0.2 mg/mL protein (approximately 15 µM) in 10 mM potassium phosphate, pH 8, 60 mM NaCl, 20 mM sucrose, whereas 0.4 mg/ml protein samples were used for near-UV CD. If a different buffer was used, this is indicated in the respective results section. CD spectra were smoothed using Chirascan Pro-Data Viewer software (Applied Photophysics) with a Savitsky-Golay smoothing factor of 4. Secondary structure content of the proteins was calculated from smoothed far-UV CD spectra using BeStSel (Micsonai et al., 2015). CD melting analyses were carried out by measuring the change in far-UV CD at 222 nm between 6-92 °C at a heating rate of 1 °C/min. A far-UV spectrum of each sample was taken before and after the melting ramp. Far-UV spectra and melting analyses were also acquired for both ZnT8 CTD variants in the presence of two molar equivalents of Zn^{2+} and Ni^{2+}, and after replacing the 60 mM NaCl in the experimental buffer with 60 mM KCl to mimic the intracellular milieu.

2.8 Protein electrophoresis

2.8.1 SDS-PAGE

Protein samples were mixed with Laemmli sample buffer (125 mM Tris/HCl, pH 6.8, 4% SDS, 20% glycerol, 10% 2-mercaptoethanol, 0.004% bromophenol blue) and loaded onto 16% (w/v) Tris-glycine polyacrylamide gels (Thermo Fisher Scientific). Dual colour protein standards were used as size markers. Proteins were separated in Tris-glycine running buffer containing 0.1% (w/v) SDS using a voltage of 120 V. Gels were either stained with Coomassie R250 dissolved in methanol/acetic acid/water or transferred to polyvinylidene difluoride (PVDF) membranes for western blot.

2.8.2 Western blot

Proteins separated using SDS-PAGE were transferred to PVDF membrane using a semi-wet transfer in transfer buffer (25 mM Tris/HCl, pH 8.3, 192 mM glycine, 20% (v/v) methanol) at 100

V for 45 minutes. Membranes were stained with Ponceau (Sigma Aldrich) to check completion of transfer, before blocking with 5% (w/v) skimmed milk in TBS-T for 1 hour at 21 ^{o}C. Presence of His-ZnT8c protein was probed with 1:1000 mouse anti-His-tag primary antibody, followed by probing with 1:15,000 rabbit anti-mouse HRP-conjugated secondary antibody. ECL reagent was added and chemiluminescence was detected on X-ray film using an X-ray film processor (Konica Minolta, Tokyo, Japan).

2.8.3 Native PAGE

ZnT8c protein samples of either variant were diluted to 20 µM (measured both spectroscopically and spectrophotometrically with a modified Bradford assay) in 50 mM Tris/HCl, pH 8, 300 mM NaCl, 100 mM sucrose. Some samples were incubated for 1 h at 20oC with 20 mM beta-mercaptoethanol, 20 mM DTT, 2 mM $ZnCl_2$, 10 mM $ZnCl_2$, or 20 mM EDTA; these samples are indicated in their respective results sections. Samples were then mixed with native sample buffer and separated on ice at 60 V using Novex 16% Tris-glycine precast gels (Thermo Scientific) with native running buffer (25 mM Tris/HCl, pH 8.3, 190 mM glycine). NativeMARK unstained protein standards were used as size markers. Gels were stained using Coomassie R250.

2.9 Bioinformatics and molecular modelling

Primary protein sequences were compared using Clustal Omega (EMBL) and secondary structure predictions were carried out using Jpred 4 (Drozdetskiy et al., 2015). Homodimers of both ZnT8c variants (residues 267-369) were modelled with SWISS-MODEL (Biasini et al., 2014) based on the 3D structure of the CTD of *T. thermophilus* homologue CzrB (residues 199-284, pdb IDs 3byr and 3byp) with two zinc ions bound. The CzrB templates both provided a primary sequence coverage of 79% of ZnT8c, with an identity of 19.8% (alignment given in Appendix VII). CzrB was chosen as the primary basis for the models rather than *E. coli* YiiP owing to the availability of the zinc-bound conformation of CzrB in the SWISS-MODEL template selection algorithm. Models

constructed based on YiiP and other available bacterial CDF CTDs returned similar models. PyMOL was used for visual representation of 3D structure.

2.10 Statistics

All statistical significance was assessed by unpaired Student's *t*-tests using SigmaPlot 14.0 (Systat Software Inc).

3. Expression and purification of the two ZnT8 CTD variants

Abstract

The CTDs of the Zn-CDF family of transporters purportedly mediate protein-protein interactions, sense cytosolic zinc, and/or channel zinc to the transport site in the TMD. Mutations in the CTDs of several mammalian ZnTs cause disease. The W325R mutation in the CTD of ZnT8 increases diabetes risk and affects the transport function of the full-length protein. Biochemical characterisation of these two variant domains of ZnT8 will shed light on the effects of this mutation and on other members of the mammalian ZnTs. Both variants express in a predominantly insoluble form. Optimisation of the bacterial expression yields soluble protein, but a large proportion of this protein forms amyloid-like β-sheet structure. However, some soluble protein forms a stable dimeric conformation, as seen in the isolation of homologous domains in bacteria. The yield of the dimeric protein is sufficient to perform experiments to characterise the ZnT8c proteins.

3.1 Introduction

There is no published 3D structure of a eukaryotic CDF. The current models for the structure and function of these proteins are based on those elucidated for prokaryotes, especially the *E. coli* Fe/Zn-CDF YiiP (Lu et al., 2009; Lu & Fu, 2007). YiiP is formed of a TMD which shares relatively high identity with the mammalian ZnTs (approximately 30% identity), and a CTD for which the primary sequence is poorly conserved in mammals (approximately 15% identity). However, the overall fold of the CTD is predicted to be conserved (Fig. 1.9). The CTD of CDF proteins is purported to function as a metal sensor, allosterically regulating the function of the transporter (Lu et al., 2009).

Sequence analysis reveals that the CTD zinc binding sites are not fully conserved in mammalian ZnTs, and that metal-binding cysteine motifs are present in vesicular ZnTs (Fig. 1.9; (Parsons et al., 2018). This raises the question of whether the mechanistic models based on bacterial CDFs can be applied to the mammalian proteins. The CTDs of mammalian ZnTs also mediate protein-protein interactions. For instance, the CTD of ZnT1 interacts with Raf-1 to activate Ras-ERK signal transduction (Jirakulaporn & Muslin, 2004), and modulates the activity and localisation of T-type calcium channels (Mor et al., 2012). Mutations in the CTDs of ZnTs are commonly linked to disease susceptibility in humans, including L349P in ZnT10 leading to hypermanganesemia (Tuschl et al., 2012), R298C in ZnT3 increasing risk of febrile seizures (Hildebrand et al., 2015), and several mutations in ZnT2 CTD leading to TNZD (Alam et al., 2015). Therefore, characterisation of these mammalian domains is of critical importance.

The studies on full-length bacterial CDF proteins are complemented by several reports on isolated bacterial CDF CTDs (Hattori et al., 2007; Höfer et al., 2007; Zeytuni et al., 2012), which confirm that this domain forms a stable ferredoxin-like fold independent of the TMD. This ferredoxin-like fold is also found in a number of mammalian metalloproteins (Blindauer, 2015). One example is the human copper chaperone Atox1, which has been successfully expressed in

E. coli (Belviso et al., 2016). Therefore, it is reasonable to assume that expression of the CTD of ZnT8 would be possible in *E. coli*.

E. coli expression strains have typically been chosen for protein expression following genetic modification to remove coding regions for certain proteases and to drive the metabolism of certain sugars. Most *E. coli* expression strains are 'B' strains, typically derived from BL21, therefore some characteristics are shared, such as deficiency in the Lon and OmpT proteases. Some mutations are designed to control how the bacteria treat the transformed DNA plasmid, for instance the *hsdS$_B$ (r_B^- m_B^-)* and *dcm* genotypes inactivate bacterial DNA methylation systems. The (DE3) phage lysogen means that the strains express the T7 RNA polymerase under the control of the lacUV5 promoter, which is induced by IPTG. The T7 RNA polymerase recognises the T7 promoter in the pET6H plasmid containing the gene of interest. This allows tight control over the point at which the bacteria express the protein of interest.

The aims of this chapter are to describe the experiments that have been performed to optimise the recombinant expression and purification of the two common human ZnT8 CTD variants in *E. coli*.

3.2 Methods

3.2.1 Inclusion body production and refolding

The pET6H-WELQ-ZnT8cR plasmid (section 2.2) was transformed using standard heat shock protocol into chemically competent *E. coli* strain BL21(DE3)pLysS and streaked on LB agar plates containing 100 µg/mL ampicillin. Starter cultures of 10 mL were grown in LB medium containing 100 µg/mL ampicillin at 37 °C overnight at 200 rpm on an orbital shaker. Overnight starter cultures were diluted to 1 L with fresh LB medium containing 100 µg/mL ampicillin and incubated at 37 °C at 200 rpm until the OD_{600} reached 0.55. Cells were then kept at 18 °C at 200 rpm on an orbital shaker for 30 min before protein expression was induced with 0.5 mM IPTG

and the cells kept at 18 °C and at 200 rpm for an additional 18 h (overnight). Cells were harvested by centrifugation at 6000 x *g* for 20 minutes, resuspended in 80 mL PBS, centrifuged again with the same conditions and frozen at -20°C until lysed. For lysis, cell pellet was resuspended in 8 mL BPER lysis reagent (Thermo Scientific) containing 1 mg/ml lysozyme (Thermo Scientific), 1 mM PMSF and 10 U/mL DNase (Thermo Scientific). Homogenate was incubated at room temperature for 30 min, then sonicated (Model 2000U, Ultrasonic Power Corp., +285 output, 0.5 s^{-1} pulse) in an ice-water bath for 20 sec pulse and 40 sec rest for a total of 15 min, followed by centrifugation at 20,000 x *g* for 30 min at 4 °C. The pellet was washed twice with 10 mL of 20 mM Tris/HCl, pH 8, 0.5 M NaCl, 1 mM DTT and 1% Triton X-100, and centrifuged again under the same conditions. Finally, the pellet was resuspended in 10 mL of 20 mM Tris/HCl, pH 8, 0.5 M NaCl, 1 mM DTT, and 2 mL aliquots taken.

The purified His-WELQ-ZnT8cR inclusion bodies were resuspended in 20 mL solubilisation buffer (20 mM Tris/HCl, pH 8, 0.5 M NaCl, 6 M guanidium hydrochloride, 1 mM DTT) and incubated for 1 h at room temperature. The homogenate was centrifugated at 20,000 x *g* for 10 min at 4°C. The supernatant was loaded on to 1 ml of HisPur cobalt resin (Thermo Scientific) pre-equilibrated with solubilisation buffer. Loaded resin was washed with 20 mL of solubilisation buffer containing 5 mM imidazole. The buffer was exchanged to 20 mM Tris/HCl, pH 8, 0.5 M NaCl, 6 M urea, 1 mM DTT, 5 mM imidazole. Protein was refolded at 4°C using a linear 6-0 M urea gradient in 0.5 M steps in a total volume of 48 mL. Following refolding, the resin was washed with 20 mM Tris/HCl, pH 8, 0.5 M NaCl, 1 mM DTT, 5 mM imidazole. The refolded recombinant protein was eluted in five 1 mL washes with 20 mM Tris/HCl, pH 8, 0.5 M NaCl, 0.5 M imidazole, 1 mM DTT.

3.2.2 Small-scale expression tests

Small-scale expression tests were carried out to optimise the soluble protein expression conditions. These tests were conducted with the pET6H-TEV-ZnT8c plasmids. The conditions

tested included various strains of *E. coli*, medium compositions, induction times and temperatures. The *E. coli* strains tested were BL21(DE3), BL21(DE3)pLysS, SoluBL21™, ArcticExpress(DE3), OverExpress™ C41, and Lemo21(DE3) (Table 2.3). Competent bacteria (all strains were competent when acquired) were transformed with the pET6H-TEV plasmid encoding ZnT8cR or ZnT8cW and incubated overnight on agar plates containing 100 µg/mL ampicillin. Agar plates streaked with BL21(DE3)pLysS or Lemo21 contained 35 µg/mL chloramphenicol in addition to 100 µg/mL ampicillin. Single colonies were picked and incubated in 10 mL LB medium containing the appropriate antibiotic(s) overnight at 25 °C on an orbital shaker at 200 rpm. Typically, 0.5 mL of these starter cultures was used to inoculate 50 mL of fresh LB medium in 250 mL Erlenmeyer flasks. In some expression tests this fresh LB medium was supplemented with 0-10 mM $ZnCl_2$. The cultures were incubated at 30 °C until the OD_{600} reached ~0.6, then transferred to an orbital shaker at the desired temperature. Cultures were then induced with 0.5 mM IPTG and incubated for 18-42 hours. Lemo21 cultures were supplemented with either 0.5 or 1 mM rhamnose at the point of induction. Bacterial pellets were collected by centrifugation at 3220 x *g* for 25 min at 4 °C. Pellets were lysed with 1 mL BPER lysis reagent (Thermo Scientific) containing 1 mg/ml lysozyme, 10 U/mL DNase I and 1 mM PMSF (all Thermo Scientific). The homogenate was incubated at room temperature for 15 min and then spun at 14,000 x *g* for 10 min at 4 °C.

3.2.3 Double colony selection

The SoluBL21™ *E. coli* strain was selected for large-scale expression of the proteins. 'Double colony selection' (Sivashanmugam et al., 2009) was used to eliminate heterogeneity in protein expression levels and to increase the yield of soluble protein. Four separate single colonies of SoluBL21™ cells transformed with either pET6H-TEV-ZnT8cR or pET6H-TEV-ZnT8cW were picked and grown overnight in LB-ampicillin at 25 °C at 200 rpm on an orbital shaker. Aliquots of these overnight starter cultures were used to prepare glycerol stocks and were stored at -70 °C. The cultures were used to inoculate fresh LB medium and incubated at 30 °C at 200 rpm until OD_{600}

reached 0.6 and subsequently induced overnight with 0.5 mM IPTG at 16 °C at 200 rpm on an orbital shaker. The bacterial pellet was collected by centrifugation at 3220 x *g* for 25 min at 4 °C. The pellet was resuspended in Laemmli buffer containing 10% 2-mercaptoethanol and the total protein expression levels of the four colonies were analysed with SDS-PAGE. The glycerol stock of the colony which was judged to produce the highest level of total protein expression was used to streak a second agar-ampicillin plate, and the process repeated. The glycerol stocks containing the highest expressing colony for both ZnT8cR and ZnT8cW in this second round of expression tests was used as the stock for all the high-yield soluble protein preparations described in General Methods (section 2.3).

3.2.4 Protease cleavage

The pET6H-TEV-ZnT8c expression plasmids encode a TEV protease cleavage site between the hexahistidine tag and the ZnT8 CTD. Purified ZnT8 CTD proteins were incubated with ProTEV Plus (Promega) and AcTEV (Life Technologies) proteases. Triton X-100 detergent was added to a final concentration of 0.1% (v/v). Several different cleavage temperatures and times were tested. Following cleavage, samples were centrifuged at 14,000 x *g* for 5 min. Nickel affinity gel (Sigma-Aldrich) was added to the supernatant and incubated for 20 min at 4 °C to bind to His-tagged entities. The nickel gel was isolated by centrifugation and imidazole was used to elute the protein from the beads. The cleavage products were then analysed by SDS-PAGE (section 2.8.1).

3.3 Results

3.3.1 Expression plasmids

The open reading frames of interest of both the pET6H-TEV-ZnT8cR and pET6H-TEV-ZnT8cW plasmids were sequenced and the encoded protein sequences elucidated (Table 2.1, Fig. 3.1). Both plasmids encode 119 residue proteins containing an N-terminal hexahistidine tag followed by a TEV protease cleavage site (highlighted blue and green in Fig. 3.1, respectively) and residues

267-369 of human ZnT8. The CGT codon encoding R325 (highlighted in yellow in Fig. 3.1) was mutated in pET6H-TEV-ZnT8cW to TGG to encode W325 (Table 2.1).

```
  1  M  H  H  H  H  H  H  S  T  E  N  L  Y  F  Q  G  L  K  D  F
  1 ATGCATCACCATCACCATCACTCGACCGAAAACCTGTATTTTCAGGGCCTGAAAGACTTT
 21  S  I  L  L  M  E  G  V  P  K  S  L  N  Y  S  G  V  K  E  L
 61 AGCATTCTGTTGATGGAAGGTGTGCCGAAAAGCCTGAACTACTCTGGTGTGAAAGAACTG
 41  I  L  A  V  D  G  V  L  S  V  H  S  L  H  I  W  S  L  T  M
121 ATTCTGGCCGTTGATGGCGTTCTGAGCGTCCACTCCCTGCATATCTGGAGCCTGACGATG
 61  N  Q  V  I  L  S  A  H  V  A  T  A  A  S  R  D  S  Q  V  V
181 AATCAAGTCATCCTGAGCGCACATGTTGCGACCGCAGCGAGCCGTGACAGCCAAGTGGTC
 81  R  R  E  I  A  K  A  L  S  K  S  F  T  M  H  S  L  T  I  Q
241 CGCCGTGAGATCGCGAAGGCTCTGAGCAAGTCCTTCACCATGCACAGCCTGACCATTCAG
101  M  E  S  P  V  D  Q  D  P  D  C  L  F  C  E  D  P  C  D  *
301 ATGGAGTCGCCGGTTGATCAGGACCCGGATTGTCTGTTCTGCGAGGATCCGTGCGACTAA
```

Figure 3.1. DNA and translated protein sequence of pET6H-TEV plasmid encoding 6xHis-TEV-ZnT8cR. The hexahistidine tag is highlighted in cyan and the TEV protease site is highlighted in green. TEV protease cleaves after the Q residue, leaving a G overhang. The plasmid DNA sequence was optimised for expression in *E. coli* and encodes residues 267-369 of ZnT8. The ZnT8 R325 residue and its corresponding codon are highlighted in yellow. The pET6H-TEV plasmid encoding ZnT8cW was produced by replacing the highlighted "CGT" R325 codon with "TGG" (encoding W).

The expected mass of the uncleaved proteins was 13,337 g/mol for ZnT8cR and 13,367 g/mol for ZnT8cW (Table 3.1). The plasmids were transformed into various *E. coli* expression strains for protein expression.

Table 3.1. Properties of cleaved and uncleaved His-TEV-ZnT8c proteins, predicted using the ExPASy server (Gasteiger et al., 2005).

Variant	Mass (uncleaved, g/mol)	Mass (cleaved, g/mol)	pI (uncleaved)	pI (cleaved)	Predicted extinction coefficient (uncleaved, $M^{-1}.cm^{-1}$)
ZnT8cR	13,337	11,400	5.86	5.13	8480
ZnT8cW	13,367	11,430	5.70	4.91	13,980

3.3.2 Inclusion body production and refolding

Initial efforts to express ZnT8cR protein were conducted using the pET6H-WELQ-ZnT8cR plasmid in BL21(DE3)pLysS *E. coli* (section 3.2.1) using 0.5 mM IPTG induction for 18 h at 18°C. With these conditions, His-WELQ-ZnT8cR expressed in a predominantly insoluble form (n > 3, Fig. 3.2A). His-WELQ-ZnT8cR inclusion bodies were prepared and solubilised using 6 M guanidium hydrochloride and bound to HisPur cobalt resin. Following refolding with a 6 – 0 M urea gradient, a small amount of 'refolded' His-WELQ-ZnT8cR protein was eluted from the resin in buffer containing 0.5 M imidazole (n = 3, Fig. 3.2B). The majority of the ZnT8cR protein only eluted from the resin following incubation in denaturing Laemmli buffer (n = 3, Fig. 3.2B). Far-UV CD spectra of the 'refolded' His-WELQ-ZnT8cR protein were typical of β-sheet secondary structure (n = 3, Fig. 3.2C). The BeStSeL algorithm confirmed that this protein was rich in β-sheet structure and did not contain similar secondary structure content to the CTD of the *E. coli* homologue YiiP (n = 3, Fig. 3.2D).

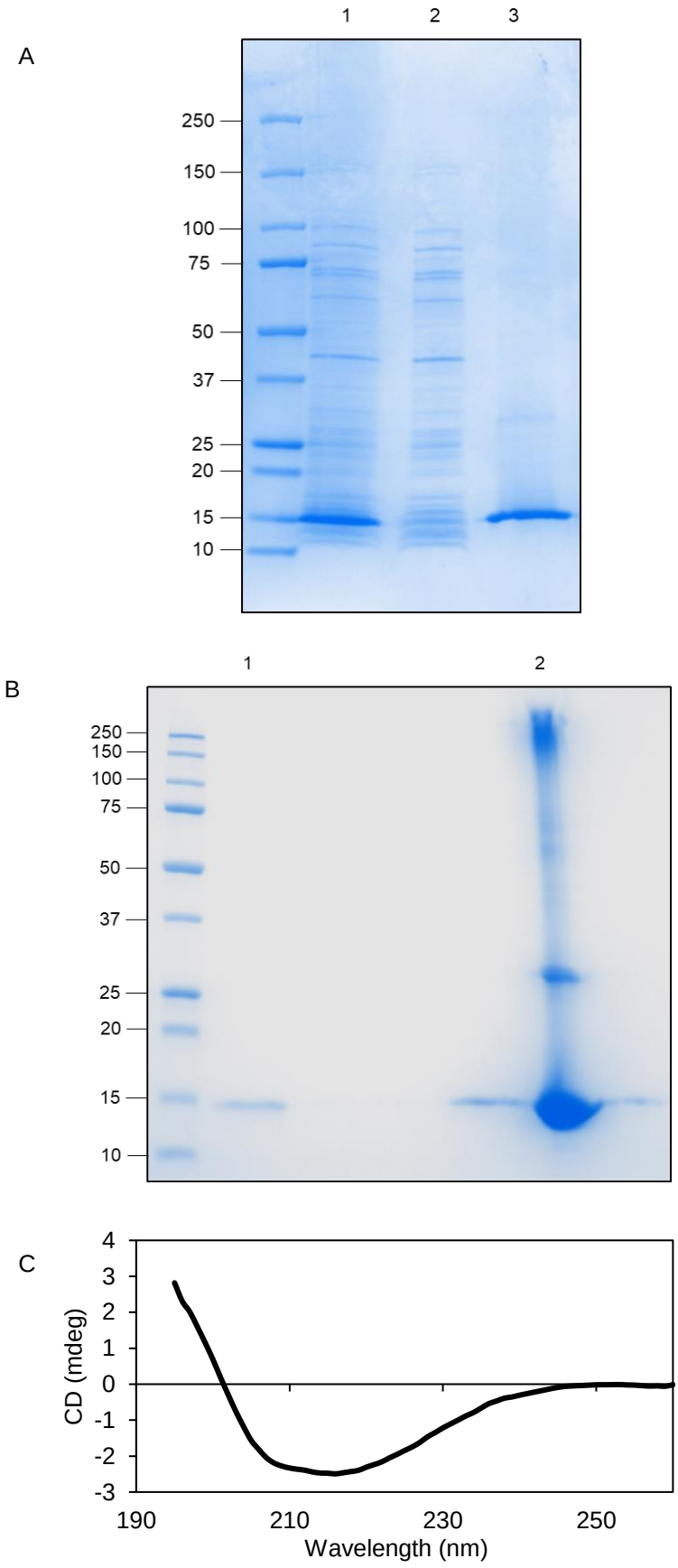
A
1
2
3
250
150
100
75
50
37
25
20
15
10
B
1
2
250
150
100
75
50
37
25
20
15
10
C
CD (mdeg)
4
3
2
1
0
-1
-2
-3
190
210
230
250
Wavelength (nm)

D

Structure	'Refolded' His-WELQ-ZnT8cR	YiiP
α-helix (%)	6.7 ±1.5	24
β-sheet (%)	34.9 ±4.6	23
Turn (%)	13.5 ±2.1	n/a
Other (%)	44.8 ±4.3	n/a

Figure 3.2. Refolding of His-WELQ-ZnT8cR expressed in inclusion bodies. A, representative (n = 3) SDS-PAGE analysis of His-WELQ-ZnT8cR protein expression in BL21(DE3)pLysS *E. coli* induced with 0.5 mM IPTG at 18°C for 18 h. Cells were lysed with BPER lysis reagent (Thermo) containing 1mg/ml lysozyme, 10 U/mL DNase and 1 mM PMSF. Lane 1 contains the total protein fraction; lane 2 contains the soluble protein; lane 3 contains insoluble protein. Protein marker sizes are indicated on the left in kDa. B, SDS-PAGE analysis of His-WELQ-ZnT8cR protein refolded on HisPur cobalt beads (Thermo) using a linear 6-0 M urea gradient. Lane 1, protein eluted from the beads with buffer containing 500 mM imidazole. Lane 2, protein retained on the beads following elution. Protein marker sizes are indicated on the left in kDa. *C*, representative (n = 3) far-UV CD spectra of 0.2 mg/ml His-WELQ-ZnT8cR in 20 mM Tris/HCl, 150 mM NaCl, 50 mM sucrose, pH 8. *D*, individual far-UV CD spectra of 'refolded' His-WELQ-ZnT8cR were analysed using the fold-recognition algorithm BeStSel. YiiP secondary structure content was calculated from the 3D structure (PDB ID 2qfi).

3.3.3 Protein expression tests

Refolding insoluble protein from His-WELQ-ZnT8cR inclusion bodies did not produce correctly folded protein. To improve the yield of soluble protein expression the expression plasmid was changed from pET6H-WELQ to pET6H-TEV and several different conditions were tested, including various *E. coli* expression strains, medium compositions, induction times and induction temperatures.

3.3.3.1 Different bacterial strains

Western blot analysis showed that, when other conditions are kept constant, the yield of soluble and insoluble ZnT8c protein varies depending on the *E. coli* expression strain used. For instance, in BL21(DE3) *E. coli*, both ZnT8cR and ZnT8cW proteins were successfully expressed, albeit in a

predominantly insoluble form, whereas in Arctic Express *E. coli* there was minimal total ZnT8cR expression (Fig. 3.3A). Furthermore, expression of ZnT8cR in Lemo21 *E. coli* incubated with either 0.5 or 1 mM rhamnose was minimal, whereas expression of ZnT8cW in the same strain showed expression of both soluble and insoluble protein (Fig. 3.3B and C, lanes 7-10). Lanes containing insoluble protein of both ZnT8c variants expressed in BL21(DE3) contain multiple bands; a strong band at 14 kDa, a second distinct band at 13 kDa and a third band at 26 kDa (Fig. 3.3A). This pattern of bands at 13 and 14 kDa is also present in lanes containing insoluble protein of both ZnT8c variants expressed in C41, BL21(DE3)pLysS, and SoluBL21™ strains (Fig. 3.2B and C). The third band at approximately 26 kDa was also seen in lanes containing insoluble ZnT8c protein of both variants expressed in BL21(DE3)pLysS, and in the lane containing ZnT8cR insoluble protein expressed in C41 (Fig. 3.3B and C). In contrast, all lanes containing detectable levels of soluble ZnT8c protein of either variant contained a single band at approximately 14 kDa (Fig. 3.3B and C). The lanes containing soluble protein of both ZnT8c variants expressed in the SoluBL21™ strain had the strongest western blot signal (Fig. 3.3B and C). Therefore SoluBL21™ produced the most soluble ZnT8c protein for both variants under these conditions, and was used for high-yield protein expression of both variants throughout the research project. It is important to note that despite SoluBL21™ *E. coli* producing the highest yield of soluble ZnT8c protein, the majority of the ZnT8c protein was still expressed in an insoluble form (Fig. 3.3B and C, lane 6). Semi-quantitative analysis of the soluble protein expression levels for both ZnT8c variants in each tested *E. coli* strain used are provided in Table 3.2.

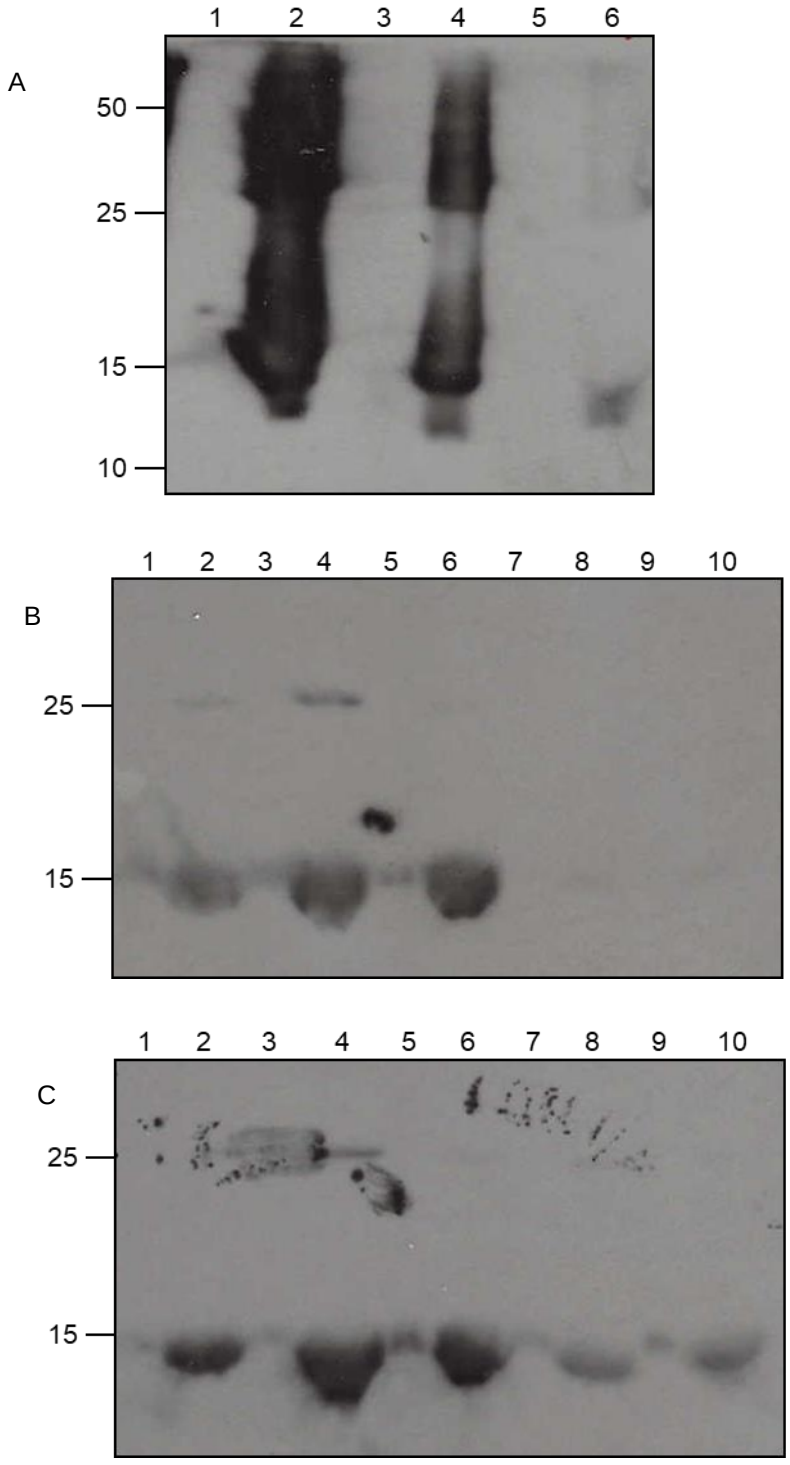

Figure 3.3. ZnT8c expression tests in different bacterial strains. Bacterial cultures were grown to OD_{600} of 0.6 and then induced overnight with 0.5 mM IPTG at 16 ^{o}C and 200 rpm on an orbital shaker. Soluble and insoluble protein fractions were separated using SDS-PAGE, transferred to PVDF membrane and probed with an anti-His tag primary antibody (see General Methods). The position of Precision Plus protein standards (BioRad) are indicated on the left in kDa. *A*, lane 1 contains soluble ZnT8cR protein expressed in BL21(DE3) *E. coli*; lane 2 contains the insoluble protein fraction. Lane 3 contains soluble ZnT8cW protein expressed using the same conditions in BL21 (DE3)*E. coli*;

lane 4 contains the insoluble fraction. Lane 5 contains soluble ZnT8cR protein expressed in the ArcticExpress bacterial strain; lane 6 contains the insoluble protein fraction. Blots of, *B*, ZnT8cR and, C, ZnT8cW; lane 1 contains soluble protein expressed in OverExpress™ C41 *E. coli*; lane 2 contains the insoluble protein fraction. Lane 3 contains soluble protein expressed in BL21(DE3)pLysS *E. coli*; lane 4 contains the insoluble protein fraction. Lane 5 contains soluble protein expressed in SoluBL21™ *E. coli*; lane 6 contains the insoluble protein fraction. Lane 7 contains soluble protein expressed in Lemo21 *E. coli* using 0.5 mM rhamnose during induction; lane 8 contains the insoluble protein fraction. Lane 9 contains soluble protein expressed in Lemo21 *E. coli* using 1 mM rhamnose during induction; lane 10 contains the insoluble protein fraction. These expression tests were not repeated (n = 1).

Table 3.2. Semi quantitative analysis of ZnT8c soluble protein expression in the *E. coli* expression strains tested.

E. coli strain	Soluble ZnT8cR expression	Soluble ZnT8cW expression
BL21 (DE3)	+	n/a
BL21 (DE3) pLysS	++	+
ArcticExpress (DE3)	-	n/a
OverExpress™ C41 (DE3)	++	+
Lemo21 (DE3)	-	++
SoluBL21™	+++	++++

3.3.3.2 Induction temperature and time

Both ZnT8c protein variants had increased expression of soluble protein when incubated overnight (18 h) at 16 °C compared to both 25 and 30 °C (Fig. 3.4, the difference was detected visually from the gels, the photograph in the figure do not show the difference clearly). A serendipitous discovery was that increasing the induction time for both ZnT8c variants to 42 h at 16 °C had a marked impact on the yield of total ZnT8c protein (Appendix VIII).

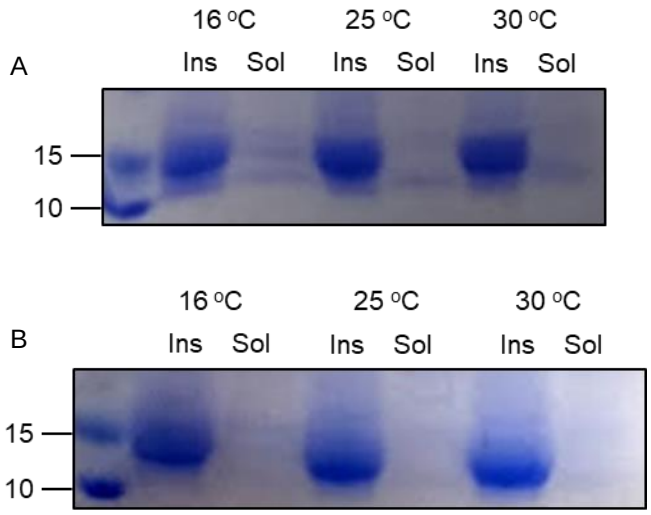

Figure 3.4. ZnT8c expression tests varying induction temperature. SoluBL21™ *E. coli* transformed with, *A*, pET6H-TEV-ZnT8cR and, *B*, pET6H-TEV-ZnT8cW were induced with 0.5 mM IPTG overnight at 200 rpm at 16, 25 or 30 °C. Bacterial pellets were lysed with BPER reagent (Thermo Scientific) and centrifuged to separate soluble ('Sol') from insoluble ('Ins') material. Protein was separated on 16% SDS-PAGE gels and stained with Coomassie R250. The position of Precision Plus protein standards (BioRad) are indicated on the left in kDa. The presented gels are representative of 2 repeats (n = 2).

3.3.3.3 Zn in culture medium

Due to the predicted presence of zinc binding sites in both ZnT8c variant proteins, $ZnCl_2$ was supplemented into the LB culture medium upon induction of protein expression. This expression

test was carried out using BL21(DE3)pLysS *E. coli* (as the beneficial effects of SoluBL21 had not been determined at this time). Addition of up to 10 mM $ZnCl_2$ reduced the level of soluble ZnT8cR protein expression (Fig. 3.5A), but had no clear effect on the level of soluble ZnT8cW protein expression (Fig. 3.5B).

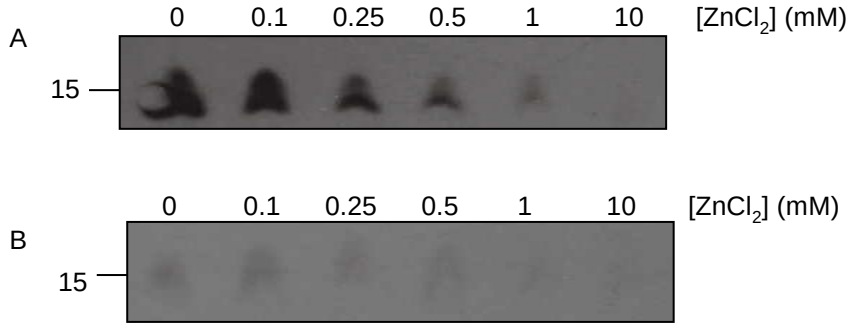

Figure 3.5. ZnT8c expression tests in LB medium supplemented with $ZnCl_2$. BL21 (DE3) pLysS *E. coli* transformed with, *A*, pET6H-TEV-ZnT8cR or, *B*, pET6H-TEV-ZnT8cW, were grown to OD_{600} = 0.6 in unsupplemented LB medium and then transferred to LB medium supplemented with 0-10 mM $ZnCl_2$. The cultures were then induced with 0.5 mM IPTG overnight at 16 ^{o}C at 200 rpm on an orbital shaker. Soluble protein was extracted and analysed by western blot using an anti-His tag primary antibody. The position of Precision Plus protein standards (BioRad) are indicated on the left in kDa. These expression tests were not repeated (n = 1).

3.3.3.4 Double colony selection

The total protein expression of several individual colonies of SoluBL21™ *E. coli* transformed with both variants of ZnT8c was analysed by SDS-PAGE following overnight induction at 16 ^{o}C. The lysis buffer volume and gel loading conditions were identical for all preparations. In the first round of colony selection, the lanes containing lysate from colonies R_2 and W_2 stained strongest with Coomassie R250 (Appendix IX). The glycerol stocks prepared from these colonies were used to streak a second LB-ampicillin agar plate and the second round of colony selections carried out. The glycerol stock containing the highest expressing SoluBL21™ colony for each ZnT8c

variant from this second round of selection was used for all high-yield ZnT8c protein expression described herein.

3.3.4 Soluble protein purification

Highly expressing glycerol stocks of SoluBL21™ *E. coli* transformed with either ZnT8c variant were used to inoculate 2 L cultures and induced with 0.5 mM IPTG for 42 h at 16 ^{o}C at 200 rpm on an orbital shaker. Extraction of soluble protein required two sequential purification steps; affinity purification and size exclusion chromatography. The lysis procedure and buffers are described in General Methods (section 2.3). ZnT8cR protein from various stages of purification was analysed using SDS-PAGE and stained with Coomassie R250 (n = 3, Fig. 3.6A). Purification of ZnT8cW protein analysed with SDS-PAGE was very similar and is not shown (n = 3). The lane containing unpurified insoluble ZnT8cR protein contained a large band with its leading edge at approximately 13 kDa, whereas the soluble protein fractions in other lanes contained a more clearly defined band at a mass of approximately 14 kDa (Fig. 3.6A). This difference was consistent (n = 3) and may represent monomeric ZnT8cR (13.3 kDa theoretical size). The insoluble protein lane also contained two bands indicating proteins with masses of approximately 26 kDa and 33 kDa, along with further bands with masses of > 100 kDa (Fig. 3.6A, lane 1). These bands may represent SDS-resistant dimeric ZnT8cR (26 kDa) as seen in figure 3.3B and C, and other insoluble protein(s) which were not detected with anti-His antibody (33 and >100 kDa bands not present in figure 3.3B and C). The flowthrough protein fraction which did not bind to the nickel resin contained many proteins, although there appeared to be an enriched band at approximately 14 kDa which may correspond to ZnT8cR (Fig. 3.6A, lane 2). The imidazole elution fraction contained ~90% pure 14 kDa protein, however there is a faint band at approximately 26 kDa (likely dimeric ZnT8c) and some material did not enter the resolving gel (Fig. 3.6A, lane 5). Following elution from the affinity resin, ZnT8c protein was loaded onto a Superdex 75 26/60 column as described in General Methods (section 2.3). Typical size exclusion chromatograms for both ZnT8c variants (Fig. 3.6B) indicated that both affinity-purified proteins consisted of two

forms. The major elution peaks at ~41 min coincided with the void volume of the column, indicated by the elution of blue dextran during calibration of the column (Fig. 3.6C). Therefore, this protein had a mass of at least 75 kDa due to the properties of the column. SDS-PAGE analysis indicated that this protein was aggregated ZnT8c (Fig. 3.6A, lane 6). Far-UV CD indicated that this aggregated protein had a predominantly β-sheet structure (Fig. 3.6D). Both ZnT8c variant proteins had a second elution peak at approximately 71 min (Fig. 3.6B), corresponding to a mass of 34.2 kDa. The calculated monomer mass of both ZnT8c variants was 13.3 kDa, therefore this protein is ~2.6x the size of monomeric ZnT8c. Following purification with size exclusion chromatography, both ZnT8c variant proteins were ≥ 95% pure as assessed by SDS-PAGE (Fig. 3.6A, lane 7).

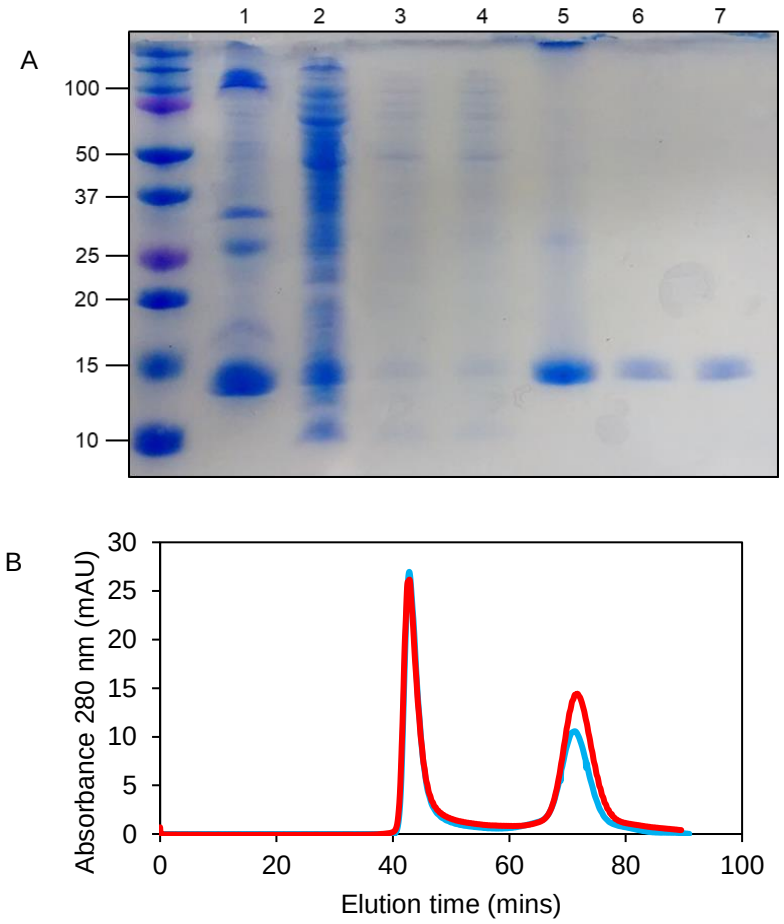

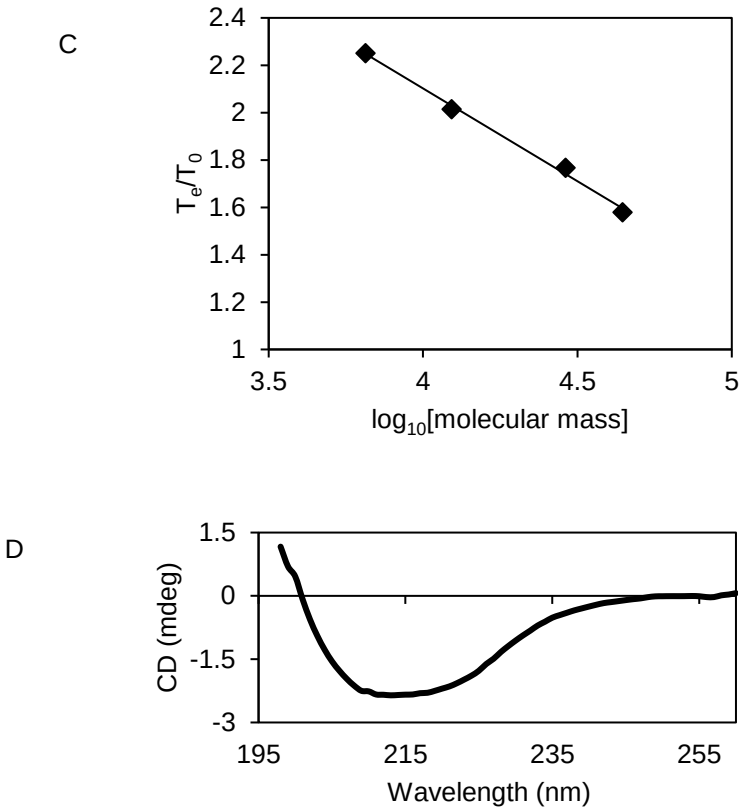

Figure 3.6. ZnT8c protein purification. *A*, Representative (n = 3) SDS-PAGE analysis of ZnT8cR protein purification steps. Lane 1 contains the insoluble protein fraction; lane 2 contains the soluble protein that did not bind to the Ni-resin; lanes 3 and 4 contain Ni-resin wash steps 1 and 2 respectively; lane 5 contains the elute fraction from the Ni-resin; lane 6 contains protein eluting from size exclusion at ~41 min in *B*; lane 7 contains protein eluting from size exclusion at ~71 min in *B*. The position of Precision Plus protein standards (BioRad) are indicated on the left in kDa. *B*, Typical (n > 3) size exclusion chromatograms using a Superdex S75 26/60 column of ZnT8cR (blue) and ZnTcW (red) proteins. Both variants had a major elution peak at ~41 min, i.e. the column void volume, and a second peak at ~71 min corresponding to 34.2 kDa protein. *C*, Semi-logarithmic plot of calibrant size used for estimation of ZnT8c protein size (n = 1). Calibrants used were bovine lung aprotinin (6.5 kDa), equine heart cytochrome c (12.4 kDa), bovine carbonic anhydrase (29 kDa), chicken ovalbumin (44.3 kDa). Column void volume was identified using blue dextran (> 2000 kDa). *D,* representative (n = 3) far-UV CD spectrum of ZnT8cR protein from the ~41 min peak in *B*. Similar results were obtained for ZnT8cW samples. Far-UV analysis of the peak eluting at 41 min is described and analysed in Chapter 4.

3.3.5 Protein concentration determination

Dilute size exclusion fractions were concentrated using 15 ml 3 kDa MWCO centrifugal concentrators (Merck Millipore; section 2.3). The concentration of pure ZnT8c protein was measured both spectroscopically using a Nanodrop 2000 instrument and spectrophotometrically using a modified Bradford assay (section 2.4; (Zor & Selinger, 1996). The extinction coefficients of 13,980 M^{-1} cm^{-1} and 8480 M^{-1} cm^{-1} for ZnT8cW and ZnT8cR, respectively, were calculated from the primary protein sequences (Table 3.1). Following optimisation of the expression protocol, a typical yield of either ZnT8c variant was 0.5 mL of 200-250 µM protein; approximately 1 mg per L of culture.

3.3.6 Native PAGE

The oligomeric state of both ZnT8c variant proteins was assessed by native PAGE (section 2.8.3, Fig. 3.7). Calculating the Rf values for the standards and the samples indicates that for both ZnT8c variants, the untreated proteins had a mass of approximately 26 kDa.

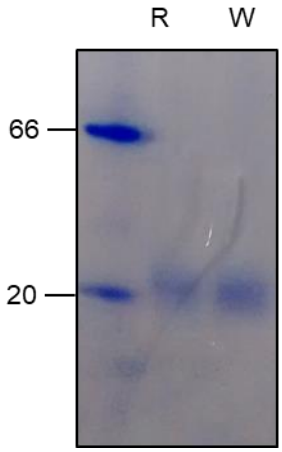

Figure 3.7. Both ZnT8c variants formed dimers. Native PAGE analysis (n > 3) of ZnT8cR ('R') and ZnT8cW ('W') indicates that both proteins had a molecular mass of approximately 26 kDa. The position of NativeMark protein standards (Thermo) are indicated on the left in kDa.

3.3.7 DTNB assay

The two ZnT8c protein variants contain three cysteine residues at the C-terminus. Following the protocol outlined in section 2.3, ZnT8c protein was purified in a buffer containing reducing agent. To remove the reducing agent, the protein was washed using degassed buffer free of reducing agents (50 mM Tris/HCl, pH 8, 300 mM NaCl, 100 mM sucrose, 100 µM TCEP). DTNB assays indicate that immediately following this washing step, both ZnT8c variants contained three free sulfhydryls and confirmed that the three cysteine residues in the proteins were reduced (Table 3.3).

Table 3.3. DTNB assays were used to calculate the number of free sulfhydryls per ZnT8c monomer post purification (n = 3).

Variant	Free S^-/monomer
ZnT8cR	2.8 ±0.3
ZnT8cW	2.7 ±0.2

3.3.8 C-terminal constructs

Despite considerable optimisation of the expression conditions, the majority of ZnT8c protein was expressed in an insoluble form in bacteria (Fig. 3.6A), and a considerable proportion of the soluble protein was aggregated (Fig. 3.6B). One hypothesis was that this tendency for aggregation and insoluble protein production was caused by the 3 cysteine residues at the C-terminus (C361, C364 and C368) forming various inter- and/or intra-protomer disulphide bonds and therefore disturbing the native protein fold. Plasmids encoding residues 267-359, 267-358 and 267-356 of ZnT8 R325 were constructed from the pET6H-TEV-ZnT8cR backbone (section 2.2, Table 2.4). Expression tests conducted using BL21(DE3)pLysS *E. coli* (this strain was used as the beneficial effects of SoluBL21 were not known at this stage) induced with 0.5 mM IPTG overnight

at 16 °C at 200 rpm indicated that removing the region containing the cysteine residues did not significantly improve the expression of soluble ZnT8cR protein (Fig. 3.8). The molecular biology to create the plasmids, the protein expression tests, and the SDS-PAGE analysis, were all carried out by the Protein Production Facility (King's College London).

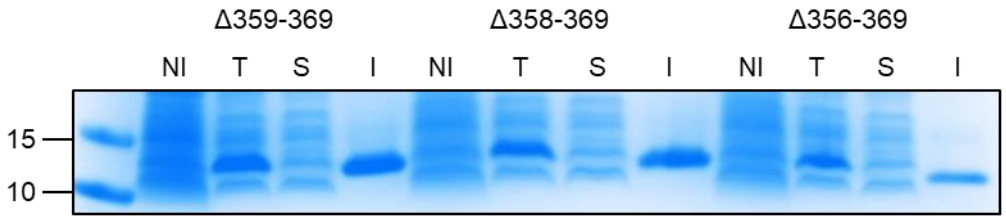

Figure 3.8. Expression tests of three ZnT8cRΔCterm constructs. BL21(DE3)pLysS *E. coli* transformed with pET6H-TEV-ZnT8cRΔCterm encoding ZnT8 residues 267-358 (Δ359-369), 267-357 (Δ358-369) or 267-355 (Δ356-369), were grown to OD_{600} of 0.6 in LB medium and induced with 0.5 mM IPTG overnight at 16 °C at 200 rpm on an orbital shaker. Non-induced samples (NI) were grown overnight in the absence of IPTG. Total (T) protein extracted from the induced samples was separated into the soluble (S) and insoluble (I) fractions following cell lysis. The position of Precision Plus protein standards (BioRad) are indicated on the left in kDa. These expression tests were not repeated (n = 1).

3.3.9 Protease cleavage

The pET6H-TEV-ZnT8c plasmids encoded a TEV protease cleavage site between the hexahistidine tag and the ZnT8 CTD (Fig. 3.1). Several attempts were made to produce cleaved soluble ZnT8c protein; modifying incubation time and temperature, buffer constituents (for instance including 0.1% (v/v) Tween-20 in the reaction buffer), and two different commercially available TEV proteases. Several steps from a typical protease cleavage reaction for both ZnT8c variants were analysed by SDS-PAGE (Fig. 3.9). Both ZnT8c variants, prior to the addition of the protease, had two bands with approximate masses of 14 and 22 kDa, corresponding to monomeric and a small

quantity of SDS-resistant dimeric ZnT8c. Following incubation of ZnT8c protein with ProTEV Plus protease (Promega), two additional bands with approximate masses of 50 kDa and 12.5 kDa appeared. The expected mass of the protease was 48 kDa, while the expected mass of the cleaved ZnT8c product was 11.4 kDa (Table 3.1). The presence of cleaved ZnT8c indicated that the proteolysis occurred. Following centrifugation of the mixture post-cleavage (Fig. 3.9A and B, lane 3) the band at 12.5 kDa was lost, suggesting that the ZnT8c cleavage product precipitated and was removed during centrifugation. There was also a significant decrease in the amount of protease in the solution following this centrifugation step. Nickel affinity resin was used to remove the uncleaved ZnT8c, cleaved hexahistidine tag, and the his-tagged TEV protease (section 3.2.4). However, following treatment with the resin, the solution appeared to contain mostly uncleaved ZnT8c monomer and dimer, similar to the ZnT8c sample prior to addition of protease. The elution from the affinity resin verified that this method was efficient at removing both uncleaved ZnT8c and the tagged protease (Fig. 3.9A and B, lane 5) from the cleavage reaction. Several of the lanes containing ZnT8cR protein contained an additional band at approximately 16 kDa (Fig. 3.9A, lanes 1-4). It is not clear what this band corresponds to, although such a band was not been seen on any other SDS-PAGE analysis of ZnT8c protein so can be assumed to be an artefact specific to this gel.

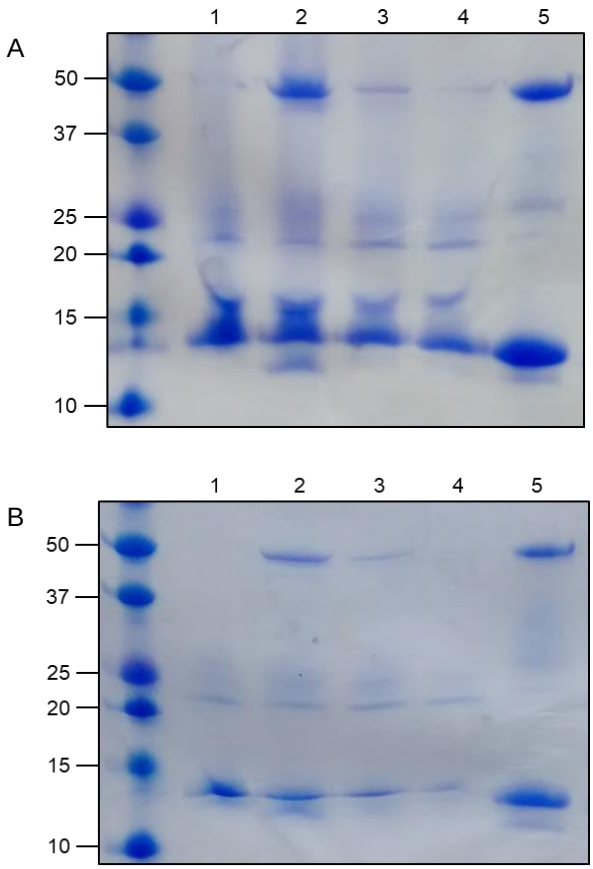

Figure 3.9. ZnT8c protease cleavage. The two variant ZnT8c proteins (*A*, ZnT8cR, and *B*, ZnT8cW) were incubated with ProTEV™ protease for 75 min at 20 °C and subsequently purified using Ni-resin. Aliquots were taken at various points during the process and analysed with SDS-PAGE. Full length ZnT8c protein has an expected size of 13.3 kDa and the cleaved protein has an expected size of 11.4 kDa. Lane 1 contains ZnT8c protein without addition of protease; lane 2 contains protein post-cleavage; lane 3 contains post-cleavage protein spun at 14,000 x *g* for 5 min to remove precipitates; lane 4 contains spun protein that did not bind to Ni-resin; lane 5 contains protein eluted from the Ni-resin with imidazole. The position of Precision Plus protein standards (BioRad) are indicated on the left in kDa. These gels are representative of several repeats (n > 3).

3.4 Discussion

The CTD of ZnT8 is the location of a mutation encoding Arg replacing Trp at position 325, which increases the risk of developing of both type 2 (Rutter & Chimienti, 2015) and gestational diabetes (Ziqi Lin et al., 2018), while significantly altering the epitope recognised by

autoantibodies in type 1 diabetes (Wenzlau et al., 2008). Neither the recombinant expression of any mammalian ZnT CTD or the biochemical effects of this mutation on the CTD of ZnT8 have previously been described. Therefore, bacterial expression plasmids were designed which encoded the two common variants of the CTD of ZnT8 (R325 and W325, residues 267-369) and the expression of the two proteins was optimised.

Initial expression tests with pET6H-WELQ-ZnT8cR indicated that this protein was predominantly expressed in insoluble inclusion bodies. One benefit of using recombinant proteins expressed in inclusion bodies is that they can be isolated in a highly pure form from *E. coli* without additional purification steps, due to the low expression level of endogenous insoluble proteins (Burgess, 2009). His-WELQ-ZnT8cR inclusion bodies were >85% pure following washing (Fig. 3.2, A, lane 3). Refolding the His-WELQ-ZnT8cR protein using a 6-0 M urea gradient produced a low yield of protein rich in β-sheet structure. Interestingly, similar CD spectra were obtained for aggregated soluble ZnT8c protein isolated with size exclusion chromatography (expressed using different plasmid and conditions, Fig. 3.6D). These data suggest that while the protein appeared to be misfolding during refolding (i.e. forming a non-native fold), it may have been forming a specific conformational state (Ventura & Villaverde, 2006). It is not known whether this protein conformation forms in the CTD of endogenous mammalian ZnT8.

It is possible that optimisation of the inclusion body refolding protocol would have resulted in production of a higher yield of correctly folded ZnT8c protein. However, concomitant expression tests using the pET6H-TEV-ZnT8c plasmids indicated that these constructs enabled production of soluble ZnT8c protein. Therefore, the decision was taken to optimise soluble protein expression using the pET6H-TEV-ZnT8c plasmids, rather than continue with the pET6H-WELQ construct. This difference in soluble/insoluble protein expression indicates that the N-terminal extension chosen influences the protein folding. Therefore, while ZnT8c protein expressed using the pET6H-TEV plasmids was partially soluble, further alterations to the N-terminal extension may have greatly improved the soluble protein expression.

Three other parameters had significant impacts on the yield of soluble ZnT8c protein; induction time, induction temperature and *E. coli* strain. For instance, ZnT8cR did not express at all in Arctic Express, whereas there was relatively high yield of soluble ZnT8cR in both BL21(DE3)pLysS and SoluBL21™ (Table 3.2). Several of the strains tested are advertised as having been optimised for expression of difficult or toxic proteins through various genetic modifications (Table 2.3). For instance, the T7 lysozyme encoded by the pLysS plasmid in BL21(DE3)pLysS inhibits T7 RNA polymerase to prevent uninduced expression of the protein of interest. This prevents long-term build-up of toxic proteins in the bacteria, which would provide a seed for aggregation and precipitation of the protein of interest during the induction period. The genome of SoluBL21™ *E. coli*, the strain which produced the greatest yield of soluble ZnT8c protein, is proprietary. The strain is derived from BL21(DE3) and contains uncharacterised mutations selected through "special" selection criteria (datasheet provided in Appendix X). However, the beneficial effects on ZnT8c expression of a low induction temperature and a long induction time suggest that the unknown mutations in SoluBL21™ have a similar effect to pLysS and work to reduce the rate of protein expression. The mutations could also affect the expression of endogenous protein chaperones, which can improve folding of the recombinant protein of interest (Georgiou & Valax, 1996).

LB medium is a complex growth medium that contains sufficient trace elements, including zinc, to maintain bacterial growth (Outten & O'Halloran, 2001). While LB medium contains approximately 10 µM zinc, *E. coli* grown in LB medium accumulate approximately 200 µM total zinc (Outten & O'Halloran, 2001). Addition of $ZnCl_2$ to LB culture medium did not improve the expression of soluble ZnT8c protein of either variant. The metal content of ZnT8c expressed in an insoluble form was not measured. Therefore, it may be the case that if ZnT8c does bind zinc, it is in a form which is outcompeted for Zn^{2+} by native bacterial proteins during its residence in *E. coli*. It may also be the case that binding to zinc in this environment causes ZnT8c to become insoluble. However, since the majority of ZnT8c was expressed in an insoluble form, had this

protein contained a significant amount of zinc it would be expected that this would cause zinc depletion in the bacteria and therefore zinc supplementation of the growth medium would have had a beneficial effect on protein expression, which it did not. The expression of three bacterial CDF CTD proteins did not require supplementation of the growth medium with zinc (Hattori et al., 2007; Höfer et al., 2007; Zeytuni et al., 2012), although the exact ingredients of the growth medium are not specified in these studies.

SDS-PAGE analysis of the ZnT8c purification steps shows that the protein is >95% pure following affinity purification. However, size exclusion chromatography shows that this sample is a mix of aggregated ZnT8c of molecular mass ≥75 kDa, and ZnT8c with a molecular mass of approximately 35 kDa. The expected mass of ZnT8c is 13.3 kDa, so the protein eluting at approximately 71 min during SEC has an apparent mass 2.6x that of the monomer, indicating either dimeric or trimeric protein. However, when this fraction from either variant is analysed by native PAGE, the molecular mass is 26 kDa, 2.0x the predicted monomer mass, indicating that both ZnT8c variants form dimers. Both *T. thermophilus* CzrB (Cherezov et al., 2008) and *M. gryphiswaldense* MamM (Zeytuni et al., 2014) CDF CTDs elute during size exclusion chromatography as dimers, although there was not such a large disparity between actual/predicted mass for these proteins. Both native PAGE and size exclusion chromatography measure the size and shape of a protein (i.e. Stokes radius). Native PAGE also separates proteins based on charge, but both native PAGE and size exclusion chromatography were carried out at approximately pH 8, so both ZnT8c variants would have a uniform negative charge (>2 pH units above the protein pI, Table 3.1). Since the running conditions are similar, it is not clear what causes the difference in apparent protein mass between these two techniques.

Despite low sequence identity, the CTDs of most human ZnTs are predicted to form a conserved αββαβ ferredoxin-like fold (Fig. 1.9; (Parsons et al., 2018). Such a fold is also found in globular cytosolic metalloproteins, for instance in iron-sulfur cluster-containing proteins (Orme-Johnson, 1973) and copper chaperones (Pufahl et al., 1997), indicating that the transmembrane domains

of the ZnTs may not be necessary for the CTDs to fold correctly and be soluble. Indeed, individual CTDs from bacterial CDF homologues have previously been isolated (Cherezov et al., 2008; Higuchi et al., 2009; Zeytuni et al., 2012). Far-UV CD data indicate that the aggregated ZnT8c eluting from size exclusion chromatography in the void volume is formed of predominantly β-sheets, indicating that this protein is not forming the correct αββαβ fold. Some SDS-PAGE gels presented in this chapter contain a minor proportion of ZnT8c protein which forms SDS-resistant dimers, for instance the insoluble protein expressed with BL21(DE3)pLysS (Fig. 3.3, Lane 4), and soluble ZnT8c protein prior to protease cleavage (Fig. 3.9, Lane 1). In the latter case, this protein had been previously purified using size exclusion chromatography, indicating that over time ZnT8c will form these β-sheet rich structures. Interestingly, SDS-PAGE analysis of full-length ZnT8 also indicates the presence of SDS-resistant dimers (Nicolson et al., 2009). Perhaps the tendencies of the isolated ZnT8 CTDs to form these β-sheet rich conformers translate to the full-length protein.

Despite removal of a considerable amount of aggregated protein using size exclusion chromatography, there is a tendency for both purified ZnT8c protein variants to aggregate and ultimately precipitate after approximately 2 weeks. Addition of fresh TCEP to the buffers during protein purification is necessary to obtain a high yield of dimeric protein. This suggests that the protein aggregation is, at least in part, due to self-association via the C-terminal cysteine residues. These cysteine residues are only conserved in the vesicular subfamily of mammalian ZnTs (Fig. 1.9; (Parsons et al., 2018). Predictions of secondary structure in human ZnTs reveal that the C-terminal 10-12 residues are not predicted to form any secondary structure (Fig. 1.9). However, expression of ZnT8cR constructs missing various lengths of this unstructured C-terminal tail (encompassing the cysteine residues), did not significantly increase the expression of soluble protein; the majority of the expressed protein was still insoluble. Therefore, the expression of ZnT8c in the insoluble fraction is not related to the cysteine residues. Interestingly, due to the removal of the cysteine residues, these ΔCterm constructs also do not contain one of

two high affinity zinc binding sites (Fig. 1.9; (Parsons et al., 2018), although the metal binding characteristics of these particular protein constructs were never investigated. These constructs were tested very early on in the project by a separate facility (Protein Production Facility, King's College London) and were focussed solely on improving soluble protein yield; metal binding experiments were undertaken much later in the project after we had established a protocol for a high yield of soluble protein expression.

ZnT8c protein concentrations were determined with direct spectroscopic measurement, based on theoretical extinction coefficients, or with a modified Bradford assay using BSA as the standard (section 2.4). Neither of these techniques provide a truly reliable measure of protein concentration (Knight & Chambers, 2003). For correct direct spectroscopic measurements, the theoretical extinction coefficient should have been confirmed experimentally, for instance using mass spectrometric amino acid analysis. Bradford dye binds to basic residues such as arginine and lysine (Bradford, 1976). Accuracy with this assay depends on the protein of interest containing a similar amount of these residues to the standard protein used (Knight & Chambers, 2003). In this case BSA was used as the standard, which contains many more basic residues than ZnT8c, whereas a known concentration of ZnT8c (following amino acid analysis) should have been used as the standard. This is particularly important for ZnT8c, as the R325W mutation leads to a 1/8 loss of basic residues (five Lys, three Arg in ZnT8cR, five Lys, two Arg in ZnT8cW).

The cleaved ZnT8c product (either variant) of the TEV protease reaction was insoluble and could not be used for downstream applications. The increased propensity of the cleaved ZnT8c proteins to precipitate indicates that the hexahistidine tag and/or the TEV protease site stabilise the His-ZnT8c proteins. The three bacterial CDF CTD homologues were all expressed with hexahistidine tags, and two of the three reports describe successful removal of the tag (Hattori et al., 2007; Höfer et al., 2007; Zeytuni et al., 2012); it is not clear whether the tag was removed from $TM0876_{206–306}$ (Hattori et al., 2007). This suggests that cleaved ZnT8c proteins (residues 267-369) are not stable. Residues 267-369 of ZnT8 were expressed because of the prediction of

these residues to form the totality of the CTD (Fig. 1.9). However, recombinant protein solubility can be substantially altered by the addition or removal of one or more residues. It is possible that removal of only a certain portion of the N-terminal region of ZnT8c would have rendered the cleavage product soluble. Mammalian proteins which also form a ferredoxin-like fold, such as the human copper chaperone Atox1 (Belviso et al., 2016), have also been successfully expressed in *E. coli*, suggesting that this type of fold is not dependent on eukaryotic post-translational modifications. Hexahistidine tags are unlikely to alter the 3D structural characteristics of the bound protein of interest (Carson et al., 2007), therefore the decision was taken to use His-TEV-ZnT8c protein for structural investigations. However, the zinc binding characteristics of the His-TEV-ZnT8c protein are affected, as the hexahistidine tag binds Zn^{2+}. Ideally all experiments would have been conducted using cleaved ZnT8c protein, but useful conclusions can still be drawn from data collected using His-ZnT8c protein.

In conclusion, the recombinant expression and purification of the two common variants of the CTD of human ZnT8 in bacteria has been optimised. This work was the underpinning of the first published account of the isolation of any mammalian ZnT CTD. Despite large optimisations, such as choosing the correct *E. coli* strain and induction conditions, and small optimisations, such as selecting highly-expressing colonies with double colony selection, the majority of the ZnT8c protein was still expressed in an insoluble form. A considerable portion of the purified soluble ZnT8c protein was formed of misfolded aggregates and needed to be further processed to purify the dimeric protein. These limitations on yield were not shared by the bacterial homologues isolated elsewhere. However, sufficient soluble protein was produced to characterise various structural and functional characteristics of the diabetes-risk and diabetes-protective ZnT8c protein variants.

4. Structural features of the two ZnT8 CTD variants

Abstract

The ferredoxin-like fold formed by the bacterial CTDs is predicted to be conserved in ZnT8c. The bacterial CTD proteins form V-shape dimers which are stabilised by dimerisation contacts in a loop between sheet β2 and helix α2. The corresponding loop in ZnT8c contains residue 325. This chapter shows that both ZnT8c variants likely form the ferreodoxin-like fold and form stable dimers. Residue 325 affects both dimer formation and stability. Fluorescence measurements indicate that W325 is solvent accessible. The results presented in this chapter begin to provide the molecular basis for the altered diabetes risk caused by the full-length ZnT8 proteins.

4.1 Introduction

The CTD of the CDF family purportedly senses cytosolic zinc, channels zinc to the transport site in the TMD, and mediates protein-protein interactions. In addition to the elucidation of the 3D structure of the full-length *E. coli* YiiP, the structures of three bacterial CDF CTDs have been elucidated independently of the TMD. These structures, along with structural predictions of the mammalian ZnTs, indicate that the ferredoxin-like fold of the CTD is largely conserved. This fold is also found in many other metal-binding domains, albeit with the metal-binding sites in different locations (Blindauer, 2015). In the bacterial CDF CTDs, one of the two conserved zinc-binding sites is formed of ligands from both CTD protomers in the dimer. Occupancy of this inter-protomer binding site with Zn^{2+} provokes a conformational change in the transporter, allowing zinc transport to occur (Lu et al., 2009). The mammalian ZnTs are thought to function with the same general transport mechanism, utilising a proton gradient to drive Zn^{2+}/H^{+} antiport, as shown for ZnT1 (Shusterman et al., 2014). However, the inter-protomer zinc binding site is not conserved in mammalian ZnTs (Fig. 1.9), suggesting that the role of the CTD is different to that in bacteria.

The CTD is the location of several disease-causing mutations in human ZnTs, including L349P in ZnT10 leading to hypermanganesemia (Tuschl et al., 2012), T288S in ZnT2 leading to transient neonatal zinc deficiency (Alam et al., 2015), R298C in ZnT3 leading to febrile seizures (Hildebrand et al., 2015), and W325R in ZnT8 increasing risk of developing both type 2 (Rutter & Chimienti, 2015) and gestational diabetes (Ziqi Lin et al., 2018). The W325R mutation alters the zinc transport function of ZnT8, although exactly how the mechanism is altered is not clear; specific liposome compositions were required to reveal transport differences between the two ZnT8 variants (Merriman et al., 2016), while no difference in transport was detected between the two ZnT8 variants expressed in *X. laevis* oocyte assays (Carvalho et al., 2017). The W325R mutation in ZnT8 also affects autoantibody specificity in type 1 diabetes (Wenzlau et al., 2008), indicating that the structural conformation of ZnT8 CTD is altered by the mutation.

The first aim of this chapter is to assess the similarities and differences between the mammalian and bacterial CDF CTDs. The second aim is to elucidate the biochemical effects of the W325R mutation on the CTD of ZnT8. For instance, the overall fold of the CTD is not likely to be affected, but the presence of residue 325 in the dimer interface site may affect dimerisation of the proteins.

4.2 Methods

4.2.1 Nano differential scanning fluorimetry (nDSF)

Protein thermal stability was also measured using nDSF, which utilises intrinsic protein fluorescence to follow denaturation events. Apo-protein samples were diluted to 5 µM in 10 mM Tris/HCl, pH 8, 60 mM NaCl, 20 mM sucrose, 2 mM DTT and loaded into nDSF-grade standard capillaries (NanoTemper Technologies, Munich, Germany). The ratio of fluorescence emission intensities at 330 and 350 nm was measured between 20-85 ^{o}C with a heating rate of 1 ^{o}C min^{-1} using a Prometheus NT.48 instrument (NanoTemper Technologies). The protein melting temperatures were calculated from the first derivative of the 350/330 nm ratio.

4.2.2 Microscale thermophoresis (MST)

MST uses the relative movement of molecules in a temperature gradient to measure a change in hydration shell of those molecules with a titration of an interactant, and thus measures the affinity of the interaction. Protein samples of 20 µM were labelled with amine-reactive Monolith NT.115 labelling kit Red-NHS (#MO-L001; NanoTemper Technologies) according to the manufacturer's instructions. Labelled protein was diluted to 100 nM in 10 mM potassium phosphate, pH 8, 60 mM NaCl, 20 mM sucrose, 100 µM TCEP, 1 mM EDTA, 0.05% (v/v) Tween-20. Homodimerisation affinities were measured using a Monolith NT.115 instrument (NanoTemper Technologies) by titrating labelled ZnT8cR with 180 µM – 5.5 nM unlabelled ZnT8cR, and labelled ZnT8cW with 124 µM – 3.8 nM unlabelled ZnT8cW. All experiments were

conducted at 25 °C in standard-coated capillaries (NanoTemper Technologies). Binding affinities were calculated with MO.Affinity Analysis software (NanoTemper Technologies).

4.2.3 Protein fluorescence

Tryptophan fluorescence measurements were taken using an LS50 fluorimeter (PerkinElmer, Waltham, MA, USA), using an excitation wavelength of 295 nm, an emission range of 300-400 nm and a scan rate of 100 nm min^{-1}. Both excitation and emission slit widths were 2.5 nm. To block the cysteine residues of some samples, they were incubated with maleimide as described in General Methods (section 2.6). Protein samples were diluted to 1-3 µM in 10 mM HEPES, pH 8, 60 mM NaCl, 20 mM sucrose. The 2 mL samples were measured in 4 mL plastic fluorescence cuvettes. Protein samples were titrated with up to 3 molar equivalents of $ZnCl_2$. Emission spectra for 3 µM N-acetyl-DL-tryptophan were collected in 50 mM Tris/HCl, pH 8, 300 mM NaCl. Spectra were corrected for Raman scattering and dilution.

Protein fluorescence quenching was carried out using both potassium iodide and acrylamide. Both ZnT8 CTD variants were diluted to 2.4 µM in 10 mM HEPES, pH 8, 60 mM NaCl, 20 mM sucrose and the fluorescence measured as above. Potassium iodide stock was prepared in water and titrated into protein samples between 0-40 mM. Spectra were corrected for dilution and Raman scattering. Data were fit to the Stern-Volmer equation:

$$\frac{I0}{I} = 1 + k.\tau.[Q]$$

where I_0 and I represent the fluorescence intensity in the absence and presence of a given concentration of a quenching agent, Q, while τ is the lifetime of the fluorophore, and *k* is the bimolecular quenching rate constant. The product k.τ is the Stern-Volmer constant, denoted K_{sv}.

To detect dityrosine bonds, measurements were taken with an excitation wavelength of 325 nm and an emission range of 330-500 nm. ZnT8c samples were diluted to 7 µM in 10 mM HEPES, pH

8, 60 mM NaCl, 20 mM sucrose. L,L-dityrosine dihydrochloride was diluted to 1 µM in 1 M Tris/HCl, pH 8, and used as a positive control.

4.2.4 ^{15}N labelled protein expression

To produce labelled protein, the bacteria were grown in a defined medium in which the only source of nitrogen was provided by a pure source of ^{15}N. As both ZnT8 CTD proteins are expected to bind metal, it was also important to control the metal content of the growth medium. Preparing such a complex medium requires the constituents to be added in a certain order to avoid precipitation, particularly of the metals. Initially, 1.8 L of 50 mM Na_2HPO_4, 50 mM KH_2PO_4, 50 mM $^{15}NH_4Cl$, pH 8.1, was prepared and autoclaved. The following constituents were sterile-filtered and added under sterile conditions in order; 5 mM Na_2SO_4, 2 mM $MgSO_4$, 1 mM sodium citrate, 1x metals mix (final concentration: 170 µM EDTA, 30 µM $FeCl_3$, 3 µM $ZnCl_2$, 0.74 µM $CuCl_2$, 0.77 µM $CoCl_2$, 1.62 µM H_3BO_3), 0.4% glycerol, 0.05% D-glucose, 0.01% α-lactose, 1x basal medium eagle (BME) vitamins (Sigma). Addition of 1 mM citrate to the medium prevented the precipitation of the metals and had a marked impact on the expression of ZnT8c protein. The medium was then made up to 2 L with autoclaved ≥ 18.2 MΩ.cm water. A 10 mL LB-ampicillin starter culture was incubated overnight at 25 ^{o}C at 200 rpm on an orbital shaker. This was added to the autoinduction growth medium and the culture incubated in four 1 L Erlenmeyer flasks at 16 ^{o}C and 200 rpm on an orbital shaker for 72 hours. Purification of the labelled proteins was carried out as described in General Methods (section 2.3).

4.2.5 NMR spectroscopy

ZnT8cW NMR sample contained 150 µM ^{15}N-labelled apo-protein in 95% H_2O/5% D_2O in 50 mM Tris/HCl, pH 8, 300 mM NaCl, 100 mM sucrose, 2 mM TCEP, 1 mM EDTA. ZnT8cR NMR sample contained 100 µM ^{15}N-labelled apo-protein in 95% H2O/5% D2O in 50 mM Na_2HPO_4, pH 8, 150 mM NaCl. The ZnT8cR ^{15}N-labelled NMR sample was prepared by the Protein Production Facility (King's College London). [^{1}H,^{15}N]-HSQC spectra were collected at 298 K using a 600 MHz NMR

spectrometer. All NMR spectroscopy was conducted by collaborators at the NMR Facility (King's College London, UK; director Prof. Sasi Conte).

4.2.6 Protein crystal screens

Several attempts were made to crystallise both variants of the two ZnT8 CTD variants. Between 1.5-7.5 mg/mL protein of either variant was prepared in 50 mM Tris/HCl, pH 8, 300 mM NaCl, 100 mM sucrose, 2 mM TCEP. Protein was mixed in 1:2, 1:1 and 2:1 ratios with crystal screen buffers and robotically pipetted into 96-well 3-drop crystallisation plates (sitting-drop method). The corresponding buffer was added to each 96-well reservoir and the plates incubated at 18 ^{o}C. The screens used were JCSG-plus, Morpheus I and II, Proplex, Clear Strategy Screen I and II, Structure Screen I and II, PACT premier, Shotgun, MIDAS, H&L Chain, MemGold, and The PGA Screen, all from Molecular Dimensions (Newmarket, UK). Crystal formation was monitored regularly using light microscopy.

4.2.7 X-ray crystallography

Crystals formed were mounted in a loop and flash-cooled for storage in liquid nitrogen. X-ray diffraction data were collected at the i03 beamline at Diamond Light Source (Oxford, UK). The crystal monitoring, isolation, transfer to Diamond and X-ray diffraction were all carried out by collaborators at the University of Bath (UK; principal investigator Prof. Ravi Acharya).

4.3 Results

4.3.1 Far-UV CD

The secondary structure of the two ZnT8c variants was investigated using far-UV CD spectroscopy. The two variants yielded similar spectra (Fig. 4.1A). There were no significant differences in the spectra when the two ZnT8c variants were incubated with two molar equivalents of either Zn^{2+} or Ni^{2+}, or when the sample buffer contained 60 mM KCl instead of 60 mM NaCl. The fold-recognition algorithm BeStSel (Micsonai et al., 2015) was used to estimate

the average (n ≥ 3) secondary structure content of the two ZnT8c variants; there was no significant difference between the secondary structure content of the two variants (Fig. 4.1B). The two variants also contained similar secondary structure to the *E. coli* homologue YiiP, indicating that the secondary structure and overall fold is conserved as predicted.

A

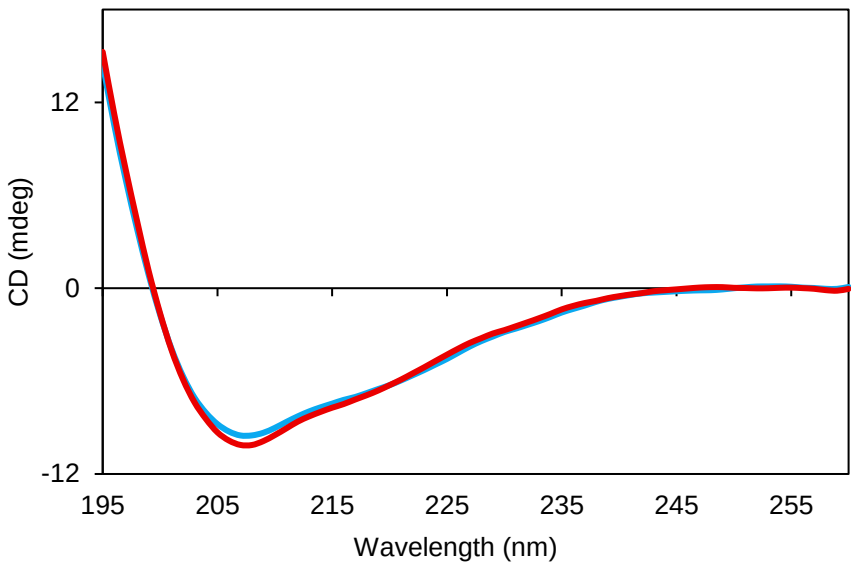

B

Structure	ZnT8cR	ZnT8cW	YiiP
α-helix (%)	18.1 ±1.2	17.8 ±2.1	24
β-sheet (%)	19.8 ±3.7	22.1 ±3.3	23
Turn (%)	12.8 ±0.1	12.4 ±1.8	n/a
Others (%)	49.4 ±2.4	47.8 ±2.8	n/a

Figure 4.1. Far-UV CD analysis of ZnT8c secondary structure. *A*, representative (n = 3) far-UV CD spectra of 0.2 mg/ml apo-ZnT8cR (blue) and apo-ZnT8cW (red) variants in 10 mM K_2HPO_4, 60 mM NaCl, 20 mM sucrose, pH 8. Far-UV CD spectra for either variant measured in the presence of either two molar equivalents of Zn^{2+}or Ni^{2+}, or with KCl replacing NaCl, were not significantly different from those of the apo-proteins. *B*, individual far-UV CD spectra for both ZnT8c variants were analysed using the fold-recognition algorithm BeStSel. YiiP secondary structure content was calculated from the 3D structure (PDB ID 2qfi). The differences in secondary structure between the two ZnT8c variants were not statistically significant.

4.3.2 Near-UV CD

Protein near-UV CD signal between 240-300 nm is largely contributed by the π-π* transition of the aromatic amino acids; Phe between 250-268 nm, Tyr between 270-280 nm, and Trp between 280-295 nm (Strickland, 1974). Signal of these residues can have both negative and positive amplitude, meaning that delineating individual near-UV CD spectra can be difficult. The exact wavelength position and signal intensity is influenced by the local environment surrounding the residue, including hydrogen bonding and hydrophobicity (Strickland, 1974). His-TEV-ZnT8cR contains four Tyr, two Phe, and one Trp residue; His-TEV-ZnT8cW contains an extra Trp. Subtraction of the apo-ZnT8cR near-UV spectrum from that of apo-ZnT8cW revealed a single negative peak at approximately 285 nm (Fig. 4.2), within the expected range for Trp residues.

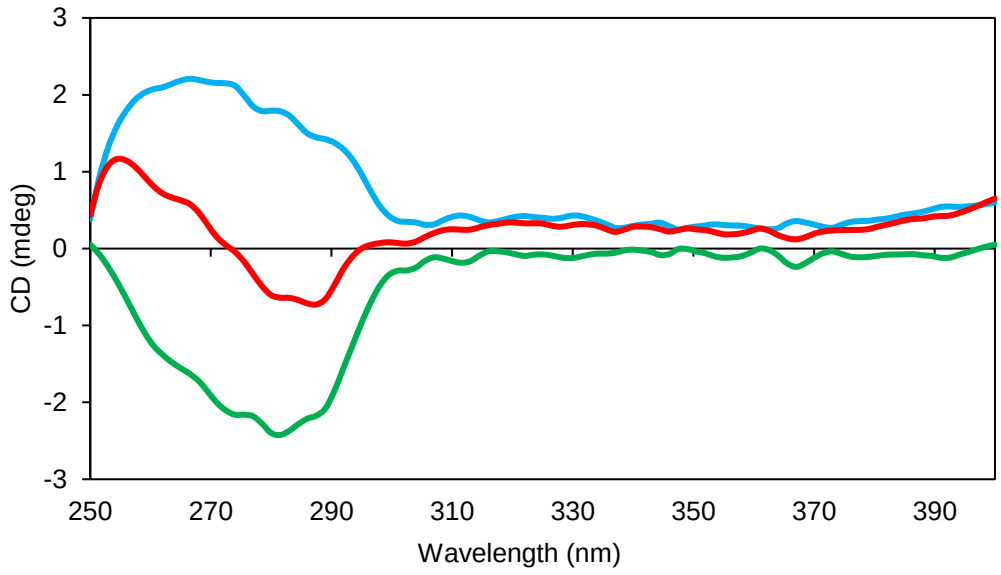

Figure 4.2. Near-UV CD of the two ZnT8c variants. Representative (n = 3) near-UV CD spectra of 0.4 mg/ml apo-ZnT8cR (blue) and apo-ZnT8cW (red). Subtracting the ZnT8cR spectra from that of ZnT8cW estimates the signal of W325 alone (green) which had a peak at approximately 285 nm.

4.3.3 ZnT8c native PAGE

Native PAGE analyses (section 2.8.3) indicate that both apo-ZnT8c variants formed dimers with a mass of 26 kDa (Fig. 4.3). Treatment of both ZnT8c variants with reducing agents did not cause a significant change in molecular mass (Fig. 4.3); therefore, both ZnT8c protein variants formed stable dimers independent of any disulphide bonds. There was no change in protein mass when the ZnT8c proteins were incubated with an excess of $ZnCl_2$ or EDTA (Fig. 4.3), indicating that ZnT8c proteins formed stable dimers independent of zinc status. However, presence of high molecular mass ZnT8c protein in the presence of excess zinc indicates that there was an increased propensity for ZnT8c proteins to aggregate in the presence of excess Zn^{2+} (Fig. 4.3). Incubation of the two ZnT8c variants with an excess of EDTA did not affect their molecular mass, indicating that the dimers did not require divalent cations other than Zn^{2+} to form (Fig. 4.3).

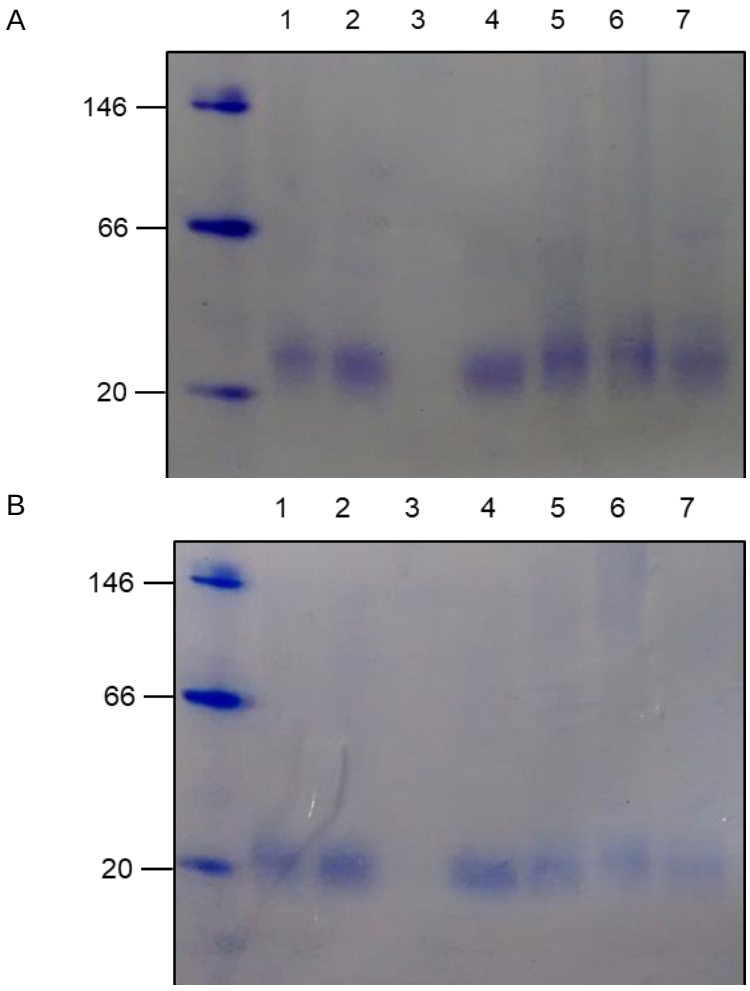

Figure 4.3. Effect of reducing agents and Zn^{2+} on the native state of ZnT8c. Samples containing, *A*, 20 µM ZnT8cR or, *B*, 20 µM ZnT8cW, were incubated with the indicated treatment for 1 hour at 21 °C. Protein was then separated using non-reducing and non-denaturing (i.e. native) PAGE and stained with Coomassie R250. Lane 1 contains untreated ZnT8c protein; lane 2 contains protein treated with 20 mM 2-mercaptoethanol; lane 3 is empty; lane 4 contains protein treated with 20 mM DTT; lane 5 contains protein treated with 2 mM $ZnCl_2$; lane 6 contains protein treated with 10 mM $ZnCl_2$; lane 7 contains protein treated with 20 mM EDTA.

4.3.4 ZnT8c dimerisation is affected by residue 325

The homodimerisation affinities of the two ZnT8c variants in the presence of EDTA were measured using MST (Fig. 4.4). Apo-ZnT8cW homodimers associated with significantly tighter affinity (1.8 ± 0.1 µM) than apo-ZnT8cR homodimers (4.3 ± 1.3 µM; n = 3, p = 0.034). Measurements of ZnT8c homodimerisation affinity in the presence of two molar equivalents of Zn^{2+} using MST yielded aberrant results, suggesting that the protein solution was heterogeneous and aggregating, making affinity analysis with this technique impossible.

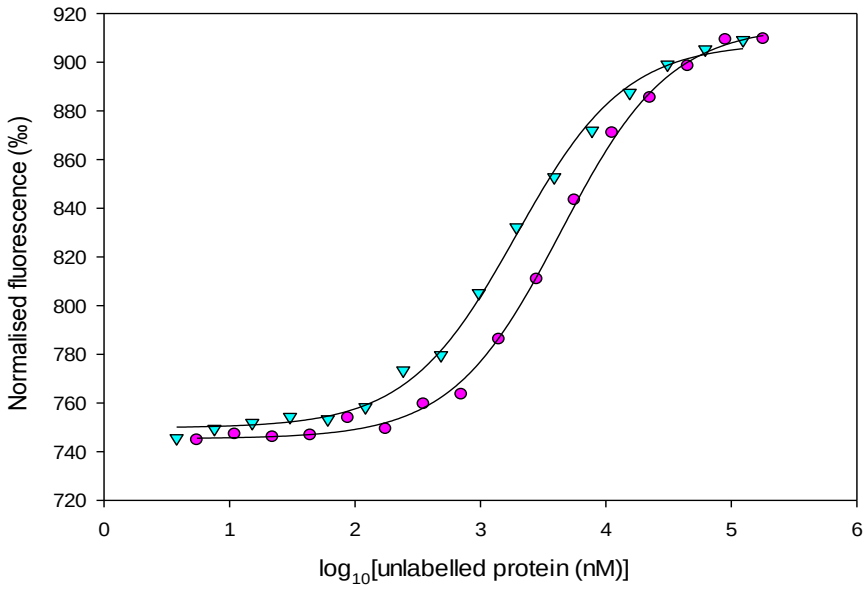

Figure 4.4. Dimerisation of the two human ZnT8 CTD variants. Representative (n = 3) microscale thermophoresis (MST) traces for dimerisation of ZnT8c proteins. Fluorescently labelled apo-ZnT8cR (100 nM, magenta circles) was titrated (in the presence of 1 mM EDTA) with unlabelled apo-ZnT8cR protein (180 µM-5.5 nM), yielding a homodimerisation K_d of 4.3 ± 1.3 µM. Fluorescently labelled apo-ZnT8cW (100 nM, teal triangles) was titrated (in the presence of 1 mM EDTA) with unlabelled apo-ZnT8cW protein (124 µM-3.8 nM), with a homodimerisation K_d of 1.8 ± 0.1 µM. There was a significant difference between the homodimerisation K_d of each variant in the presence of EDTA (n = 3, p = 0.034).

4.3.5 Dityrosine fluorescence

Dityrosine bonds in the CTDs of full-length ZnT3 and ZnT4 homodimers have been detected (Salazar et al., 2009). ZnT8c proteins contain a single tyrosine residue, although its location is not conserved with those involved in ZnT3/4 homodimerisation. Dityrosine bonds exhibit a strong fluorescence emission when excited using 325 nm, whereas tyrosine alone does not (Fig. 4.5A). There was no detectable dityrosine signal in either ZnT8cR (Fig 4.5B) or ZnT8cW (Appendix XI).

A

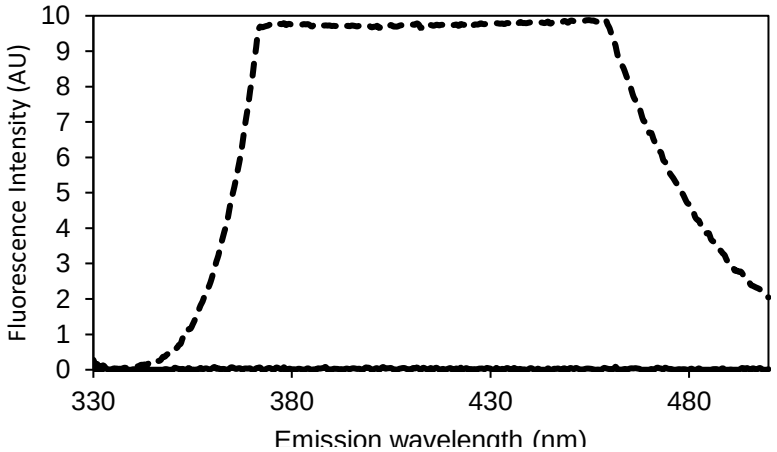

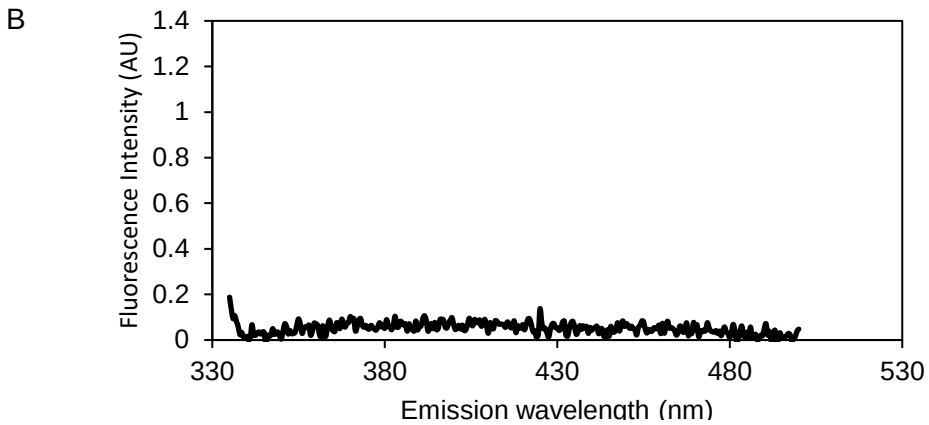

Figure 4.5. ZnT8c dimers do not contain a dityrosine bond. *A,* using an excitation wavelength of 325 nm, 1 µM dityrosine dihydrochloride (dashed line) emitted strongly at approximately 410 nm, whereas 1 µM L-tyrosine (solid line) did not. *B,* a 7 µM sample of ZnT8cR did not elicit the strong emission indicative of a dityrosine bond. Similar results were obtained using ZnT8cW (Appendix XI).

4.3.6 Protein thermostability

Both CD spectroscopy and nano differential scanning fluorimetry (nDSF) were used to investigate the melting characteristics of the two ZnT8c variants. In CD thermostability experiments, the change in signal at 222 nm measures the loss of secondary structure as a function of temperature. In nDSF experiments, the intrinsic protein fluorescence emission at 330 nm is presumed to represent fluorescent residues in folded protein, whereas emission at 350 nm represents unfolded (or denatured) protein. The ratio of these emission intensities measures protein structural changes as a function of temperature. Both techniques showed that, in the absence of Zn^{2+}, ZnT8cR was significantly more thermostable than ZnT8cW (Fig. 4.6, Appendix XII); apo-ZnT8cR T_m was 42.8 ± 0.5 ^oC, whereas the apo-ZnT8cW T_m was 41.4 ± 0.4 ^oC (n = 3, p = 0.013). In the presence of two molar equivalents of Zn^{2+}, both ZnT8c variants were significantly more thermostable than their apo forms; 2Zn-ZnT8cR T_m was 54.5 ± 2.1 ^oC and 2Zn-ZnT8cW T_m was 51.0 ± 1.8 ^oC (n = 3, p = <0.001 for both). There was no statistically significant difference between the melting temperatures of the two zinc-bound ZnT8c variants (p = 0.093). There was

no significant change in melting temperature when either ZnT8c variant was incubated with two molar equivalents of Ni^{2+}.

A

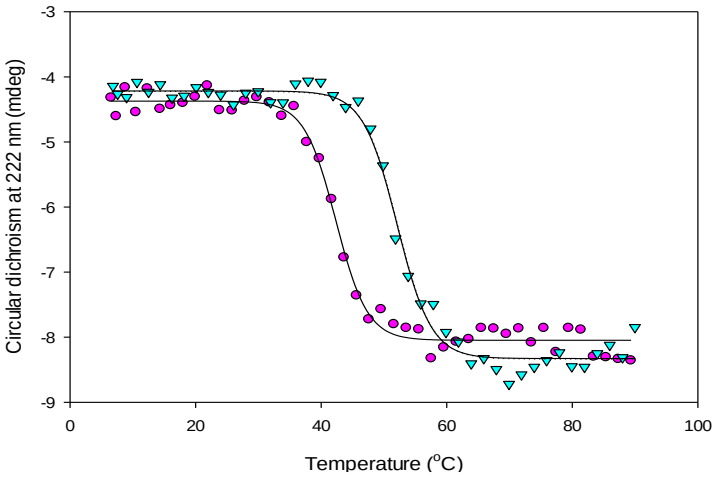

B

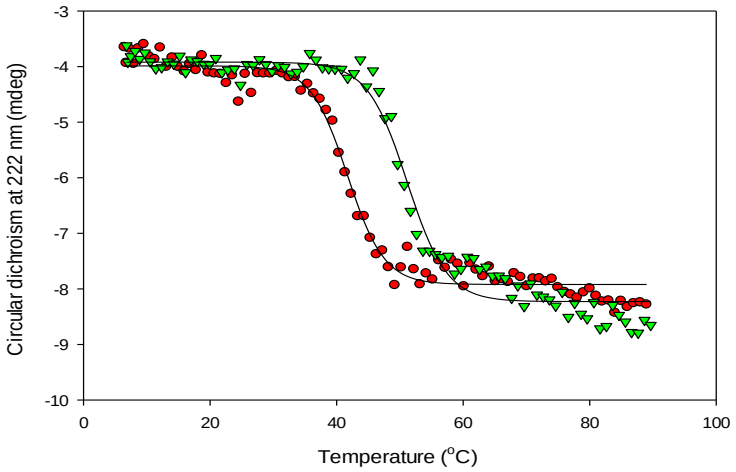

Figure 4.6. Thermostability of the two ZnT8c variants. Representative (n ≥ 3) melting curves between 6-92 °C measuring the change in CD at 222 nm for, *A*, apo-ZnT8cR (magenta circles, T_m = 42.8 ± 0.5 °C) and 2Zn-ZnT8cR (teal triangles, T_m = 54.5 ± 2.1 °C) and, *B*, apo-ZnT8cW (red circles, T_m = 41.4 ± 0.4 °C) and 2Zn-ZnT8cW (green triangles, T_m = 51.0 ± 1.8 °C). The difference in T_m measured using CD between the two apo-ZnT8c proteins was statistically significant (n = 3, p = 0.013). There was a significant difference in T_m between both apo-proteins and their zinc-bound counterparts (n = 3, p = <0.001 for both). The difference in T_m between the two zinc-bound ZnT8c proteins was not statistically significant (n = 3, p = 0.093). There was no significant change in T_m when the proteins were incubated with two molar equivalents of Ni^{2+}.

4.3.7 Tryptophan fluorescence

ZnT8cW contains two tryptophan residues (W306 and W325), whereas ZnT8cR contains one (W306). Using an excitation wavelength specific to tryptophan (295 nm), and protein samples of the same concentration, the emission spectrum of ZnT8cR can be subtracted from that of ZnT8cW to give the emission spectrum of W325 specifically. The wavelength of maximal emission (λ_{max}) for apo-ZnT8cR (and therefore W306) was 342 nm and for apo-ZnT8cW was 345 nm, whereas that of W325 specifically was 352 nm (Fig. 4.7). The solvent accessibility of a protein tryptophan residue can be elucidated using the relative blue-shift from the λ_{max} of free tryptophan. The λ_{max} of N-acetyl-DL-tryptophan in the same buffer was 363 nm. Therefore, in apo- and Zn^{2+}-bound ZnT8cW, W325 is more solvent accessible than W306.

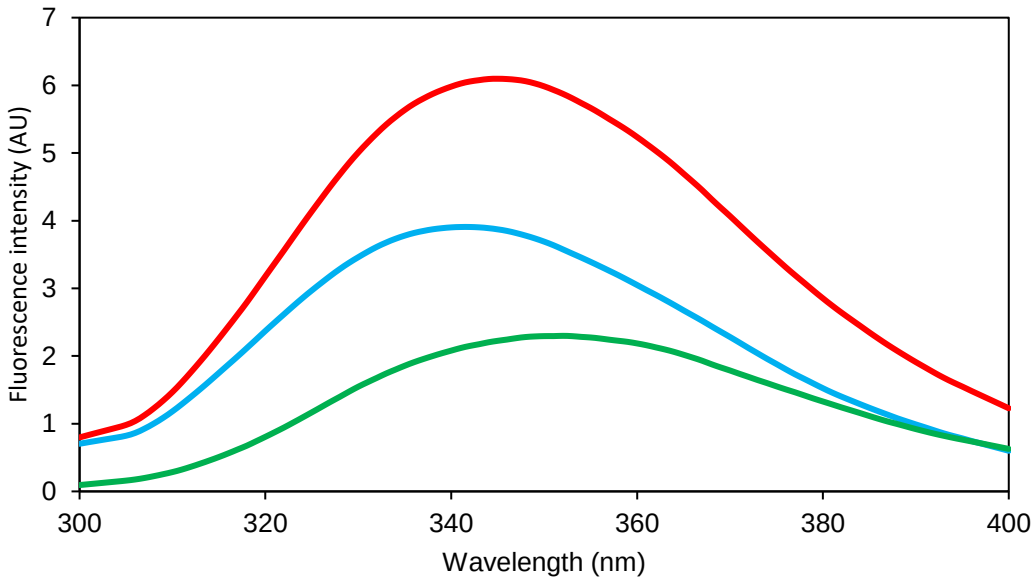

Figure 4.7. Tryptophan fluorescence of the two ZnT8c variant proteins. Representative (n = 3) fluorescence emission spectra (excitation = 295 nm) for apo-ZnT8cW (red, λ_{max} = 345 nm) and apo-ZnT8cR (blue, λ_{max} = 342 nm) samples diluted to 1.2 µM in 10 mM HEPES, pH 8, 60 mM NaCl, 20 mM sucrose. ZnT8cW contains two tryptophan residues (W306 and W325), whereas ZnT8cR contains one (W306). Subtracting the fluorescence emission spectrum of ZnT8cR from ZnT8cW therefore gives the fluorescence emission of W325 specifically (green, λ_{max} = 352 nm). All spectra were corrected for Raman scattering.

4.3.8 Tryptophan fluorescence quenching

The effects of a quencher on the fluorescence of a protein tryptophan residue can give information on the local environment of the tryptophan. Iodide ions do not penetrate the protein fold due to the charge and large hydration shell, and therefore quench surface tryptophan residues (Lehrer, 1971). The strength of quenching by iodide is related to the charge environment of the tryptophan residue. The Stern-Volmer constant (K_{sv}) is a measure of the accessibility of the tryptophan to the quencher; higher K_{sv} values indicate greater accessibility. When quenched with iodide, both ZnT8c variants elicited a biphasic response, denoted $K_{sv}1$ and $K_{sv}2$ (Fig. 4.8). There was no difference in $K_{sv}1$ or $K_{sv}2$ between the two ZnT8c variants when quenched with iodide in a buffer containing 300 mM NaCl (Table 4.1). Iodide quenching $K_{sv}1$ values for both ZnT8c variants were reduced in the presence of 2 M NaCl (Table 4.1). The quenching of N-acetyl-DL-tryptophan by iodide was not affected by changing the ionic strength of the reaction buffer.

A

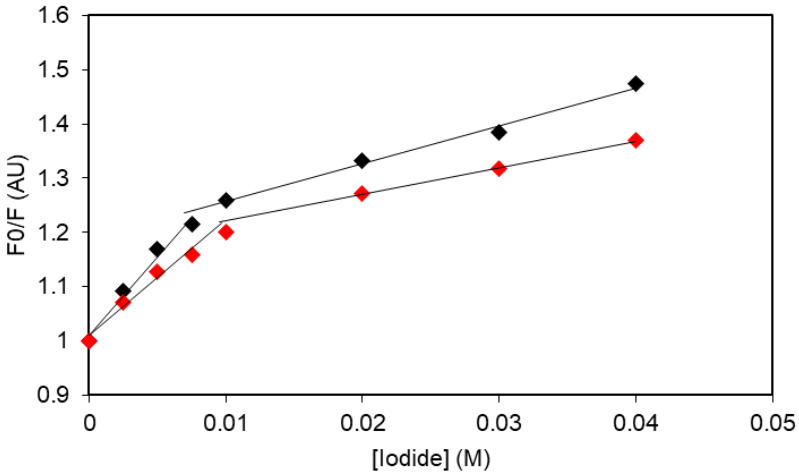

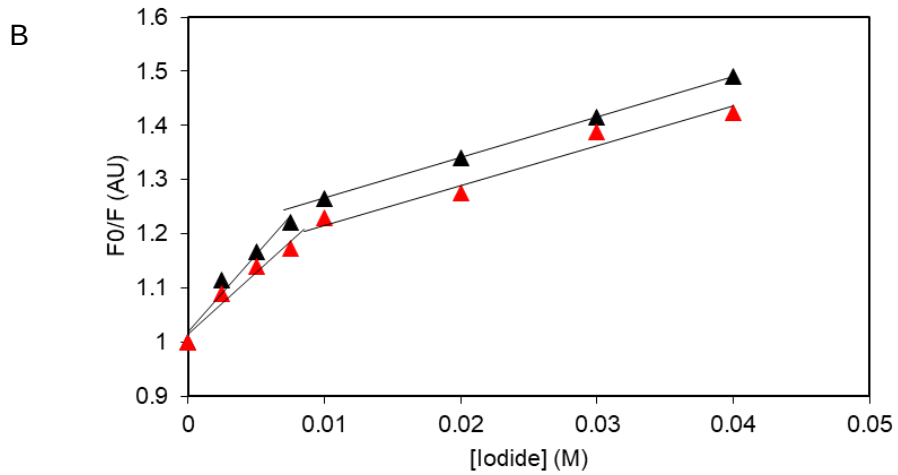

Figure 4.8. Tryptophan fluorescence quenching. Representative (n = 3) Stern-Volmer plots of 1.2 µM, *A*, ZnT8cR or, *B*, ZnT8cW in 10 mM HEPES, pH 8, 300 mM NaCl, 20 mM sucrose titrated with potassium iodide (black). Quenching of both protein variants is biphasic, indicating a charged environment surrounding the quenched Trp residue. Increasing the ionic strength of the reaction buffer from 300 mM NaCl to 2 M NaCl decreased the initial quenching component (red). The gradient of the trend lines give the Stern-Volmer constants (K_{sv}). K_{sv} values for both ZnT8c variants quenched with iodide in buffers of different ionic strength are summarised in Table 4.1.

Table 4.1. Iodide quenching of ZnT8c.

Sample	Ionic strength	Stern-Volmer constant (M^{-1})
N-acetyl-DL-tryptophan	300 mM	11.2
ZnT8cR	300 mM	Ksv1 = 28.9
		Ksv2 = 7.0
ZnT8cW	300 mM	Ksv1 = 28.6
		Ksv2 = 7.5
N-acetyl-DL-tryptophan	2 M	11.3
ZnT8cR	2 M	Ksv1 = 21.3
		Ksv2 = 5.5
ZnT8cW	2 M	Ksv1 = 22.8
		Ksv2 = 7.0

4.3.9 Minimal medium expression

ZnT8c protein of either variant expressed using the autoinduction protocol in minimal medium had a different oligomeric profile to the proteins expressed using IPTG induction in LB medium. Typical size exclusion chromatograms of either ZnT8c protein expressed in LB medium with IPTG-induction (Fig. 3.6B) contained major protein peaks at ~41 minutes (i.e. the column void volume) and at ~71 minutes (dimeric ZnT8c). However, size exclusion chromatograms of ZnT8cW expressed in minimal medium using autoinduction contained elution peaks at 41, 65, 71 and 77 minutes (Fig. 4.9). The peaks at 65, 71 and 77 minutes correspond to proteins of masses 59.6, 36.2 and 21.1 kDa; 4.5, 2.7 and 1.6 times larger than the expected mass of ZnT8cW of 13.3 kDa, respectively. The elution profiles of ZnT8cR protein expressed in minimal medium showed similar results. Addition of 1 mM sodium citrate prior to addition of the metal solution to the minimal medium prevented the production of precipitates in the medium and significantly increased the yield of soluble, dimeric ZnT8c (Fig. 4.9, 71 min elution peak). The purpose of the citrate was to buffer the supplemented metals.

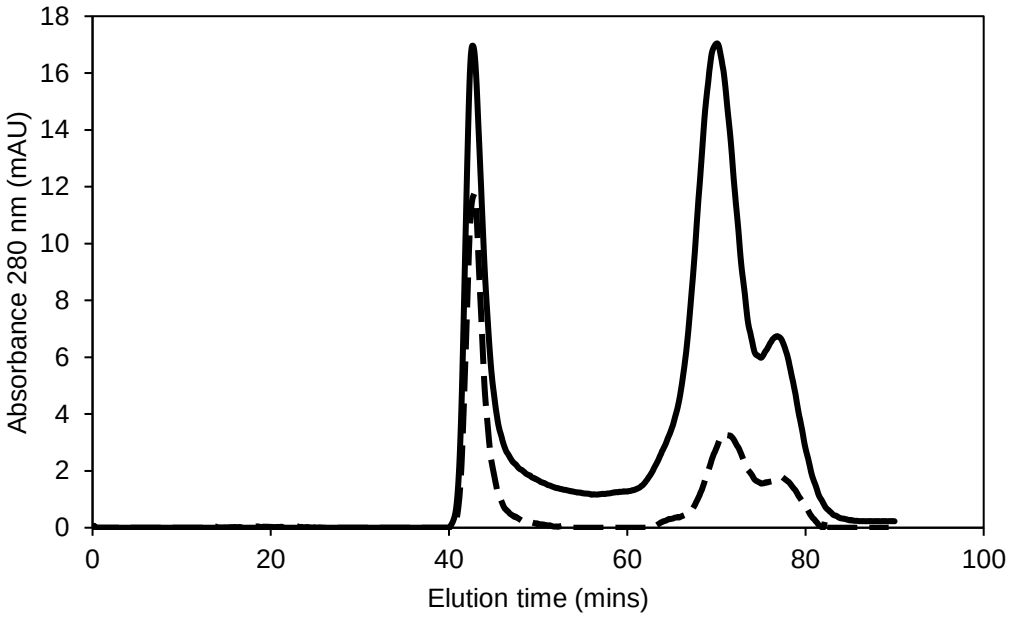

Figure 4.9. Size exclusion chromatograms of affinity-purified ZnT8cW protein expressed using autoinduction protocol. Chromatograms of ZnT8cW protein expressed using autoinduction medium containing 1x metals (as

defined in Materials and Methods, section 4.2) with (solid line) and without (dashed line) the addition of 1 mM sodium citrate. Both samples have a peak at ~41 min, i.e. the column void volume, a small peak at ~65 min, a major peak at 71 min, and a major peak at 77 min. The peaks at 65, 71 and 77 min correspond to protein of 59.6, 36.2 and 23.1 kDa respectively. The expected size of monomeric ZnT8cW is 13.3 kDa. A similar elution profile was produced by ZnT8cR protein expressed using the same autoinduction expression protocol with 1x metals and 1 mM sodium citrate. The calibration of the size exclusion column is presented in Fig. 3.6, C.

4.3.10 NMR HSQC

The optimised autoinduction protocol for protein expression was used to produce ^{15}N-labelled ZnT8c proteins. The [^{1}H-^{15}N] HSQC spectra revealed that both ZnT8c proteins are structured proteins (Fig. 4.10). However, the protein concentration (approximately 100 µM ZnT8cR and 150 µM ZnT8cW, both determined spectroscopically) and stability were not sufficient to allow further experimentation to enable assignment of specific residues. The stability of the proteins reduced when the temperature was increased from 274 to 298 K to run the spectroscopy scans (section 4.2.5). Overlay of the HSQC spectra of the two ^{15}N-labelled proteins showed that many of the resolved peaks for ZnT8cR are shifted in the spectra of ZnT8cW. However, it is not clear whether this is significant as the proteins were measured in different buffers. Tryptophan residues are typically found at a ^{1}H shift of ≥10 ppm and a ^{15}N shift of ≥128 ppm. The peak at ^{1}H 10 ppm, ^{15}N 128 ppm likely corresponds to W325 (Fig. 4.10).

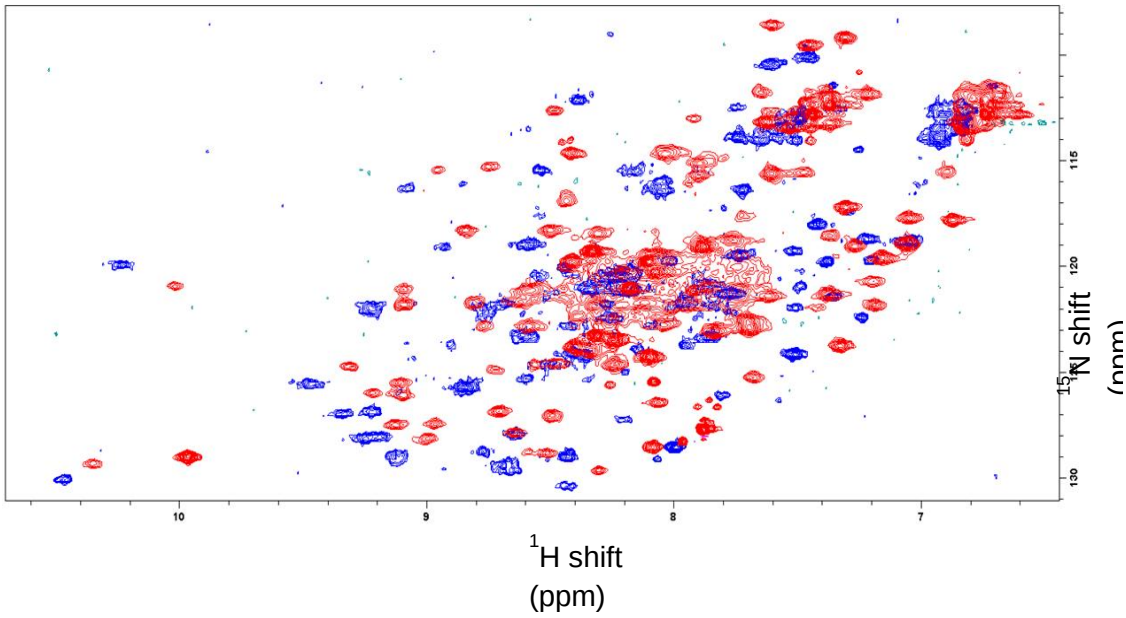

Figure 4.10. [^{1}H-^{15}N] HSQC spectra of ZnT8c proteins. ^{15}N-labelled sample of 100 µM ZnT8cR (blue) in 50 mM Na_2HPO_4, pH 8, 150 mM NaCl, and 150 µM ZnT8cW (red) in 50 mM Tris/HCl, pH 8, 300 mM NaCl, 100 mM sucrose, 2 mM TCEP, 1 mM EDTA. Both proteins were prepared in 95% H_2O/5% D_2O. Assignment of peaks to specific residues was not possible. As the proteins were measured in different buffers (both n = 1), the spectral differences seen in this figure may not be significant.

4.3.11 Crystal screens

Crystal screens were set up on several different occasions with 1.5-7.5 mg/ml of either ZnT8c variant in combination with hundreds of conditions (section 4.2.6). The majority of the conditions resulted in either clear liquid or light precipitate, indicating that the protein concentration was lower than the optimum. However, three conditions resulted in protein crystals, all with 3 mg/ml ZnT8cR. The first was produced in the JCSG F1 screen in 100 mM MES, pH 6.5, 50 mM CsCl, 30% (v/v) Jeffamine M-600. This oblong crystal was relatively large at approximately 80 x 20 µm (Fig. 4.11). No diffraction was detected with this crystal, even after carrying out grid scans (Appendix XIII). Grid scans shoot a series of points to find the optimum area of the crystal for diffraction. The second and third crystals were produced in the Heavy and Light G10 screen in 100 mM HEPES, pH 7.5, 200 mM $CaCl_2.2H_2O$, 19.6% (v/v) PEG-400. These

crystals were much smaller than the first, measuring approximately 5 x 5 µm with square morphology (Appendix XIV), and no diffraction was detected using grid scans. As no ZnT8c protein crystal diffracted under X-ray analysis, it cannot be confirmed that the crystals were protein rather than salt. If the crystals were protein, the fact that they did not diffract suggest that the crystals contained some internal disorder.

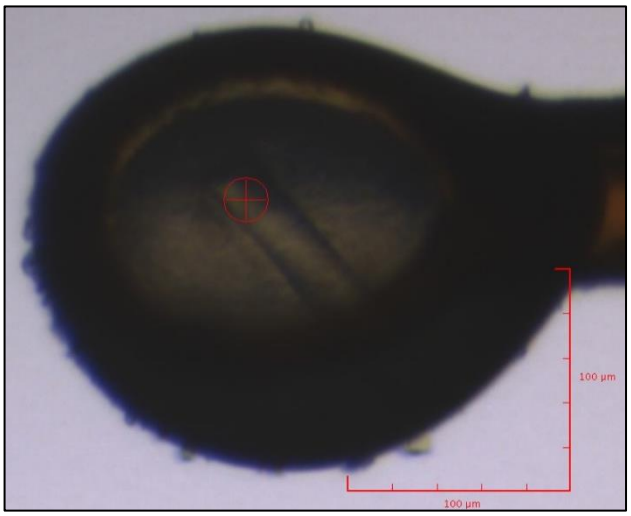

Figure 4.11. ZnT8cR protein crystal. Oblong crystal (red cross) measured approximately 80 x 20 was yielded from 3 mg/ml ZnT8cR in 100 mM MES, pH 6.5, 50 mM caesium chloride, 30% (v/v) Jeffamine M-600. No ZnT8cR crystals diffracted, therefore it could not be confirmed that this was a protein crystal rather than salt. Screens set up with ZnT8cW did not yield any crystals.

4.4 Discussion

The purported mechanism of action of the 10 mammalian ZnTs is based on that elucidated for ZnT1 (Shusterman et al., 2014) and their bacterial homologues (Lu et al., 2009). Induced conformational changes cause alternate opening and closing of the transporter and hence Zn^{2+}/H^{+} antiport to occur (Lu et al., 2009). The amino acid ligands forming the transport site in the TMD of the transporters provides selectivity for one divalent metal ion over another (Hoch et al., 2012). The CTD of *E. coli* YiiP acts as a metal sensor, allosterically regulating the function of the transporter by linking the cytosolic free Zn^{2+} concentration and subsequent occupancy of

the CTD zinc sites with exporter function (Lu et al., 2009). There is significant sequence conservation in the TMD from bacteria to mammals, whereas the CTD is much more variable (~15% identity). For instance, the location of the zinc binding site in the TMD is conserved, but the sites in the CTD are only partially conserved. Additionally, there are several amino acid motifs distinct to subsets of the mammalian ZnTs which are functionally significant. The diabetes-risk W325R mutation in the CTD of ZnT8 affects the transport kinetics of the full length transporter when reconstituted in liposomes formed of certain lipid mixtures (Merriman et al., 2016). The two major aims of this project were, firstly, to investigate the similarities between the bacterial and mammalian CTDs, and secondly, elucidate the biochemical effects of the diabetes-risk W325R mutation in ZnT8.

Predictions of the secondary structure of the CTDs of most mammalian ZnTs suggest that the ferredoxin-like fold elucidated for *E. coli* YiiP and other bacterial CDF CTDs is largely conserved. Indeed, far-UV CD spectra confirm that both ZnT8c variants form such a mixed α/β structure, and the secondary structure is not significantly affected upon zinc binding. The ferredoxin-like fold was originally identified in iron-sulphur cluster containing proteins (Orme-Johnson, 1973), and has since been found in other metal binding proteins including copper chaperones such as yeast Atx1 (Pufahl et al., 1997). The metal binding domains of bacterial and plant zinc-transporting ATPases also form ferredoxin-like folds (Blindauer, 2015).

Dimerisation of YiiP is necessary for its function as a zinc transporter. The dimer is stabilised by the "charge-interlock", a salt bridge formed between Lys77, located in a loop between TMII and TMIII, and Asp207 located in the CTD (Fig. 1.2D; (Lu et al., 2009). These residues are conserved (or rather, the charge is conserved, with Arg replacing Lys77 and Glu replacing Asp207) in ZnT8 and the other vesicular ZnTs, but isolated CTDs lacking the TMD necessarily cannot be stabilised by this mechanism. Native-PAGE and size exclusion chromatography analyses indicate that both ZnT8c apo-proteins form stable dimers in the absence of this charge-interlock, and that the dimerisation is neither dependent on disulphide formation or presence of divalent metal ions.

Similarly, the apo-CTDs of both *T. thermophilus* CzrB and *M. gryphiswaldense* MamM elute as dimers during size exclusion chromatography, and their 3D structures show that the proteins are dimeric in the absence of zinc (Cherezov et al., 2008; Zaytuni et al., 2014). The presence of monomeric ZnT8c was only observed during purification of protein expressed using autoinduction in minimal medium (Fig. 4.9), and was not confirmed with further experiments. Why a small amount of ZnT8c protein would be monomeric under these conditions but not with IPTG induction in LB medium is not clear. However, disulphide bond formation, dityrosine bond formation and metal binding have all been ruled out as responsible for ZnT8c dimer formation. Therefore, it is possible that this monomeric ZnT8c protein is not folded correctly, and thus could not form the necessary apo-dimer contacts.

The 3D structures elucidated for the CTDs of CzrB (Cherezov et al., 2008), MamM (Zaytuni et al., 2014) and *T. maritima* $TM0876_{206\text{-}306}$ (Higuchi et al., 2009) all reveal that the apo-proteins form a V-shape dimer. The interacting residues which stabilise these CTD dimers (at the point of the 'V') are in the loop between sheet β2 and helix α2 (Fig. 4.12). Specifically, in CzrB, there are interprotomer hydrogen bonds between Glu254-Gly249 and Val253-Thr251, along with several hydrophobic contacts between this loop and the C-terminus (Cherezov et al., 2008). The corresponding loop in ZnT8 CTD contains residue 325. The identity of residue 325 affects both the formation and stability of ZnT8c dimers. Expressing arginine at position 325, which increases type 2 diabetes risk in the full-length protein, causes a significant reduction in homodimerisation affinity of apo-ZnT8 CTD relative to the W325 variant. Conversely, the thermostability of apo-ZnT8cR dimers is significantly increased relative to apo-ZnT8cW dimers. Interestingly, in the bacterial CDF CTDs and the mammalian ZnT CTDs (except ZnT4), this β2-α2 loop contains at least one negatively charged residue (Asp or Glu). The interfacial charge in YiiP CTD dimers is crucial for the function of the full-length transporter (Lu et al., 2009). Therefore, it is likely that in the ZnT8 CTD, substituting the uncharged, hydrophobic Trp with the charged, polar Arg disrupts the

charge environment of the apo-dimer interaction site, causing the observed effects on dimer formation and stability.

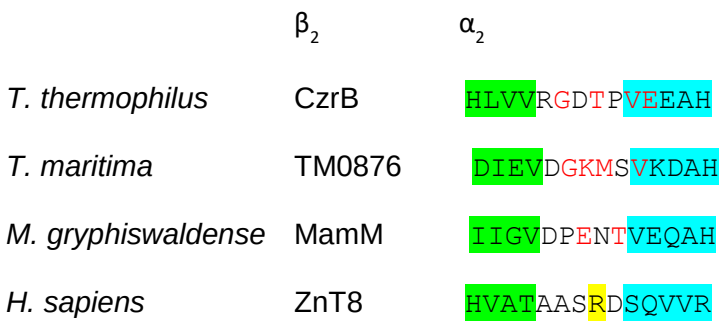

Figure 4.12. The dimer interface site elucidated for the bacterial CDF CTDs. Hydrogen bonding between residues (red text) in the loop between sheet β_2 (green) and helix α_2 (blue) stabilises the apo-dimer. Residue 325 in ZnT8 (yellow) is located in this loop.

Observed tryptophan fluorescence λ_{max} values can vary between ~310 nm for Trp48 in the protein azurin, where the Trp is totally buried in the protein interior, to ~360 nm for Trp25 in glucagon, where the Trp is totally exposed to solvent (Vivian & Callis, 2001). The λ_{max} values for W306 and W325 in ZnT8c (342 and 352 nm, respectively), indicate that both residues are partially available to solvent, although W325 more so. Residue 325 forms part of the epitope of anti-ZnT8 autoantibodies in type 1 diabetic patients (Wenzlau et al., 2008), in agreement with the high solvent accessibility of W325. However, there is no difference in risk to develop type 1 diabetes between carriers of R/W325.

Fluorescence quenching with iodide confirms that both W306 and W325 in ZnT8cW and W306 in ZnT8cR are surface-accessible to solvent. The $K_{sv}1$ values for both variants are greater than those measured for free tryptophan. This indicates that the environment of both W306 and W325 contains positive charges, as this promotes the binding of the negatively charged iodide ions. Furthermore, this charge effect on $K_{sv}1$ was decreased upon addition of 2 M NaCl. However,

a 3D model of ZnT8c with charged residues highlighted does not indicate a positively charged environment surrounding either tryptophan residue (Fig. 4.13). This suggests that, while ZnT8c forms stable dimers with the expected fold, the dimer may not be a symmetrical unit as indicated by the 3D models, and some asymmetry introduces a charged environment around the Trp residues. Studies using 'humanised' MamM, in which R/W325 were inserted into the bacterial protein, indicate that the humanised residues cause the CTD dimer to twist and introduce asymmetry (Zeytuni et al., 2014). High resolution 3D structures of the ZnT8c proteins would be required to confirm the exact dimer conformation.

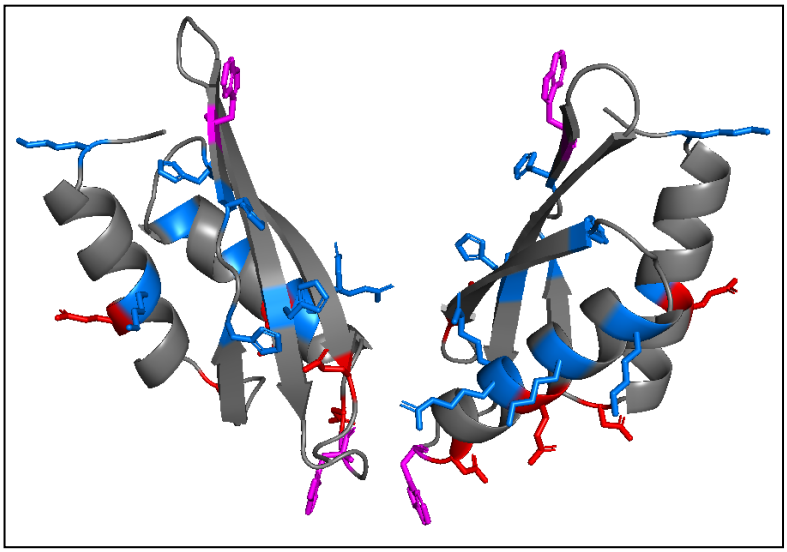

Figure 4.13. 3D homology model of ZnT8cW apo-dimer in the 'V'-shape conformation elucidated for the bacterial homologues. The two Trp residues are coloured magenta, with W306 at the top of the 'V' and W325 located at the bottom at the dimer interface. Positively charged residues (Arg, Lys, His) are coloured blue, while negatively charged residues (Glu, Asp) are coloured red. Model of ZnT8cW residues 267-369 created using SWISS-MODEL and visualised using Pymol (section 2.8).

The addition of two molar equivalents of zinc to both ZnT8c variants significantly increases the thermal stability of both proteins. The significant difference in stability between the two apo-protein variants is lost upon the addition of zinc. Residue 325 in ZnT8 is not predicted to directly

affect the conserved CTD interfacial zinc binding site. These data indicate that the structural issue caused by the R325W mutation is most prominent in the apo-protein. Unfortunately, attempts with high resolution structural techniques such as NMR and X-ray crystallography with ZnT8c did not yield 3D structures to elucidate the differences. The stabilising effect of Zn^{2+} on both ZnT8c variants is not seen upon addition of Ni^{2+}. This is important, as the proteins contain hexahistidine tags, which bind both Ni^{2+} and Zn^{2+}. This resultsuggests that metal binding to the hexahistidine tag does not significantly interfere with the structure or function of ZnT8c in these experiments.

In conclusion, both ZnT8c variants are likely to form a ferredoxin-like fold and stable apo-dimers as observed for the bacterial homologues. W325 is solvent accessible and in a charged local environment. Residue 325 is located at the predicted dimer interface site, and significantly affects both dimer formation and stability in the absence of zinc. Whether these differences cause the alterations in zinc transport and diabetes susceptibility found in full-length ZnT8 requires further experiments.

5. Metal binding of the CTD of ZnT8

Abstract

The current models of how the mammalian ZnTs function are based on the structure and function of the bacterial CDF YiiP. Metal binding to the CTD of *E. coli* YiiP causes a conformational change in the protein which allosterically regulates transport function of the full-length protein. The inter-protomer His261 residue required for this mechanism is not conserved in any mammalian ZnT. The second YiiP CTD zinc binding site is conserved in mammalian ZnTs. Potential metal binding cysteine motifs are conserved in the vesicular ZnTs CTDs. This chapter shows that the two ZnT8c variants bind zinc with a stoichiometry and affinity that differs to the bacterial homologues, emphasising the limitation of applying the bacterial model to mammals.

5.1 Introduction

Zinc binding to CDF CTDs causes conformational changes that allosterically regulate transport in the full length protein (Lu et al., 2009). Homology models predict that His261, thought to be critical for this conformational change, is not conserved in the mammalian ZnTs. The vesicular subfamily of mammalian ZnTs also contains a CXXC motif in the C-terminal tail (Fig. 1.9). This motif is found in copper chaperones and mediates the transfer of copper from chaperone to transporter (Rosenzweig & O'Halloran, 2000). Therefore, an important question became whether this motif binds zinc in ZnT8. ZnT8 also contains a third cysteine residue close to the site of this conserved motif (CXXCXXXC). The first aim of this chapter is to compare the *in vitro* zinc binding of ZnT8c with that elucidated for the bacterial homologues. The only cysteine residues in ZnT8c are in the unstructured C-terminal tail. Therefore, blocking the cysteines should not disrupt the protein structure. Alkylating agents were therefore used to investigate the stoichiometry and affinity of ZnT8c zinc binding with and without accessible cysteines.

The W325R mutation in the CTD of ZnT8 increases the risk of developing both type 2 and gestational diabetes (Davidson et al., 2014; Ziqi Lin et al., 2018). Studies on the effect of the mutation on transport function have provided mixed (contradictory) results. Transport assays conducted in rodent insulinoma cells lines MIN6 and INS-1E showed that the R325 variant had reduced transport activity (Kim et al., 2011; Nicolson et al., 2009). However, assays using proteoliposomes indicated that the R325 variant has increased transport activity under certain lipid conditions (Merriman et al., 2016). Transport assays conducted with *X. laevis* oocytes did not detect a difference between the two ZnT8 variants (Carvalho et al., 2017). Data from the previous chapter indicate that the R/W325 ZnT8c variants have altered dimer formation and stability. The second aim of this chapter, therefore, is to reveal possible differences in zinc binding capacity and affinity between the two ZnT8c variants.

5.2 Methods

5.2.1 Inductively coupled plasma mass spectrometry (ICP-MS)

Apo-protein samples were diluted using ≥18.2 MΩ.cm water and the zinc and nickel content measured with ICP-MS (Perkin Elmer Life Science, model NexION 350D). Zinc-66 and nickel-60 were measured to avoid polyatomic interferences. Raw data were automatically corrected for natural isotope abundancies by the instrument software. All sample sets contained several internal standards. Operation of the instrument was carried out by Mr. Andrew Cakebread (King's College London, UK).

To examine zinc-binding stoichiometries of the two ZnT8c variants, the proteins were diluted to 10 µM in 10 mM Tris/HCl, pH 8, 60 mM NaCl, 20 mM sucrose and incubated with 0-10 molar equivalents of Zn^{2+} ($ZnCl_2$) for 10 min at 21 °C. Unbound Zn^{2+} was removed using gravity-flow gel filtration with PD MiniTrap G-25 desalting columns (GE Healthcare). Samples were then diluted with ≥18.2 MΩ.cm water and the zinc and nickel content measured with ICP-MS.

5.2.2 UV absorbance spectroscopy

UV absorbance spectra were acquired using a Chirascan Plus spectrometer (Applied Photophysics). Protein samples of either ZnT8c variant were diluted to 35 µM in 10 mM HEPES, pH 8, 60 mM NaCl, 20 mM sucrose and incubated with 0-2 molar equivalents of Zn^{2+} for 20 min at 21 °C. Absorbance spectra were collected between 250-400 nm.

5.2.3 Tryptophan fluorescence zinc titrations

Protein samples were diluted to 2 µM in 10 mM HEPES, pH 8, 60 mM NaCl, 20 mM sucrose. Fluorescence measurements were taken as described in section 4.2.3. Stock solutions of $ZnCl_2$ were prepared in water and used for titrations up to three molar equivalents (per monomer). Spectra were corrected for Raman scattering and dilution.

5.2.4 Zincon competition assay

The affinity of the protein zinc binding sites was estimated by competition with the chromophoric dye Zincon. Zincon forms a 1:1 complex with Zn^{2+} with an affinity of 214 nM at pH 8 (Kocyła et al., 2017). The concentration of free Zincon was measured at 488 nm with a Jenway 7315 spectrophotometer using the extinction coefficient ε_{488} = 26,900 M^{-1} cm^{-1} and a 0.5 cm path length quartz cuvette. Assays were conducted in 50 mM HEPES, pH 8, 300 mM NaCl, 100 mM sucrose. Zincon was diluted to 70 µM and titrated with $ZnCl_2$, measuring the increase in absorbance at 620 nm. Competition assays were set up between 70 µM Zincon and 5 µM ZnT8c protein. Both unmodified apo-proteins and proteins treated with iodoacetamide were used (section 2.6). Binding stoichiometries were analysed by extrapolation of the linear portion of the titration curve and comparing with the buffer-only control.

5.2.5 C-terminal peptide synthesis

The human ZnT8 C-terminal peptide PDCLFCEDPCD (residues 359-369) was synthesised using a Prelude peptide synthesiser (Protein Technologies, Tucson, AZ, USA), according to the Fmoc strategy (Stawikowski & Fields, 2012). The peptide was analysed with HPLC on a Breeze system (Waters Corporation, Milford, MA, USA) equipped with an ACE5 C18-300 column (5 µm particle size, 4.6 × 250 mm), and subsequently purified with a Vydac semi-preparative column (5 mm particle size, 10 × 250 mm). The HPLC mobile phase was (A) 0.1% (v/v) trifluoroacetic acid (TFA) in water and (B) 0.1% (v/v) TFA in 90% (v/v) acetonitrile in water. The pure peptide was lyophilised and analysed on a Q-ToF Premier mass spectrometer (Waters Corporation). Peptide synthesis and purification was carried out by collaborators at the Polish Academy of Sciences (Poland; principal investigator Prof. Wojciech Bal).

5.2.6 Potentiometry

Potentiometric titrations were performed on a 907 Titrando Automatic Titrator (Metrohm, Herisau, Switzerland) with a Biotrode combined glass electrode (Metrohm). The electrode was calibrated daily by titrating an argon-bubbled 4 mM HNO_3/96 mM KNO_3 solution with 0.1 M NaOH. The solubility of the peptide in the HNO_3/KNO_3 solution was verified using UV/Vis spectroscopy. Pure peptide, stored anaerobically, was dissolved in 7.5 mL of 0.4 mM HNO_3/99.6 mM KNO_3 solution to a final concentration of 180 µM and incubated with 0-0.9 molar equivalents of $ZnCl_2$ at 25 °C for 5 min before potentiometric titrations with 0.1 M NaOH. All experiments were carried out under argon at 25 °C. The SUPERQUAD and HYPERQUAD programs (Gans et al., 1996) were used to analyse the data and generate the species distribution diagrams. The formation of complexes was characterised by the general equilibrium process:

$$p\mathrm{M} + q\mathrm{H} + r\mathrm{L} \xrightarrow{\beta \mathrm{M}p\mathrm{H}q\mathrm{L}r} \mathrm{M}p\mathrm{H}q\mathrm{L}r$$

$$\beta \mathrm{M}p\mathrm{H}q\mathrm{L}r = \frac{[\mathrm{M}p\mathrm{H}q\mathrm{L}r]}{[\mathrm{M}]p[\mathrm{H}]q[\mathrm{L}]r}$$

where M represents metal, L represents deprotonated ligand, H represents protons and β is the stability constant of a complex. In these experiments, the metal is zinc(II) and the ligand is the 11-residue ZnT8 C-terminal peptide.

5.3 Results

5.3.1 Zinc:protein stoichiometry

The two 6xHis-tagged ZnT8c protein variants were diluted to 10 µM and incubated with 0-10 molar equivalents of Zn^{2+} (section 5.2.1). Following gel filtration to remove excess Zn^{2+}, the zinc and nickel content of the proteins was measured using ICP-MS (Tables 5.1 and 5.2). Following gel filtration, the protein concentration of both variants dropped to 2 µM (measured spectroscopically). The two apo-ZnT8c variants, with no additional Zn^{2+} added, contained

approximately 0.15 total divalent metal ions (Zn^{2+} and Ni^{2+}) per monomer (n = 3; total metal content in Tables 5.1 and 5.2 divided by 2 µM protein). Over 90% of this residually bound metal was contributed by Ni^{2+}. Therefore, references to 'apo-protein' throughout this thesis refer to ZnT8c protein containing 0.15 molar equivalents of zinc and nickel ions, of which the majority is nickel. ICP-MS analysis following supplementation with up to ten molar equivalents of Zn^{2+} indicated that both 6xHis-tagged ZnT8c proteins maximally bound approximately three Zn^{2+} ions per monomer; ZnT8cR bound 2.6 ± 0.4, whereas ZnT8cW bound 3.2 ± 0.5 (Fig. 5.1). This difference in Zn^{2+} stoichiometry between the two ZnT8c variants is not statistically significant (n = 3, p = 0.156). The ICP-MS measurements indicate that the residually bound Ni^{2+} was displaced upon addition of Zn^{2+} (Tables 5.1 and 5.2). The 10 mM Tris/HCl, pH 8, 60 mM NaCl, 20 mM sucrose reaction buffer contained 0.11 ±0.01 µM nickel and 3.6 ±1.1 nM zinc (n = 3).

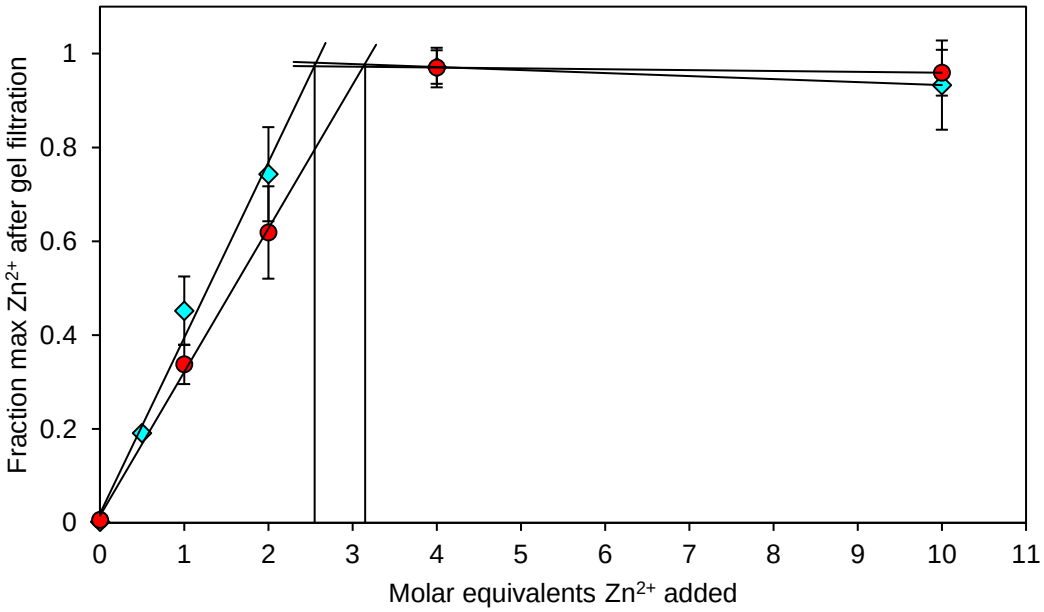

Figure 5.1. Zinc stoichiometry of the two human ZnT8c variants. Samples of 10 µM ZnT8cR (teal diamonds) or ZnT8cW (red circles) were incubated with 0-10 molar equivalents of $ZnCl_2$, unbound zinc removed using gel filtration, and their Zn^{2+} content measured using ICP-MS. The titration breakpoints indicated that ZnT8cR bound Zn^{2+} with a stoichiometry of 2.6 ± 0.4 per monomer, whereas ZnT8cW bound 3.2 ± 0.5 per monomer. This difference is not statistically significant (n = 3 for both variants, p = 0.156).

Table 5.1 ICP-MS measurements of zinc and nickel content of 2 µM monomeric ZnT8cR after gel filtration following incubation with 0-10 molar equivalents of Zn^{2+} (n = 3).

	ZnT8cR			
Mol. Equiv. Zn^{2+} added	Zn (µM)	Ni (µM)	Total metal (µM)	Metal:monomer
0	0.03 ±0.02	0.26 ±0.03	0.29	0.15
1	2.80 ±0.07	0.28 ±0.01	3.03	1.52
2	5.28 ±0.39	0.24 ±0.02	5.52	2.76
4	6.65 ±0.09	0.12 ±0.01	6.77	3.39
10	5.99 ±0.30	0.01 ±0.01	6.00	3.00

Table 5.2 ICP-MS measurements of zinc and nickel content of 2 µM monomeric ZnT8cW after gel filtration following incubation with 0-10 molar equivalents of Zn^{2+} (n = 3).

	ZnT8cW			
Mol. Equiv. Zn^{2+} added	Zn (µM)	Ni (µM)	Total metal (µM)	Metal:monomer
0	0.04 ±0.02	0.33 ±0.01	0.37	0.19
1	2.48 ±0.15	0.28 ±0.02	2.76	1.38
2	5.06 ±0.21	0.24 ±0.02	5.30	2.65
4	6.51 ±0.38	0.12 ±0.01	6.63	3.32
10	6.23 ±0.25	0.08 ±0.01	6.31	3.16

5.3.2 UV absorbance

The UV absorbance of 35 µM apo-ZnT8cR or apo-ZnT8cW was measured following addition of up to two molar equivalents (per monomer) of Zn^{2+}. The spectra of both apo-proteins contained a broad peak at approximately 320 nm, in addition to the typical peaks contributed by aromatic residues at 275-290 nm (Fig. 5.2). The signal at 320 nm was likely contributed by a metal-to-ligand charge transfer by bound Ni^{2+} (personal communication with Dr. Alex Drake, King's College London). Addition of up to two molar equivalents of Ni^{2+} to the apo-proteins did not affect the peak at 320 nm (Appendix XV). Upon addition of $ZnCl_2$, the peak at 320 nm was lost (Fig. 5.2), indicating that the Ni^{2+} was displaced by the spectroscopically silent Zn^{2+}.

A

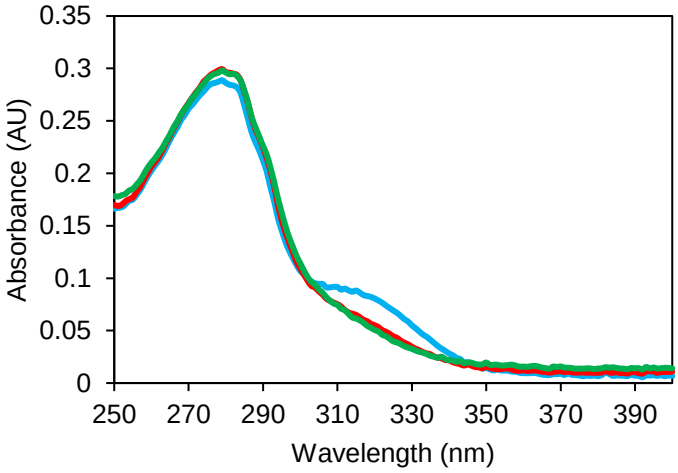

B

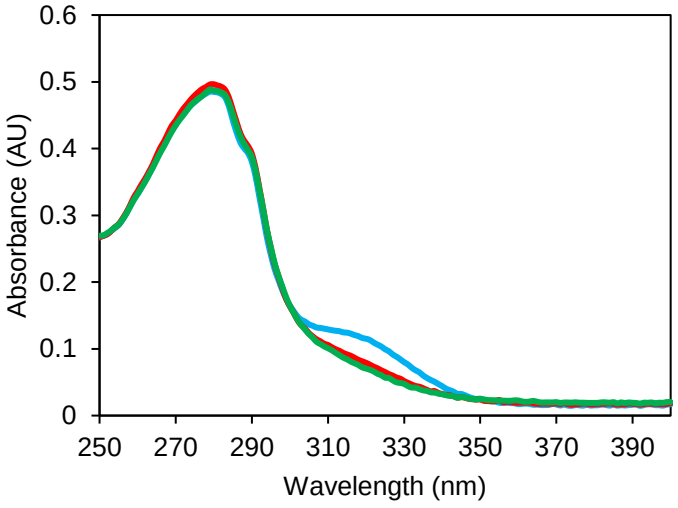

Figure 5.2. ZnT8c UV absorbance changes with addition of zinc. Representative (n = 3) UV absorbance spectra of 35 µM of, *A*, ZnT8cR and, *B*, ZnT8cW in the absence of Zn^{2+} (blue), and with one (red) and two (green) molar equivalents of Zn^{2+}, revealed that addition of Zn^{2+} ablates a broad peak at approximately 320 nm from both apo-ZnT8c variants. Spectra are buffer and dilution corrected.

5.3.3 Near-UV CD

Samples of both ZnT8c variants were diluted to 35 µM and incubated with 0-2 molar equivalents of Zn^{2+} (per monomer). Comparisons of the near-UV CD signal of the apo-, 1Zn-, and 2Zn-bound ZnT8c proteins revealed that the first and second molar equivalents of Zn^{2+} have different effects (Fig. 5.3A and B). For both ZnT8c variants, the addition of one molar equivalent of Zn^{2+} induced a negative CD peak at approximately 315 nm (Fig. 5.3C). The near-UV CD signal at this wavelength is not contributed by the aromatic residues. This is the same wavelength at which the displacement of residually bound Ni^{2+} with Zn^{2+} was observed in UV absorbance measurements (Fig. 5.2). The second molar equivalent of Zn^{2+} differentially altered the spectra of the two ZnT8c variants between 270-290 nm (Fig. 5.3D). Tryptophan contributes to near-UV CD signal between 280-295 nm. ZnT8cW contains two tryptophan residues; W325 and W306, whereas ZnT8cR contains one; W306. Therefore, the near-UV CD data indicated that binding of the second Zn^{2+} ion altered the spectral properties of W325 differently to W306, likely by binding to nearby residues.

A

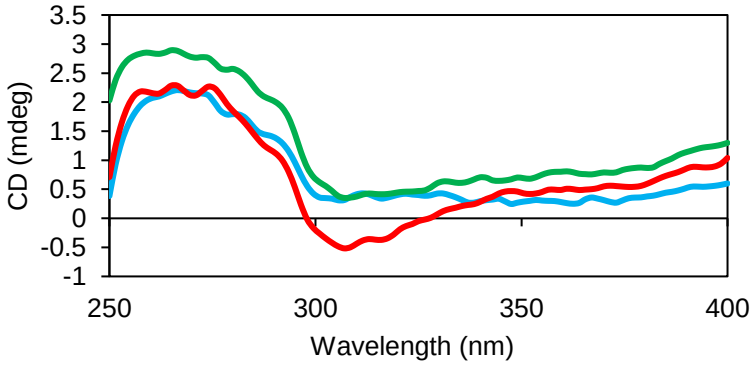

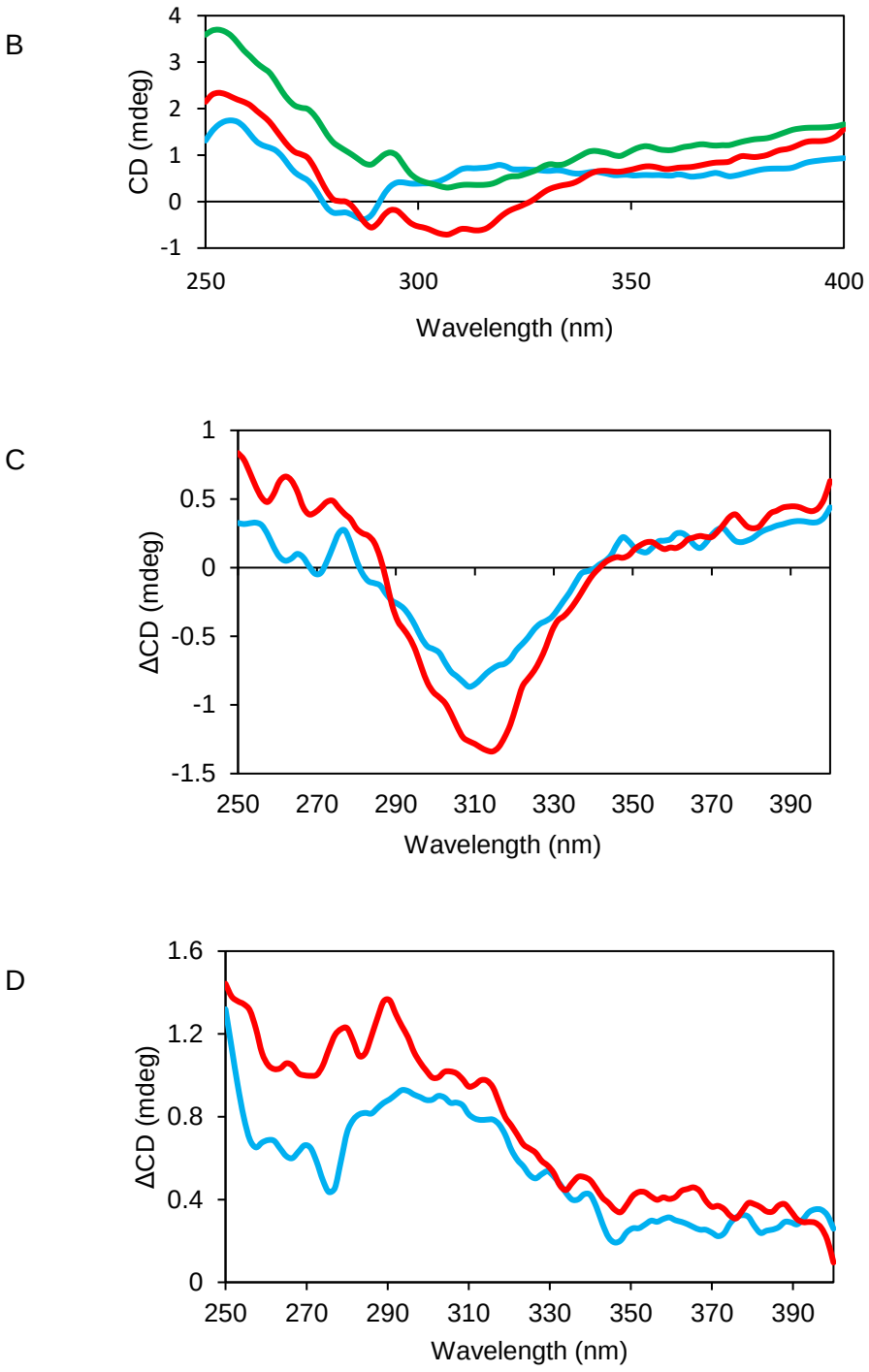

Figure 5.3. The near-UV CD of ZnT8c changes upon addition of zinc. Representative (n = 3) near-UV CD spectra with 35 µM of, A, ZnT8cR and, B, ZnT8cW in the absence of Zn^{2+} (blue), and upon addition of one (red) and two (green) molar equivalents of Zn^{2+}. Subtracting the spectrum of the apo-protein from that of the variant incubated with one molar equivalent of Zn^{2+}, C, reveals the first Zn^{2+} binding event elicits a negative peak at 310 nm for both ZnT8cR (red) and ZnT8cW (blue). *D*, subtracting the spectrum of protein incubated with one molar equivalent of Zn^{2+} from

the one of protein incubated with two molar equivalents reveals a difference in signal in the second Zn^{2+} binding event between ZnT8cR (red) and ZnT8cW (blue) between 265-290 nm.

5.3.4 Trp fluorescence zinc titrations

The effect of Zn^{2+} on the local Trp environment of both ZnT8c variants was investigated using intrinsic protein fluorescence. The wavelength at which intensity is maximal, λ_{max}, decreased by 1 nm for both ZnT8c variants upon addition of 3 molar equivalents of Zn^{2+} (per monomer, Fig. 5.4). Since the slit-width of the fluorimeter is 2.5 nm, these differences in λ_{max} are not significant. For comparison, the blue-shift elicited upon addition of 2 molar equivalents of Zn^{2+} to the bacterial homologue CTD MamM is 6-7 nm (Zaytuni et al., 2014). This suggests that the 1 nm blue-shift in λ_{max} found for both ZnT8c variants upon zinc binding does not represent the conformational change elucidated for MamM. Titration of up to 3 molar equivalents of Zn^{2+} increased the fluorescence intensity of ZnT8cR, while that of ZnT8cW was decreased (Fig. 5.4). The significance of this difference is not clear.

A

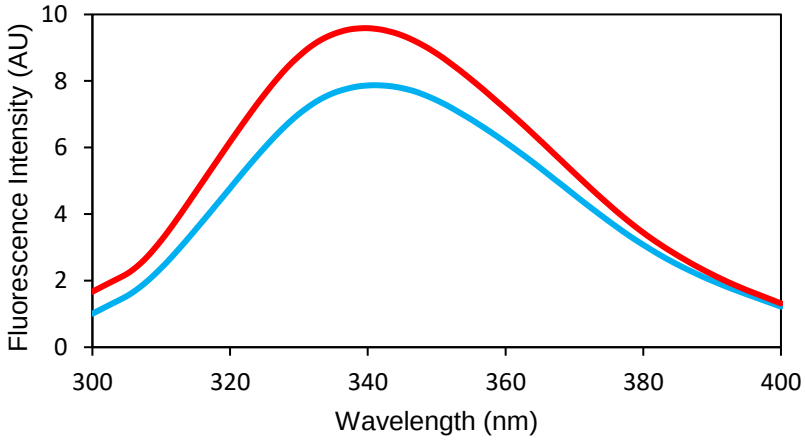

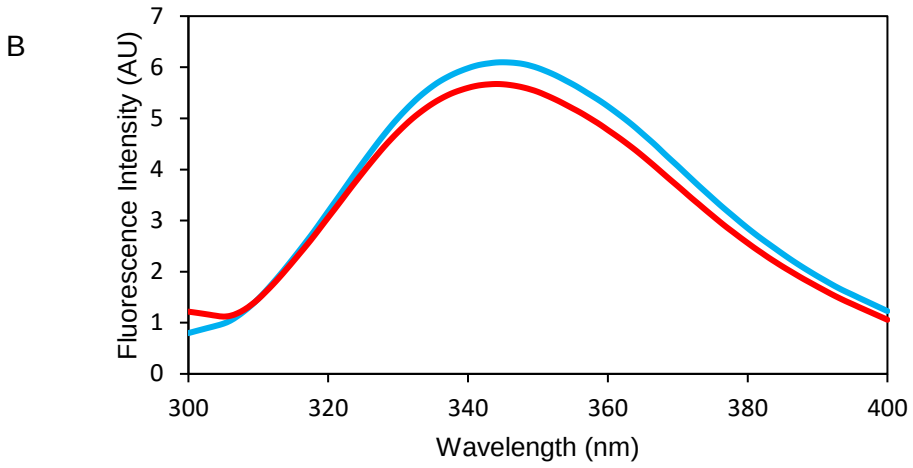

Figure 5.4. Zinc-induced changes in the tryptophan fluorescence of the two ZnT8c variants. Samples of either ZnT8c variant were diluted to 2 µM in 10 mM HEPES, pH 8, 60 mM NaCl, 20 mM sucrose and titrated with up to 3 molar equivalents of Zn^{2+}. Spectra of the apo-proteins and the proteins incubated with 3 molar equivalents of Zn^{2+} are shown for clarity. All spectra were corrected for dilution and Raman scattering. A, representative (n = 3) emission spectra (λ_{ex} = 295 nm) of ZnT8cR with no added Zn^{2+} (blue) and in the presence of 3 molar equivalents of Zn^{2+} (red). The wavelength at which intensity is maximal (λ_{max}) was 341 nm for apo-ZnT8cR and 340 nm for 3Zn-ZnT8cR. B, Fluorescence emission of ZnT8cW in the absence (blue) and presence (red) of 3 molar equivalents of Zn^{2+}. The λ_{max} was 345 nm for apo-ZnT8cW and 344 nm for 3Zn-ZnT8cW. Since the slit-width of the fluorimeter is 2.5 nm, these differences in λ_{max} are not significant.

5.3.5 Zincon competition

Zincon is a chromophoric dye which binds Zn^{2+} in a 1:1 ratio with a K_d of 214 nM at pH 8 (Kocyła et al., 2017). When titrated with Zn^{2+} in buffer (50 mM HEPES, pH 8, 300 mM NaCl, 100 mM sucrose) alone, 70 µM Zincon was saturated upon addition of 70 µM $ZnCl_2$, indicating that the buffer did not compete directly with Zincon for the added Zn^{2+} (i.e. Zincon and the buffer did not have a similar K_d for Zn^{2+}, Fig. 5.5, black squares). The signal at 620 nm increased upon addition of 1 µM $ZnCl_2$ to the 70 µM Zincon solution, indicating that the buffer did not outcompete Zincon for the added Zn^{2+} (i.e. the buffer did not have a tighter K_d for Zn^{2+} than Zincon, Fig. 5.5, black squares). However, in competition with 5 µM of either apo-ZnT8c variant, the initial increase in signal at 620 nm was not observed until 10 µM Zn^{2+} was added (Fig. 5.5, orange and blue

diamonds), indicating that both ZnT8c variants contain two zinc-binding sites with K_d < 214 nM, which outcompeted the Zincon for the added Zn^{2+}.

Alkylation of the three cysteine residues in both ZnT8c variants with iodoacetamide was confirmed using a DTNB assay (section 2.5 and 2.6). For both alkylated ZnT8c variants, only 5 µM $ZnCl_2$ was required to elicit the initial increase in Zincon signal (Fig. 5.5, red and magenta triangles), indicating that one of the two high affinity zinc-binding sites in ZnT8c is contributed by the cysteine residues.

A

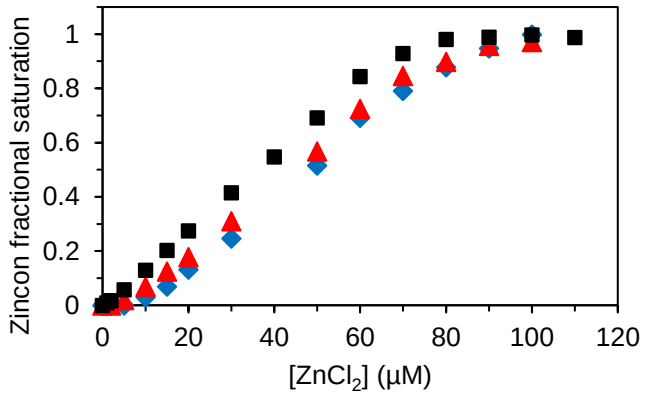

B

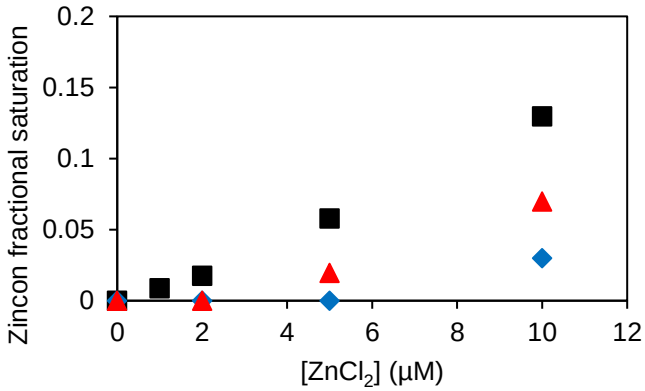

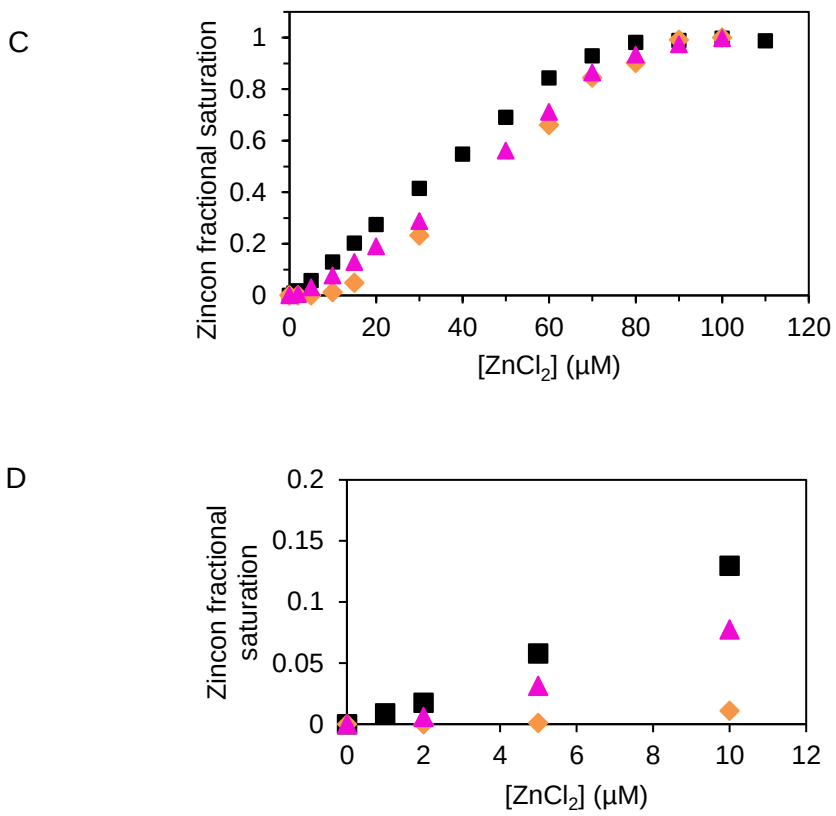

Figure 5.5. Zincon competition assay with the two ZnT8c variants. A, samples of 70 µM Zincon in 50 mM HEPES, pH 8, 300 mM NaCl, 100 mM sucrose (black squares) were saturated with 70 µM $ZnCl_2$. In competition with 5 µM ZnT8cR (blue diamonds), the initial increase in signal did not occur until 10 µM $ZnCl_2$ is added. . When the cysteine residues of ZnT8cR were alkylated with iodoacetamide (red triangles), the initial increase in signal was elicited by 5 µM $ZnCl_2$. B, Inset highlighting the initial signal increase in A. C, Titrations of Zincon in buffer (black squares), and in competition with 5 µM ZnT8cW (magenta triangles) or 5 µM alkylated ZnT8cW revealed that ZnT8cW showed similar results to ZnT8cR. D, Inset highlighting the initial signal increase in C.

5.3.6 Potentiometry

The 11-residue C-terminal peptide (denoted 'L' for ligand in Fig. 5.6 and Tables 5.3 and 5.4) of human ZnT8 was synthesised and its mass verified using mass spectrometry (not shown); sequence NH_2-PDCLFCEDPCD-COOH. Visible spectroscopy measurements indicated that concentrations of peptide greater than 0.2 mM were insoluble in the HNO_3/KNO_3 reaction solution (section 5.2.7). Therefore, 180 µM peptide was prepared in 7.5 mL of 0.4 mM

HNO_3/99.6 mM KNO_3 solution. Titration of the peptide with 0.1 M NaOH, and subsequent modelling of the proton concentration data using the SUPERQUAD and HYPERQUAD software (Gans et al., 1996), indicated that at pH 7.4 the major protonated species of the apo-peptide is LH4 (Table 5.3; Fig. 5.6A). The logK value for each L*p*H*q* in table 5.3 is calculated as the difference between the logβ values of two species. For instance, the logK of LH3 (9.71) is the logβ of LH3 (31.14) minus the logβ of LH2 (21.43). Comparing the modelled logK protonation constants to an example physiological pH of 7.4, the first four protonation actions (LH-LH4) occur at a pH higher than 7.4. Using amino acid pK_a values, this means that the three cysteine residue thiols (pK_a = 8.3) and the N-terminal proline residue α-amino group (pK_a = 10.6) are protonated at pH 7.4. Separate peptide samples were incubated with 0.5, 0.65, 0.8 and 0.9 molar equivalents of Zn^{2+}, and titrated with 0.1 M NaOH as for the apo-peptide. Modelling of these data yielded stability constants of the peptide-Zn^{2+} complex (Table 5.4). Again, the logK values are calculated as the difference between the modelled logβ values, for example the logK of ZnLH2 (7.26) is the logβ of ZnLH2 (33.14) minus the logβ of ZnLH (25.88). The stability constant of the ZnL2 complex is calculated relative to the ZnL complex, so the logK of ZnL2 (7.35) is the logβ of ZnL2 (23.33) minus the logβ of ZnL (15.98).The stability constant of the first peptide ligand (Table 5.4, ZnL, log*K* 15.98) is much higher than the second ligand (Table 5.4, ZnL2, log*K* 7.35), therefore the first peptide ligand binds to Zn^{2+} much more strongly than the second peptide ligand. Therefore, ZnL2 species do not form to a significant degree and can be ignored during modelling of the physiological speciation. The zinc-ligand species distribution diagram (modelled using SUPERQUAD and HYPERQUAD software) indicates that at pH 7.4 there is a mix of 58% ZnLH and 42% ZnLH2 (Fig. 5.6B). The stability constants for ZnLH and ZnLH2 were 9.9 and 7.3 respectively (Table 5.4). The K_a of the C-terminal peptide for Zn^{2+} can therefore be calculated by combining 58% of 9.9 and 42% of 7.3, equal to approximately 8.8, and taking the antilog (10^8.8). Therefore, the estimated K_d of the C-terminal 11-residue peptide of ZnT8 for Zn^{2+} at pH 7.4 was 2 nM.

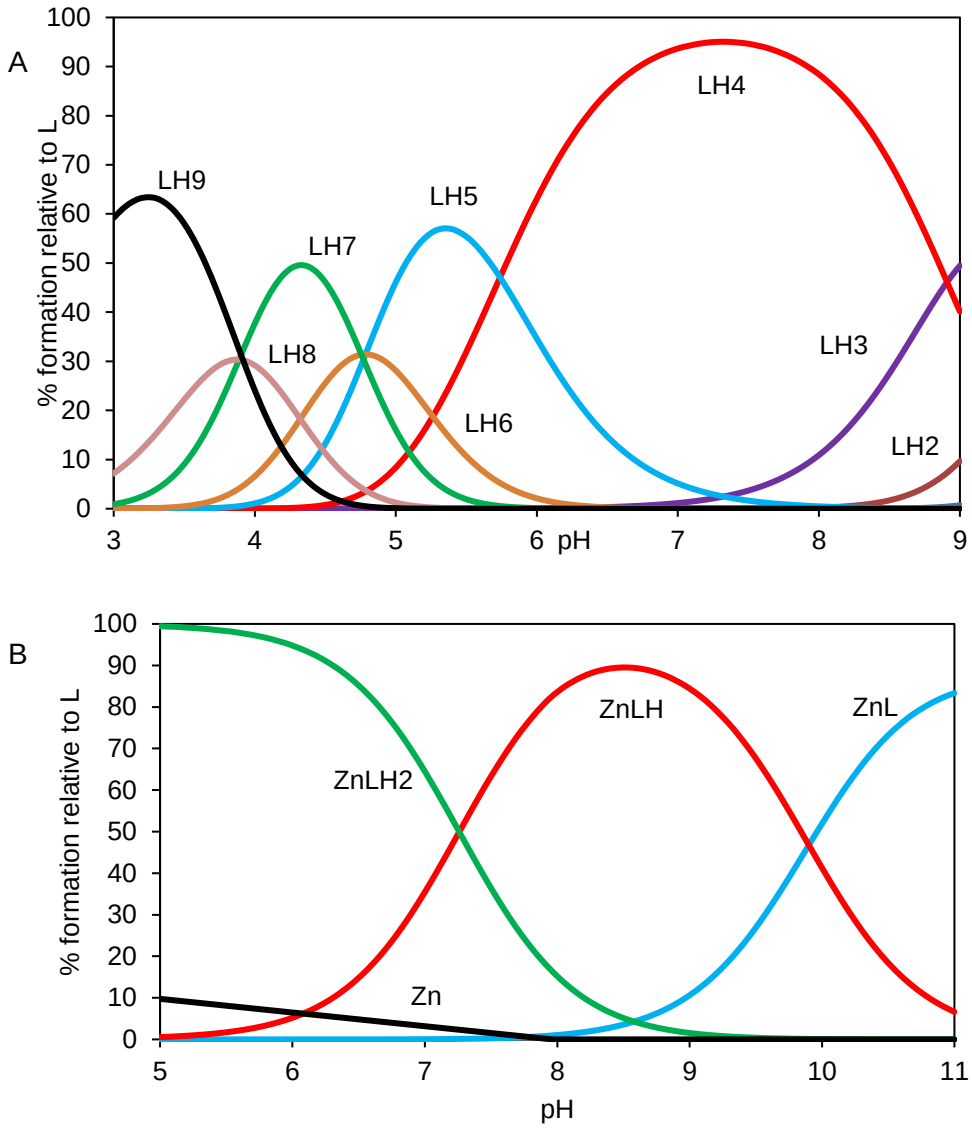

Figure 5.6. Speciation diagrams for the 11-residue ZnT8 C-terminal peptide. *A*, protonation of 180 µM peptide (denoted L) during titration with NaOH according to data in table 5.3. At pH 7.4 the dominant species is LH4 (red). *B*, modelling of 180 µM peptide with 200 µM Zn^{2+} using the stability constants in table 5.4 reveals that at pH 7.4 there is a mix of 58% ZnLH (red) and 42% ZnLH2 (green) relative to the peptide concentration. In both experiments the ionic strength is 0.1 M and the temperature is 25 ºC.

Table 5.3. Protonation constants for the ZnT8 11-residue C-terminal peptide, ionic strength 0.1 M, temperature 25 °C. The residues predicted to be protonated in each species are predicted based on amino acid pK_a values.

L*q*H*r*	logβ	log*K*	Predicted protonated residue
LH	11.29	11.29	Proline α-amino
LH2	21.43	10.14	Cysteine sulfhydryl
LH3	31.14	9.71	Cysteine sulfhydryl
LH4	40.05	8.91	Cysteine sulfhydryl
LH5	45.79	5.74	Glutamic acid side chain
LH6	50.57	4.78	Aspartic acid side chain
LH7	55.33	4.76	Aspartic acid side chain
LH8	59.22	3.89	Aspartic acid side chain
LH9	63.14	3.92	Aspartic acid α-COOH

Table 5.4. Stability constants for zinc(II)-peptide complexes, ionic strength 0.1 M, temperature 25 °C.

Zn*p*L*q*H*r*	logβ	log*K*
ZnL	15.98	15.98
ZnLH	25.88	9.9
ZnLH2	33.14	7.26
ZnL2	23.33	7.35
ZnL2H	33.85	10.52
ZnL2H2	44.20	10.35
ZnL2H3	53.43	9.23
ZnL2H4	63.01	9.58

5.4 Discussion

The CTD of the bacterial CDFs purportedly acts as a metal sensor, linking occupancy of the binuclear zinc binding site C with activation of the exporter (Lu et al., 2009). A critical aspect of this model is that one of the two zinc sites in bacterial CDFs is formed of amino acid ligands from both CTD protomers in the dimer, providing the means for the conformational change elicited upon zinc binding (Lu et al., 2009). This inter-protomer zinc site is not conserved in the mammalian ZnTs, indicating that the bacterial model may not be sufficient to describe the mechanism of action of the mammalian proteins. The diabetes-risk W325R mutation in the CTD of ZnT8 alters zinc transport when the full length protein is reconstituted in liposomes (Merriman et al., 2016). The aim of the investigations described in this chapter was to characterise the zinc binding properties of the two variant CTDs of ZnT8.

Homology modelling predicts that ZnT8c contains one zinc binding site, formed of His301, His 318, and Glu352, with a water molecule completing the tetrahedral coordination. ICP-MS measurements indicate that both ZnT8c variants contain three zinc binding sites. Two of the three binding sites have high affinity for Zn^{2+} (tighter than 214 nM), and one of the three has lower affinity. Blocking of the cysteine residues with iodoacetamide indicates that one of the ZnT8c high affinity zinc sites is provided by the C-terminal cysteine residues. Furthermore, a synthesised C-terminal peptide encompassing the ZnT8c cysteine residues binds Zn^{2+} in a 1:1 ratio with a K_d of 2 nM at pH 7.4. The low affinity site identified in both ZnT8c variants is likely provided by the hexahistidine tag. Literature values for the affinity of protein-bound His-tags for Ni^{2+} are approximately 700 nM (Nieba et al., 1997), and the affinity of His-tags for Zn^{2+} is lower than that for Ni^{2+} (Watly et al., 2015). Therefore, the stoichiometric data can be reconciled with the homology modelling in that one zinc is bound with high affinity at the conserved interfacial site, the second high affinity site is provided by the C-terminal cysteines, and the third binding site has lower affinity for Zn^{2+} and is provided by the His tag.

The affinities of the metal binding sites in CDF CTDs are critical to their purported function as sensing and regulatory units. The K_d for Zn^{2+} of the CTD of *E. coli* YiiP reconstituted into liposomes is 24 µM (Lu et al., 2009), although earlier measurements indicate one binding site in YiiP has a K_d for Zn^{2+} of 3 µM (Wei & Fu, 2006). The zinc transport K_m of YiiP in liposomes is 554 µM (Lu et al., 2009). The problem with these affinities is that the cytosolic free zinc concentration in *E. coli* is approximately nanomolar, if there is any at all (Outten & O'Halloran, 2001). Therefore, the sensing mechanism suggested for the CTD of bacterial CDFs would not detect any zinc under normal circumstances, and thus YiiP transport function would be inhibited (Lu et al., 2009). This may not be a problem for bacterial exporters such as YiiP, but the vesicular subfamily of mammalian ZnTs supply functionally significant secretory vesicles with zinc against a large concentration gradient. The two high affinity zinc binding sites (K_d < 214 nM) in the CTD of ZnT8 identified in this study are significantly stronger than the binding of the bacterial CDF CTDs.

Cytosolic free Zn^{2+} concentrations in HEK293 and HeLa cells are approximately 0.9 nM (Hessels et al., 2015). The 2 nM affinity of the C-terminal peptide indicates that the ZnT8 CTD may be able to bind physiologically relevant concentrations of zinc. However, *in vitro* binding affinities of a small peptide may not be representative of *in vitro* binding of the full-length protein, let alone *in vivo* binding. Calorimetric analysis of Zn^{2+} binding to the MTCAAC motif in the metal binding domain of *A. thaliana* Cu(I)-ATPase HMA7 reveals a similar K_d at pH 7.3 of 5 nM (Zimmermann et al., 2009). However, in the MTCAAC site in HMA7, the other coordinating ligands are provided by the amino N and the carbonyl O of the N-terminal methionine from the second protomer in a dimer (Zimmermann et al., 2009). The C-terminal peptides of the vesicular ZnTs also contain several residues which could complete the coordination geometry of a Zn^{2+} ion in a 1:1 interaction. However, which residues coordinate the Zn^{2+} ion in the peptide investigated here, and whether this is physiologically relevant, is not clear.

The relatively low stability constant of the ZnL2 ZnT8 C-terminal peptide species indicates that zinc-induced dimerisation of the peptide is not energetically favoured. This agrees with native PAGE data in Chapter 4 of this thesis showing that dimerisation of ZnT8c is independent of disulphide formation or the presence of divalent cations (Fig. 4.3). While ZnT8 contains three C-terminal cysteine residues, only the CXXC motif is conserved in the other vesicular ZnTs. It is tempting to speculate that the importance of metal transport into specific functional vesicles by vesicular ZnTs has resulted in the evolution of additional metal sensing/uptake strategies relative to the non-vesicular ZnTs. To discover whether this motif mediates transfer of metal from a chaperone to the transporter, as in copper homeostasis (Rosenzweig & O'Halloran, 2000), requires additional experiments. Intriguingly, the coordination of Zn^{2+} by cysteine residues means that occupancy of the site is necessarily linked to cellular redox biology. Pancreatic beta-cells are unusually vulnerable to oxidative stress (Lenzen, 2008). This is exacerbated by increased reactive oxygen species (ROS) production by mitochondria during prolonged exposure to high glucose (Gerber & Rutter, 2017), a symptom of type 2 diabetes. Increased ROS production during

hypoxia decreases both ZnT8 expression and cytosolic free zinc (Gerber et al., 2014). It is therefore conceivable that ZnT8 and the other vesicular ZnTs are regulated in some way by cellular redox balance through cytosolic zinc binding to these C-terminal cysteine residues. This study is the first evidence of the *in vitro* functionality of this motif in mammalian ZnTs. Additional experiments are required to elucidate the function *in vivo*.

In the CTDs of CzrB and MamM, addition of zinc to the apo-proteins causes the CTD protomers to swing together, from a 'V' shape to a 'II' shape. This conformational change is verified by the crystal structures of apo- and zinc-bound CzrB (Cherezov et al., 2008), and small angle X-ray scattering (SAXS) of both CzrB and MamM (Cherezov et al., 2008; Zaytuni et al., 2014). In common with ZnT8c, MamM encodes a single Trp residue located on the dimer interface in the open part of the V-conformation formed by the apo-proteins (W247 in MamM, W306 in ZnT8cR) (Zaytuni et al., 2014). Addition of Zn^{2+} to MamM causes a blue-shift in intrinsic protein fluorescence λ_{max}, indicative of W247 becoming less solvent accessible after the transition from the apo (V-shape) to Zn^{2+}-bound (II-shape) conformation (Zaytuni et al., 2014). Intrinsic protein fluorescence data presented here show that addition of two molar equivalents of Zn^{2+} do not induce a large blue-shift in ZnT8c Trp fluorescence, indicating that the conformational change observed in the bacterial CDF CTDs is not induced by Zn^{2+} in ZnT8c. This is to be expected, as the mammalian ZnTs are not predicted to contain the interprotomer ligand (His261 in *E. coli* YiiP) found in the bacterial homologues. In the absence of a zinc-induced conformational change, it is not clear what the *in vivo* function of the interfacial zinc site is in the mammalian ZnTs.

This study did not detect any significant difference in zinc binding between ZnT8cR and ZnT8cW. The near-UV CD data indicate that binding of the second Zn^{2+} ion alters the spectral properties of W325 differently to W306. This is to be expected, as W325 is predicted to be localised close to the canonical interface binding site and may be close to the cysteine site in the unstructured C-terminal tail (Fig. 5.7). Characterisation of the transport kinetics of the two full length ZnT8 isoforms revealed that the R325 variant is a more active transporter under certain lipid

compositions in liposomes (Merriman et al., 2016). The altered lipid conditions purportedly mirror those found in insulin secretory granules *in vivo* (Merriman et al., 2016). A second report investigating differential uptake into *X. laevis* oocytes did not find a difference in transport activity between the R/W325 ZnT8 variants (Carvalho et al., 2017). Therefore, there may be a difference in zinc binding to the two ZnT8c variants, but the techniques used in this study were not sufficiently sensitive to detect it. It may also be the case that exposure to certain lipid conditions *in vitro* or *in vivo* alters the function of the full-length proteins in such a way that zinc binding to the CTD is modified by residue 325.

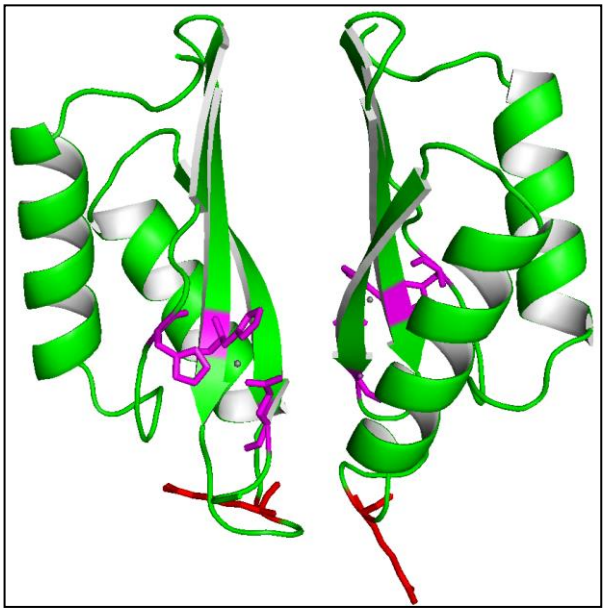

Figure 5.7. Homology model of ZnT8cR. 3D homology model of ZnT8cR produced using SWISS-MODEL (section 2.9) based on the zinc-bound structure of *T. thermophilus* CzrB (PDB ID: 3byr). The residues forming the canonical interface site are coloured magenta and residue 325 (Arg) is coloured red. The predicted location of residue 325 is both at the dimerisation site and close to the interfacial zinc binding site.

In conclusion, this study shows that zinc binding to the CTDs of mammalian ZnTs is different to that elucidated for the bacterial homologues. The identification of two high-affinity zinc binding sites in ZnT8 CTD suggests that a sensing role of this domain is possible *in vivo*. The C-terminal cysteine motif has an affinity for Zn^{2+} of 2 nM. This motif is only conserved in the vesicular ZnTs,

suggesting that there may be a specialised zinc sensing/uptake mechanism for this critical subfamily. Additional structural information would help to elucidate the functional consequences of zinc binding to this domain, and may help further unravel the effect of the diabetes-risk W325R mutation on ZnT8 function.

6. General Discussion

Zinc biochemistry is central to cellular processes in all forms of life. While iron is twice as abundant as zinc in the human body, the proportion of the human proteome contributed by zinc proteins is five times that of iron proteins (10% to 2%) (Andreini et al., 2006a, 2018). These structural and catalytic roles for zinc in proteins are complemented by the emerging field of zinc signalling (Maret, 2017). Correct cellular compartmentalisation of zinc is inextricably linked to these functions. In humans, the efflux of zinc from the cytosol into organelles or the extracellular space is mediated by the ZnT family of transporters (Palmiter & Huang, 2004).

There is currently no 3D structure of a mammalian ZnT. The models of how these transporters function are based on the mechanism elucidated for their bacterial homologues, in particular that of *E. coli* YiiP (Lu et al., 2009). YiiP protomers are formed of a TMD and a metal-binding CTD, an architecture which is generally shared by most of the mammalian ZnTs (Kambe et al., 2015). In YiiP, the CTD contains a binuclear zinc binding site, with one component ligand provided from the second protomer in the dimer (Lu & Fu, 2007). A conformational change is elicited in the YiiP CTD by zinc binding to this interprotomer site, which allosterically regulates transporter function (Lu et al., 2009). This crucial interprotomer site is not conserved in mammalian ZnTs, indicating that this 'sensing' function of the CTD may differ in mammals.

The functions of mammalian ZnTs extend beyond simple transport. ZnT1 is implicated in the Ras-ERK signalling pathway and modulates the activity and localisation of both L-type and T-type calcium channels (Levy et al., 2009; Mor et al., 2012). ZnT2 recruits the vacuolar H^+-ATPase to the membrane of secretory vesicles in mammary epithelia (Lee et al., 2017). Mutations in the CTDs of human ZnTs are linked to several diseases, including TNZD, hypermanganesemia, and diabetes (Hogstrand & Maret, 2016). The W325R mutation in the CTD of ZnT8 increases the risk of developing both type 2 and gestational diabetes, and alters the specificity of autoantibodies in type 1 diabetes (Davidson et al., 2014; Ziqi Lin et al., 2018; Wenzlau et al., 2008). Cell, oocyte

and proteoliposome-based transport assays have returned contradictory results on the effect of the W325R mutation on transport kinetics of the full-length protein (Carvalho et al., 2017; Merriman et al., 2016; Nicolson et al., 2009). Elucidating structural and functional characteristics of the two variant CTDs of ZnT8 would aid in our understanding of how this crucial family of proteins function, and could shed light on the pathogenesis of these diseases.

The first aim of this study was to express and purify the CTDs of the two common ZnT8 variants. The expression and purification of three bacterial CDF CTDs separate from the TMD has been previously reported (Hattori et al., 2007; Höfer et al., 2007; Zeytuni et al., 2012). Sequence analysis reveals that the ferredoxin-like fold formed by these domains is conserved in ZnT8c. The human copper chaperone Atox1 also forms this fold, and has been successfully expressed in *E. coli* (Belviso et al., 2016). Therefore, it was expected that ZnT8c would express in *E. coli*. Expression plasmids encoding ZnT8c were therefore designed, and Chapter 3 details the process of optimising the expression and purification of the two variant proteins. Both ZnT8c variants predominantly expressed in an insoluble form. Initial expression tests with a plasmid encoding a WELQ protease site instead of a TEV protease site resulted in solely insoluble protein being produced. Two conclusions can be drawn from the data collected with this construct. Firstly, this shows that the N-terminal extension is critical to the solubility and/or folding of the protein. We tested the soluble protein expression with several different C-terminal deletions, anticipating that aberrant disulphide formation between the cysteine residues in this region were contributing to the misfolding. Deletion of the region containing these cysteine residues did not alleviate the misfolding problem. The region selected to represent the CTD of ZnT8 (residues 267-369) was based on the information in the UniProt database. The first eight residues of this region (LKDFSILL) contains a large proportion of hydrophobic residues. Deleting one or more of these residues, or adding one or more hydrophilic residues around the protease site, may have improved the soluble protein expression.

Secondly, the refolding of isolated, denatured ZnT8c requires additional optimisation. This misfolding process may also extend to the aggregated protein produced during soluble protein expression with the TEV constructs. Using a different expression system could have greatly improved the expression and folding of ZnT8c protein. While we did not anticipate the presence of post-translational modifications, and the human protein Atox1, which is also formed of a ferredoxin fold, was successfully expressed in *E. coli* (Belviso et al., 2016), a eukaryotic system such as yeast or insects would have been simple to test and may have solved these issues.

Switching to a low induction temperature and longer induction time increased the soluble protein yield to approximately 1 mg per litre of culture for both variants. Far-UV CD analysis indicated that the dimeric proteins were folded as expected, and both variants formed dimers independently of disulphide bond formation or the presence of divalent metal ions. The soluble, aggregated ZnT8c protein was formed of a predominantly β-sheet structure, indicating some protein misfolding. Formation of amyloid-like structures by ZnT8c could be very interesting, as amyloidogenesis is implicated in type 2 diabetes (Mukherjee et al., 2015), and the full-length protein forms SDS-resistant dimers when extracted from mammalian cells (Nicolson et al., 2009). Whether this connection is physiologically relevant would require additional experiments. Further optimisation of the ZnT8c protein expression yield is almost certainly possible, and the presence of additional chaperones in eukaryotic expression systems would likely reduce protein misfolding. However, after the first 18 months of this study these efforts were halted to focus on the downstream experiments.

The second aim of this study was to elucidate the differences between ZnT8c and the CTDs of the bacterial homologues. These experiments were greatly aided by the biophysical characterisation (beyond just a 3D structure) of the bacterial CDF CTDs *T. thermophilus* CzrB and *M. gryphiswaldense* MamM, although metal binding data is scarce in these reports (Cherezov et al., 2008; Zaytuni et al., 2014). In common with these homologous proteins, ZnT8c forms a stable dimer in the absence of divalent cations. The ferredoxin-like fold is conserved. One key

difference is the loss of the protomer-bridging His261 residue in the mammalian ZnTs, which is crucial for the CTD conformational change in the sensing mechanism of YiiP (Lu et al., 2009). In the absence of this movement, what is the function of Zn^{2+} binding to the CTD of mammalian ZnTs? High resolution 3D structures of ZnT8c would answer this question. That ZnT8c protein crystals did not diffract indicates that the protein contained some internal disorder, which is probably caused by unfolding, exacerbated by the high protein concentrations required for crystal formation.

In the bacterial homologues, the affinity of the metal binding sites is approximately micromolar; too weak to bind nanomolar free Zn^{2+} in the cytosol under normal conditions (Outten & O'Halloran, 2001; Wei & Fu, 2006). This disparity spawned proposals of chaperone-mediated delivery of Zn^{2+} to the transporters (Cherezov et al., 2008), similar to that found in copper transport (Harris, 2000). An interesting property of the vesicular subfamily of ZnTs is the conservation of a cysteine motif (CXXC) in the C-terminal tail. The most abundant cytosolic zinc chaperone is cysteine-rich metallothionein, which is ubiquitously expressed in eukarya but has only been identified in some bacteria (Blindauer, 2011). However, there is no evidence so far of chaperone-mediated transfer of metal to zinc transporters. Intriguingly, the C-terminal peptide of ZnT8 containing the cysteine residues has an affinity for Zn^{2+} of 2 nM at pH 7.4. Therefore, the cytosol-facing CTD could bind physiologically relevant concentrations of free zinc (approximately 0.9 nM in HeLa and HEK293 cells (Hessels et al., 2015)). The conserved interfacial zinc-binding site also has a significantly stronger affinity for Zn^{2+} than the bacterial homologues. These strong binding sites may be involved in specific uptake mechanisms evolved in the vesicular ZnTs, which are not necessarily required in ZnTs localised to the Golgi or the plasma membrane. Regardless, there are clearly significant differences between ZnT8c and the bacterial CDF CTDs.

The third aim of this study was to assess the biochemical effect of the diabetes-risk W325R mutation in ZnT8c. In the full-length protein, this mutation has been shown to affect zinc transport in some (Merriman et al., 2016; Nicolson et al., 2009), but not all studies (Carvalho et

al., 2017). The protein conformation is also altered by the mutation, as the specificity of autoantibodies is different in type 1 diabetic patients (Wenzlau et al., 2008). This study did not detect a difference in metal binding between the two ZnT8c variants. There are two possibilities for this; firstly, the techniques used may not have been sensitive enough to detect the difference. Revealing the difference in transport kinetics between the two full-length ZnT8 variants in proteoliposomes required certain lipid formulations, suggesting that the mutation does not cause large changes in the proteins (Merriman et al., 2016). One issue with our study is that the ZnT8c protein always contained a zinc-binding His-tag. This issue prevented some additional experiments to explore small differences in metal binding between the two protein variants, such as ITC, as data analysis would be plagued by concerns of zinc binding to the tag. However, one technique that could have been used to validate the metal:protein stoichiometries and affinities is electrospray ionisation mass spectrometry (ESI-MS) (Deng et al., 2010). ESI-MS has the added benefits of accurately quantifying the protein concentration, which is an issue that was not addressed fully in this thesis, and determining the exact size of the protein isolates. This would have been particularly useful during protease cleavage optimisation.

The second possible reason that no difference in metal binding was detected between the two ZnT8c variants is that there is no difference. This study indicates that the differences caused by the W325R mutation are in dimer formation and stability. In the bacterial CTDs, the loop between β2-α2 forms the dimer interface (Cherezov et al., 2008; Higuchi et al., 2009; Zaytuni et al., 2014). The corresponding loop in ZnT8 contains residue 325. In *E. coli* YiiP, the CTD charge interface is critical to its function (Lu et al., 2009). The substitution of an uncharged, aromatic Trp side chain for a charged, polar Arg side chain disrupts the dimer interface in ZnT8c. Studies using humanised *M. gryphiswaldense* MamM, in which R/W325 is mutated in to the bacterial CTD, indicate that the dimer is twisted and becomes asymmetrical (Zeytuni et al., 2014). The CTDs of other mammalian ZnTs have been shown to mediate protein-protein interactions; of particular interest is the recruitment of a H^+-ATPase to the secretory granule membrane by ZnT2

(Lee et al., 2017). Therefore, one possibility is that the mutation at residue 325 which increases diabetes-risk may alter functions of ZnT8 unrelated to zinc transport itself.

One interesting aspect of ZnT8 biochemistry that was not explored in this thesis is that of heterodimer formation. Alleles for both isoforms vary in different populations, but are both common; 'C' encoding R325 present in 60-95% of people, 'T' encoding W325 present in 5-40% (Boesgaard et al., 2008). Therefore, in some populations most people will express both protein isoforms. Whether heterodimers can form in the full-length proteins is not known, but the isolated CTDs of both forms would be an excellent tool to begin to explore this relationship.

Future directions

This study is the first to show that the CTD of a mammalian ZnT binds Zn^{2+} and that it may be physiologically relevant. However, a key issue which remains unanswered at this stage is what the purpose of this Zn^{2+} binding actually is, both *in vitro* and *in vivo*. High resolution 3D structural elucidation using NMR spectroscopy with the ZnT8c proteins is ongoing in our laboratory, with the hope to answer the question of *in vitro* function. As suggested above, the biochemical effect of this mutation *in vivo* may be to interfere with protein-protein interactions or other protein functionality. In some populations, the heterodimer may be the most relevant form of the full-length protein. Many of the experiments presented in this thesis could simply be repeated with a mixture of both forms of ZnT8c. Investigations into other potential protein partners for ZnT8 are also ongoing in our laboratory.

VII. References

Alam, S., Hennigar, S. R., Gallagher, C., Soybel, D. I., & Kelleher, S. L. (2015). Exome Sequencing of SLC30A2 Identifies Novel Loss- and Gain-of-Function Variants Associated with Breast Cell Dysfunction. *Journal of Mammary Gland Biology and Neoplasia*, *20*(3–4), 159–172.

Andreini, C., Banci, L., Bertini, I., & Rosato, A. (2006a). Counting the Zinc-Proteins Encoded in the Human Genome. *Journal of Proteome Research*, *5*(1), 196–201.

Andreini, C., Banci, L., Bertini, I., & Rosato, A. (2006b). Zinc through the Three Domains of Life. *Journal of Proteome Research*, *5*(11), 3173–3178.

Andreini, C., Putignano, V., Rosato, A., & Banci, L. (2018). The human iron-proteome. *Metallomics*, *10*(9), 1223–1231.

Andrews, G. K., Wang, H., Dey, S. K., & Palmiter, R. (2004). Mouse zinc transporter 1 gene provides an essential function during early embryonic development. *Genesis*, *40*(2), 74–81.

Anton, A., Grosse, C., Reissmann, J., Pribyl, T., & Nies, D. H. (1999). CzcD is a heavy metal ion transporter involved in regulation of heavy metal resistance in Ralstonia sp. strain CH34. *Journal of Bacteriology*, *181*(22), 6876–6881.

Árus, D., Dancs, Á., Nagy, N. V., & Gajda, T. (2013). A comparative study on the possible zinc binding sites of the human ZnT3 zinc transporter protein. *Dalton Transactions*, *42*(33), 12031.

Assuncao, A. G. L., Herrero, E., Lin, Y.-F., Huettel, B., Talukdar, S., Smaczniak, C., Immink, R. G. H., van Eldik, M., Fiers, M., Schat, H., & Aarts, M. G. M. (2010). Arabidopsis thaliana transcription factors bZIP19 and bZIP23 regulate the adaptation to zinc deficiency. *Proceedings of the National Academy of Sciences*, *107*(22), 10296–10301.

Banci, L., Bertini, I., Ciofi-Baffoni, S., Finney, L. A., Outten, C. E., & O'Halloran, T. V. (2002). A new zinc-protein coordination site in intracellular metal trafficking: Solution structure of the Apo and Zn(II) forms of ZntA(46-118). *Journal of Molecular Biology*, *323*(5), 883–897.

Barnett, J. P., Blindauer, C. A., Kassaar, O., Khazaipoul, S., Martin, E. M., Sadler, P. J., & Stewart, A. J. (2013). Allosteric modulation of zinc speciation by fatty acids. *Biochimica et Biophysica Acta - General Subjects*, *1830*(12), 5456–5464.

Bellomo, E., Massarotti, A., Hogstrand, C., & Maret, W. (2014). Zinc ions modulate protein tyrosine phosphatase 1B activity. *Metallomics*, *6*(7), 1229–1239.

Belviso, B. D., Galliani, A., Lasorsa, A., Mirabelli, V., Caliandro, R., Arnesano, F., & Natile, G. (2016). Oxaliplatin Binding to Human Copper Chaperone Atox1 and Protein Dimerization. *Inorganic Chemistry*, *55*(13), 6563–6573.

Biasini, M., Bienert, S., Waterhouse, A., Arnold, K., Studer, G., Schmidt, T., Kiefer, F., Cassarino, T. G., Bertoni, M., Bordoli, L., & Schwede, T. (2014). SWISS-MODEL: Modelling protein tertiary and quaternary structure using evolutionary information. *Nucleic Acids Research*, *42*(W1), W252–W258.

Blaudez, D. (2003). Poplar Metal Tolerance Protein 1 Confers Zinc Tolerance and Is an Oligomeric Vacuolar Zinc Transporter with an Essential Leucine Zipper Motif. *The Plant Cell*, *15*(12), 2911–2928.

Blindauer, C. A. (2011). Bacterial metallothioneins: Past, present, and questions for the future. *Journal of Biological Inorganic Chemistry*, *16*(7), 1011–1024.

Blindauer, C. A. (2015). Advances in the molecular understanding of biological zinc transport. *Chemical Communications*, *51*(22), 4544–4563.

Boesgaard, T. W., Žilinskaitė, J., Vänttinen, M., Laakso, M., Jansson, P.-A., Hammarstedt, A., Smith, U., Stefan, N., Fritsche, A., Häring, H., Hribal, M., Sesti, G., Zobel, D. P., Pedersen, O., Hansen, T., & Consortium, for the E. 2. (2008). The common SLC30A8 Arg325Trp variant is associated with reduced first-phase insulin release in 846 non-diabetic offspring of type 2 diabetes patients—the EUGENE2 study. *Diabetologia*, *51*(5), 816–820.

Bradford, M. M. (1976). A rapid and sensitive method for the quantitation of microgram quantities of protein utilizing the principle of protein-dye binding. *Analytical*

Biochemistry, *72*(1–2), 248–254.

Brender, J. R., Hartman, K., Nanga, R. P. R., Popovych, N., de la Salud Bea, R., Vivekanandan, S., Marsh, E. N. G., & Ramamoorthy, A. (2010). Role of Zinc in Human Islet Amyloid Polypeptide Aggregation. *Journal of the American Chemical Society*, *132*(26), 8973–8983.

Brown, M. A., Thom, J. V., Orth, G. L., Cova, P., & Juarez, J. (1964). Food Poisoning Involving Zinc Contamination. *Archives of Environmental Health: An International Journal*, *8*(5), 657–660.

Burgess, R. R. (2009). Chapter 17 Refolding Solubilized Inclusion Body Proteins. In *Methods in Enzymology* (1st ed., Vol. 463, pp. 259–282). Elsevier Inc.

Carson, M., Johnson, D. H., McDonald, H., Brouillette, C., & DeLucas, L. J. (2007). His-tag impact on structure. *Acta Crystallographica Section D Biological Crystallography*, *63*(3), 295–301.

Carvalho, S., Molina-López, J., Parsons, D., Corpe, C., Maret, W., & Hogstrand, C. (2017). Differential cytolocation and functional assays of the two major human SLC30A8 (ZnT8) isoforms. *Journal of Trace Elements in Medicine and Biology*, *44*, 116–124.

Chandra, B. R., Yogavel, M., & Sharma, A. (2007). Structural Analysis of ABC-family Periplasmic Zinc Binding Protein Provides New Insights Into Mechanism of Ligand Uptake and Release. *Journal of Molecular Biology*, *367*(4), 970–982.

Cherezov, V., Höfer, N., Szebenyi, D. M. E., Kolaj, O., Wall, J. G., Gillilan, R., Srinivasan, V., Jaroniec, C. P., & Caffrey, M. (2008). Insights into the Mode of Action of a Putative Zinc Transporter CzrB in Thermus thermophilus. *Structure*, *16*(9), 1378–1388.

Chimienti, F., Devergnas, S., Favier, A., & Seve, M. (2004). Identification and cloning of a beta-cell-specific zinc transporter, ZnT-8, localized into insulin secretory granules. *Diabetes*, *53*(9), 2330–2337.

Chimienti, F., Devergnas, S., Pattou, F., Schuit, F., Garcia-Cuenca, R., Vandewalle, B., Kerr-Conte, J., Van Lommel, L., Grunwald, D., Favier, A., & Seve, M. (2006). In vivo expression and functional characterization of the zinc transporter ZnT8 in glucose-induced insulin

secretion. *Journal of Cell Science*, *119*(Pt 20), 4199–4206.

Coudray, N., Valvo, S., Hu, M., Lasala, R., Kim, C., Vink, M., Zhou, M., Provasi, D., Filizola, M., Tao, J., Fang, J., Penczek, P. A., Ubarretxena-Belandia, I., & Stokes, D. L. (2013). Inward-facing conformation of the zinc transporter YiiP revealed by cryoelectron microscopy. *Proceedings of the National Academy of Sciences*, *110*(6), 2140–2145.

da Silva Xavier, G., Bellomo, E. A., McGinty, J. A., French, P. M., & Rutter, G. A. (2013). Animal Models of GWAS-Identified Type 2 Diabetes Genes. *Journal of Diabetes Research*, 1–12.

Davidson, H. W., Wenzlau, J. M., & O'Brien, R. M. (2014). Zinc transporter 8 (ZnT8) and β cell function. *Trends in Endocrinology & Metabolism*, *25*(8), 415–424.

Deng, L., Sun, N., Kitova, E. N., & Klassen, J. S. (2010). Direct Quantification of Protein−Metal Ion Affinities by Electrospray Ionization Mass Spectrometry. *Analytical Chemistry*, *82*(6), 2170–2174.

Dodson, G., & Steiner, D. (1998). The role of assembly in insulin's biosynthesis. *Current Opinion in Structural Biology*, *8*(2), 189–194.

Dräger, D. B., Desbrosses-Fonrouge, A.-G., Krach, C., Chardonnens, A. N., Meyer, R. C., Saumitou-Laprade, P., & Krämer, U. (2004). Two genes encoding *Arabidopsis halleri* MTP1 metal transport proteins co-segregate with zinc tolerance and account for high *MTP1* transcript levels. *The Plant Journal*, *39*(3), 425–439.

Drozdetskiy, A., Cole, C., Procter, J., & Barton, G. J. (2015). JPred4: a protein secondary structure prediction server. *Nucleic Acids Research*, *43*(W1), W389–W394.

Dunn, M. F. (2005). Zinc–Ligand Interactions Modulate Assembly and Stability of the Insulin Hexamer – A Review. *BioMetals*, *18*(4), 295–303.

Eizirik, D. L., Sammeth, M., Bouckenooghe, T., Bottu, G., Sisino, G., Igoillo-Esteve, M., Ortis, F., Santin, I., Colli, M. L., Barthson, J., Bouwens, L., Hughes, L., Gregory, L., Lunter, G., Marselli, L., Marchetti, P., McCarthy, M. I., & Cnop, M. (2012). The human pancreatic islet transcriptome: Expression of candidate genes for type 1 diabetes and the impact of pro-

inflammatory cytokines. *PLoS Genetics*, *8*(3), e1002552.

Flannick, J., Thorleifsson, G., Beer, N. L., Jacobs, S. B. R., Grarup, N., Burtt, N. P., Mahajan, A., Fuchsberger, C., Atzmon, G., Benediktsson, R., … Altshuler, D. (2014). Loss-of-function mutations in SLC30A8 protect against type 2 diabetes. *Nature Genetics*, *46*(4), 357–363.

Foster, M. C., Leapman, R. D., Li, M. X., & Atwater, I. (1993). Elemental composition of secretory granules in pancreatic islets of Langerhans. *Biophysical Journal*, *64*(2), 525–532.

Franklin, R. B. (2007). Zinc and zinc transporters in normal prostate function and the pathogenesis of prostate cancer. *Frontiers in Bioscience*, *10*(1–3), 2230.

Fukue, K., Itsumura, N., Tsuji, N., Nishino, K., Nagao, M., Narita, H., & Kambe, T. (2018). Evaluation of the roles of the cytosolic N-terminus and His-rich loop of ZNT proteins using ZNT2 and ZNT3 chimeric mutants. *Scientific Reports*, *8*(1), 14084.

Fukunaka, A., Suzuki, T., Kurokawa, Y., Yamazaki, T., Fujiwara, N., Ishihara, K., Migaki, H., Okumura, K., Masuda, S., Yamaguchi-Iwai, Y., Nagao, M., & Kambe, T. (2009). Demonstration and Characterization of the Heterodimerization of ZnT5 and ZnT6 in the Early Secretory Pathway. *Journal of Biological Chemistry*, *284*(45), 30798–30806.

Gans, P., Sabatini, A., & Vacca, A. (1996). Investigation of equilibria in solution. Determination of equilibrium constants with the HYPERQUAD suite of programs. *Talanta*, *43*(10), 1739–1753.

Gasteiger, E., Hoogland, C., Gattiker, A., Duvaud, S., Wilkins, M. R., Appel, R. D., & Bairoch, A. (2005). Protein Identification and Analysis Tools on the ExPASy Server. In *The Proteomics Protocols Handbook* (pp. 571–607).

Georgiou, G., & Valax, P. (1996). Expression of correctly folded proteins in Escherichia coli. *Current Opinion in Biotechnology*, *7*(2), 190–197.

Gerber, P. A., Bellomo, E. A., Hodson, D. J., Meur, G., Solomou, A., Mitchell, R. K., Hollinshead, M., Chimienti, F., Bosco, D., Hughes, S. J., Johnson, P. R. V., & Rutter, G. (2014). Hypoxia lowers SLC30A8/ZnT8 expression and free cytosolic Zn2+ in pancreatic beta cells.

Diabetologia, *57*(8), 1635–1644.

Gerber, P. A., & Rutter, G. (2017). The Role of Oxidative Stress and Hypoxia in Pancreatic Beta-Cell Dysfunction in Diabetes Mellitus. *Antioxidants & Redox Signaling*, *26*(10), 501–518.

Golan, Y., Itsumura, N., Glaser, F., Berman, B., Kambe, T., & Assaraf, Y. G. (2016). Molecular Basis of Transient Neonatal Zinc Deficiency. *Journal of Biological Chemistry*, *291*(26), 13546–13559.

Goldenberg, R. L., Tamura, T., Neggers, Y., Copper, R. L., Johnston, K. E., DuBard, M. B., & Hauth, J. C. (1995). The effect of zinc supplementation on pregnancy outcome [see comments]. *Journal of the American Medical Association*, *274*(6), 463–468.

Grass, G., Fan, B., Rosen, B. P., Franke, S., Nies, D. H., & Rensing, C. (2001). ZitB (YbgR), a Member of the Cation Diffusion Facilitator Family, Is an Additional Zinc Transporter in Escherichia coli. *Journal of Bacteriology*, *183*(15), 4664–4667.

Guerrerio, A. L., & Berg, J. M. (2004). Metal Ion Affinities of the Zinc Finger Domains of the Metal Responsive Element-Binding Transcription Factor-1 (MTF1). *Biochemistry*, *43*(18), 5437–5444.

Günes, C., Heuchel, R., Georgiev, O., Müller, K. H., Lichtlen, P., Blüthmann, H., Marino, S., Aguzzi, A., & Schaffner, W. (1998). Embryonic lethality and liver degeneration in mice lacking the metal-responsive transcriptional activator MTF-1. *The EMBO Journal*, *17*(10), 2846–2854.

Gupta, S., Chai, J., Cheng, J., D'Mello, R., Chance, M. R., & Fu, D. (2014). Visualizing the kinetic power stroke that drives proton-coupled zinc(ii) transport. *Nature*, *512*(1), 101–104.

Hambidge, M., & Krebs, N. F. (2002). Interrelationships of key variables of human zinc homeostasis: relevance to dietary zinc requirements. *Annual Review of Nutrition*, *21*(1), 429–452.

Hardy, A. B., Serino, A. S., Wijesekara, N., Chimienti, F., & Wheeler, M. B. (2011). Regulation of glucagon secretion by zinc: lessons from the β cell-specific Znt8 knockout mouse model.

Diabetes, Obesity and Metabolism, *13*, 112–117.

Hardyman, J. E. J., Tyson, J., Jackson, K. A., Aldridge, C., Cockell, S. J., Wakeling, L. A., Valentine, R. A., & Ford, D. (2016). Zinc sensing by metal-responsive transcription factor 1 (MTF1) controls metallothionein and ZnT1 expression to buffer the sensitivity of the transcriptome response to zinc. *Metallomics*, *8*(3), 337–343.

Harris, E. D. (2000). Cellular copper transport and metabolism. *Annual Review of Nutrition*, *20*(1), 291–310.

Hattori, M., Tanaka, Y., Ishitani, R., & Nureki, O. (2007). Crystallization and preliminary X-ray diffraction analysis of the cytosolic domain of a cation diffusion facilitator family protein. *Acta Crystallographica Section F: Structural Biology and Crystallization Communications*, *63*(9), 771–773.

Hennigar, S. R., & Kelleher, S. L. (2015). TNFα Post-Translationally Targets ZnT2 to Accumulate Zinc in Lysosomes. *Journal of Cellular Physiology*, *230*(10), 2345–2350.

Hessels, A. M., Chabosseau, P., Bakker, M. H., Engelen, W., Rutter, G. A., Taylor, K. M., & Merkx, M. (2015). EZinCh-2: A Versatile, Genetically Encoded FRET Sensor for Cytosolic and Intraorganelle Zn2+ Imaging. *ACS Chemical Biology*, *10*(9), 2126–2134.

Higuchi, T., Hattori, M., Tanaka, Y., Ishitani, R., & Nureki, O. (2009). Crystal structure of the cytosolic domain of the cation diffusion facilitator family protein. *Proteins: Structure, Function and Bioinformatics*, *76*(3), 768–771.

Hildebrand, M. S., Phillips, A. M., Mullen, S. A., Adlard, P. A., Hardies, K., Damiano, J. A., Wimmer, V., Bellows, S. T., McMahon, J. M., Burgess, R., Hendrickx, R., Weckhuysen, S., Suls, A., De Jonghe, P., Scheffer, I. E., Petrou, S., Berkovic, S. F., & Reid, C. A. (2015). Loss of synaptic Zn2+ transporter function increases risk of febrile seizures. *Scientific Reports*, *5*, 17816.

Hoch, E., Lin, W., Chai, J., Hershfinkel, M., Fu, D., & Sekler, I. (2012). Histidine pairing at the metal transport site of mammalian ZnT transporters controls Zn2+ over Cd2+ selectivity.

Proceedings of the National Academy of Sciences, *109*(19), 7202–7207.

Höfer, N., Kolaj, O., Li, H., Cherezov, V., Gillilan, R., Wall, J. G., & Caffrey, M. (2007). Crystallization and preliminary X-ray diffraction analysis of a soluble domain of the putative zinc transporter CzrB from Thermus thermophilus. *Acta Crystallographica Section F: Structural Biology and Crystallization Communications*, *63*(8), 673–677.

Hogstrand, C., & Maret, W. (2016). Genetics of Human Zinc Deficiencies. In *eLS* (pp. 1–8).

Hou, J. C., Min, L., & Pessin, J. E. (2009). Chapter 16 Insulin Granule Biogenesis, Trafficking and Exocytosis. In *Vitamins and hormones* (Vol. 80, pp. 473–506).

Ilari, A., Alaleona, F., Tria, G., Petrarca, P., Battistoni, A., Zamparelli, C., Verzili, D., Falconi, M., & Chiancone, E. (2014). The Salmonella enterica ZinT structure, zinc affinity and interaction with the high-affinity uptake protein ZnuA provide insight into the management of periplasmic zinc. *Biochimica et Biophysica Acta - General Subjects*, *1840*(1), 535–544.

Irving, H., & Williams, R. J. P. (1948). Order of stability of metal complexes. *Nature*, *162*(4123), 746–747.

Jackson, M. J. (1989). Physiology of Zinc: General Aspects. In *Zinc in Human Biology* (pp. 1–14).

Jeong, J., & Eide, D. J. (2013). The SLC39 family of zinc transporters. *Molecular Aspects of Medicine*, *34*(2–3), 612–619.

Jirakulaporn, T., & Muslin, A. J. (2004). Cation Diffusion Facilitator Proteins Modulate Raf-1 Activity. *Journal of Biological Chemistry*, *279*(26), 27807–27815.

Kambe, T. (2011). An Overview of a Wide Range of Functions of ZnT and Zip Zinc Transporters in the Secretory Pathway. *Bioscience, Biotechnology, and Biochemistry*, *75*(6), 1036–1043.

Kambe, T., Hashimoto, A., & Fujimoto, S. (2014). Current understanding of ZIP and ZnT zinc transporters in human health and diseases. *Cellular and Molecular Life Sciences*, *71*(17), 3281–3295.

Kambe, T., Narita, H., Yamaguchi-Iwai, Y., Hirose, J., Amano, T., Sugiura, N., Sasaki, R., Mori, K.,

Iwanaga, T., & Nagao, M. (2002). Cloning and Characterization of a Novel Mammalian Zinc Transporter, Zinc Transporter 5, Abundantly Expressed in Pancreatic β Cells. *Journal of Biological Chemistry*, *277*(21), 19049–19055.

Kambe, T., Suzuki, T., Nagao, M., & Yamaguchi-Iwai, Y. (2006). Sequence similarity and functional relationship among eukaryotic ZIP and CDF transporters. *Genomics, Proteomics & Bioinformatics*, *4*(1), 1–9.

Kambe, T., Tsuji, T., Hashimoto, A., & Itsumura, N. (2015). The Physiological, Biochemical, and Molecular Roles of Zinc Transporters in Zinc Homeostasis and Metabolism. *Physiological Reviews*, *95*(3), 749–784.

Keilin, D., & Mann, T. (1939). Carbonic Anhydrase. *Nature*, *144*(3644), 442–443.

Kim, I., Kang, E. S., Yim, Y. S., Ko, S. J., Jeong, S.-H., Rim, J. H., Kim, Y. S., Ahn, C. W., Cha, B. S., Lee, H. C., & Kim, C. H. (2011). A low-risk ZnT-8 allele (W325) for post-transplantation diabetes mellitus is protective against cyclosporin A-induced impairment of insulin secretion. *The Pharmacogenomics Journal*, *11*(3), 191–198.

Klomp, L. W., Lin, S. J., Yuan, D. S., Klausner, R. D., Culotta, V. C., & Gitlin, J. D. (1997). Identification and functional expression of HAH1, a novel human gene involved in copper homeostasis. *The Journal of Biological Chemistry*, *272*(14), 9221–9226.

Knight, M. I., & Chambers, P. J. (2003). Problems Associated with Determining Protein Concentration: A Comparison of Techniques for Protein Estimations. *Molecular Biotechnology*, *23*(1), 19–28.

Kocyła, A., Pomorski, A., & Krężel, A. (2017). Molar absorption coefficients and stability constants of Zincon metal complexes for determination of metal ions and bioinorganic applications. *Journal of Inorganic Biochemistry*, *176*, 53–65.

Krężel, A., & Maret, W. (2007). Dual Nanomolar and Picomolar Zn(II) Binding Properties of Metallothionein. *Journal of the American Chemical Society*, *129*(35), 10911–10921.

Krężel, A., & Maret, W. (2006). Zinc-buffering capacity of a eukaryotic cell at physiological pZn.

Journal of Biological Inorganic Chemistry, *11*(8), 1049–1062.

Krężel, A., & Maret, W. (2016). The biological inorganic chemistry of zinc ions. *Archives of Biochemistry and Biophysics*, *611*, 3–19.

Laity, J. H., & Andrews, G. K. (2007). Understanding the mechanisms of zinc-sensing by metal-response element binding transcription factor-1 (MTF-1). *Archives of Biochemistry and Biophysics*, *463*(2), 201–210.

Langmade, S. J., Ravindra, R., Daniels, P. J., & Andrews, G. K. (2000). The Transcription Factor MTF-1 Mediates Metal Regulation of the Mouse ZnT1 Gene. *Journal of Biological Chemistry*, *275*(44), 34803–34809.

Lawson, R., Maret, W., & Hogstrand, C. (2018). Prolonged stimulation of insulin release from MIN6 cells causes zinc depletion and loss of β-cell markers. *Journal of Trace Elements in Medicine and Biology*, *49*, 51–59.

Lee, S., Rivera, O. C., & Kelleher, S. L. (2017). Zinc transporter 2 interacts with vacuolar ATPase and is required for polarization, vesicle acidification, and secretion in mammary epithelial cells. *Journal of Biological Chemistry*, *292*(52), 21598–21613.

Lefebvre, B., Vandewalle, B., Balavoine, A. S., Queniat, G., Moerman, E., Vantyghem, M. C., Gmyr, V., Pawlowski, V., Kerr-Conte, J., & Pattou, F. (2012). Regulation and functional effects of ZNT8 in human pancreatic islets. *Journal of Endocrinology*, *214*(2), 225–232.

Lehrer, S. S. (1971). Solute perturbation of protein fluorescence. The quenching of the tryptophyl fluorescence of model compounds and of lysozyme by iodide ion. *Biochemistry*, *10*(17), 3254–3263.

Lemaire, K., Ravier, M. A., Schraenen, A., Creemers, J. W. M., Van de Plas, R., Granvik, M., Van Lommel, L., Waelkens, E., Chimienti, F., Rutter, G., Gilon, P., Veld, P. A. i., & Schuit, F. C. (2009). Insulin crystallization depends on zinc transporter ZnT8 expression, but is not required for normal glucose homeostasis in mice. *Proceedings of the National Academy of Sciences*, *106*(35), 14872–14877.

Lenzen, S. (2008). Oxidative stress: the vulnerable β-cell. *Biochemical Society Transactions*, *36*(3), 343–347.

Levy, S., Beharier, O., Etzion, Y., Mor, M., Buzaglo, L., Shaltiel, L., Gheber, L. A., Kahn, J., Muslin, A. J., Katz, A., Gitler, D., & Moran, A. (2009). Molecular basis for zinc transporter 1 action as an endogenous inhibitor of L-type calcium channels. *The Journal of Biological Chemistry*, *284*(47), 32434–32443.

Li, Y., Kimura, T., Laity, J. H., & Andrews, G. K. (2006). The zinc-sensing mechanism of mouse MTF-1 involves linker peptides between the zinc fingers. *Molecular and Cellular Biology*, *26*(15), 5580–5587.

Lichten, L. A., & Cousins, R. J. (2009). Mammalian Zinc Transporters: Nutritional and Physiologic Regulation. *Annual Review of Nutrition*, *29*(1), 153–176.

Lin, W., Chai, J., Love, J., & Fu, D. (2010). Selective electrodiffusion of zinc ions in a Zrt-, Irt-like protein, ZIPB. *The Journal of Biological Chemistry*, *285*(50), 39013–39020.

Lin, Z., Wang, Y., Zhang, B., & Jin, Z. (2018). Association of type 2 diabetes susceptible genes GCKR, SLC30A8, and FTO polymorphisms with gestational diabetes mellitus risk: a meta-analysis. *Endocrine*, *62*(1), 34–45.

Lopez-Redondo, M. L., Coudray, N., Zhang, Z., Alexopoulos, J., & Stokes, D. L. (2018). Structural basis for the alternating access mechanism of the cation diffusion facilitator YiiP. *Proceedings of the National Academy of Sciences*, *115*(12), 3042–3047.

Lopez, V., & Kelleher, S. L. (2009). Zinc transporter-2 (ZnT2) variants are localized to distinct subcellular compartments and functionally transport zinc. *Biochemical Journal*, *422*(1), 43–52.

Lu, M., Chai, J., & Fu, D. (2009). Structural basis for autoregulation of the zinc transporter YiiP. *Nature Structural and Molecular Biology*, *16*(10), 1063–1067.

Lu, M., & Fu, D. (2007). Structure of the zinc transporter YiiP. *Science*, *317*(5845), 1746–1748.

Maret, W. (2009). Molecular aspects of human cellular zinc homeostasis: redox control of zinc

potentials and zinc signals. *BioMetals*, *22*(1), 149–157.

Maret, W. (2013). Zinc Biochemistry: From a Single Zinc Enzyme to a Key Element of Life. *Advances in Nutrition*, *4*(1), 82–91.

Maret, W. (2015, February). Analyzing free zinc(II) ion concentrations in cell biology with fluorescent chelating molecules. *Metallomics*, Vol. 7, pp. 202–211.

Maret, W. (2017). Zinc in Cellular Regulation: The Nature and Significance of "Zinc Signals". *International Journal of Molecular Sciences*, *18*(11).

Maret, W., & Li, Y. (2009). Coordination Dynamics of Zinc in Proteins. *Chemical Reviews*, *109*(10), 4682–4707.

Maret, W., & Sandstead, H. (2006). Zinc requirements and the risks and benefits of zinc supplementation. *Journal of Trace Elements in Medicine and Biology*, *20*(1), 3–18.

Maywald, M., Wessels, I., & Rink, L. (2017). Zinc Signals and Immunity. *International Journal of Molecular Sciences*, *18*(10), 2222.

McClain, C. J. (1985). Zinc metabolism in malabsorption syndromes. *Journal of the American College of Nutrition*, *4*(1), 49–64.

Merriman, C., Huang, Q., Rutter, G., & Fu, D. (2016). Lipid-tuned zinc transport activity of human ZnT8 protein correlates with risk for type-2 diabetes. *Journal of Biological Chemistry*, *291*(53), 26950–26957.

Micsonai, A., Wien, F., Kernya, L., Lee, Y.-H., Goto, Y., Réfrégiers, M., & Kardos, J. (2015). Accurate secondary structure prediction and fold recognition for circular dichroism spectroscopy. *Proceedings of the National Academy of Sciences*, *112*(24), E3095-103.

Miller, J., McLachlan, A. D., & Klug, A. (1985). Repetitive zinc-binding domains in the protein transcription factor IIIA from Xenopus oocytes. *The EMBO Journal*, *4*(6), 1609–1614.

Montanini, B., Blaudez, D., Jeandroz, S., Sanders, D., & Chalot, M. (2007). Phylogenetic and functional analysis of the Cation Diffusion Facilitator (CDF) family: improved signature and prediction of substrate specificity. *BMC Genomics*, *8*, 107.

Mor, M., Beharier, O., Levy, S., Kahn, J., Dror, S., Blumenthal, D., Gheber, L. A., Peretz, A., Katz, A., Moran, A., & Etzion, Y. (2012). ZnT-1 enhances the activity and surface expression of T-type calcium channels through activation of Ras-ERK signaling. *American Journal of Physiology-Cell Physiology*, *303*(2), C192–C203.

Mukherjee, A., Morales-Scheihing, D., Butler, P. C., & Soto, C. (2015). Type 2 diabetes as a protein misfolding disease. *Trends in Molecular Medicine*, *21*(7), 439–449.

Multhaup, G., Strausak, D., Bissig, K.-D., & Solioz, M. (2001). Interaction of the CopZ Copper Chaperone with the CopA Copper ATPase of Enterococcus hirae Assessed by Surface Plasmon Resonance. *Biochemical and Biophysical Research Communications*, *288*(1), 172–177.

Murgia, C., Devirgiliis, C., Mancini, E., Donadel, G., Zalewski, P., & Perozzi, G. (2009). Diabetes-linked zinc transporter ZnT8 is a homodimeric protein expressed by distinct rodent endocrine cell types in the pancreas and other glands. *Nutrition, Metabolism and Cardiovascular Diseases*, *19*(6), 431–439.

Nicolson, T. J., Bellomo, E. A., Wijesekara, N., Loder, M. K., Baldwin, J. M., Gyulkhandanyan, A. V., Koshkin, V., Tarasov, A. I., Carzaniga, R., Kronenberger, K., … Rutter, G. (2009). Insulin storage and glucose homeostasis in mice null for the granule zinc transporter ZnT8 and studies of the type 2 diabetes-associated variants. *Diabetes*, *58*(9), 2070–2083.

Nieba, L., Nieba-Axmann, S. E., Persson, A., Hämäläinen, M., Edebratt, F., Hansson, A., Lidholm, J., Magnusson, K., Karlsson, Å. F., & Plückthun, A. (1997). BIACORE Analysis of Histidine-Tagged Proteins Using a Chelating NTA Sensor Chip. *Analytical Biochemistry*, *252*(2), 217–228.

Nies, D. H. (2007). How cells control zinc homeostasis. *Science*, *317*(5845), 1695–1696.

Nishito, Y., Tsuji, N., Fujishiro, H., Takeda, T. A., Yamazaki, T., Teranishi, F., Okazaki, F., Matsunaga, A., Tuschl, K., Rao, R., Kono, S., Miyajima, H., Narita, H., Himeno, S., & Kambe, T. (2016). Direct comparison of manganese detoxification/efflux proteins and molecular

characterization of ZnT10 protein as a manganese transporter. *Journal of Biological Chemistry*, *291*(28), 14773–14787.

O'Roak, B. J., Deriziotis, P., Lee, C., Vives, L., Schwartz, J. J., Girirajan, S., Karakoc, E., MacKenzie, A. P., Ng, S. B., Baker, C., Rieder, M. J., Nickerson, D. A., Bernier, R., Fisher, S. E., Shendure, J., & Eichler, E. E. (2011). Exome sequencing in sporadic autism spectrum disorders identifies severe de novo mutations. *Nature Genetics*, *43*(6), 585–589.

Orme-Johnson, W. H. (1973). Iron-Sulfur Proteins: Structure and Function. *Annual Review of Biochemistry*, *42*(1), 159–204.

Outten, C. E., & O'Halloran, T. V. (2001). Femtomolar Sensitivity of Metalloregulatory Proteins Controlling Zinc Homeostasis. *Science*, *292*(5526), 2488–2492.

Outten, C. E., Outten, F. W., & O'Halloran, T. V. (1999). DNA distortion mechanism for transcriptional activation by ZntR, a Zn(II)-responsive MerR homologue in Escherichia coli. *The Journal of Biological Chemistry*, *274*(53), 37517–37524.

Palmiter, R., & Findley, S. D. (1995). Cloning and functional characterization of a mammalian zinc transporter that confers resistance to zinc. *The EMBO Journal*, *14*(4), 639–649.

Palmiter, R., & Huang, L. (2004). Efflux and compartmentalization of zinc by members of the SLC30 family of solute carriers. *Pflugers Archiv European Journal of Physiology*, *447*(5), 744–751.

Parsons, D. S., Hogstrand, C., & Maret, W. (2018). The C-terminal cytosolic domain of the human zinc transporter ZnT8 and its diabetes risk variant. *FEBS Journal*, *285*(7), 1237–1250.

Patzer, S. I., & Hantke, K. (1998). The ZnuABC high-affinity zinc uptake system and its regulator Zur in Escherichia coli. *Molecular Microbiology*, *28*(6), 1199–1210.

Perez, Y., Shorer, Z., Liani-Leibson, K., Chabosseau, P., Kadir, R., Volodarsky, M., Halperin, D., Barber-Zucker, S., Shalev, H., Schreiber, R., Gradstein, L., Gurevich, E., Zarivach, R., Rutter, G., Landau, D., & Birk, O. S. (2017). SLC30A9 mutation affecting intracellular zinc

homeostasis causes a novel cerebro-renal syndrome. *Brain*, *140*(4), 928–939.

Petkovic, V., Miletta, M. C., Eblé, A., Flück, C. E., & Mullis, P.-E. (2014). Alteration of ZnT5-Mediated Zinc Import into the Early Secretory Pathway Affects the Secretion of Growth Hormone from Rat Pituitary Cells. *Hormone Research in Paediatrics*, *82*(4), 245–251.

Podar, D., Scherer, J., Noordally, Z., Herzyk, P., Nies, D., & Sanders, D. (2012). Metal selectivity determinants in a family of transition metal transporters. *The Journal of Biological Chemistry*, *287*(5), 3185–3196.

Pound, L. D., Hang, Y., Sarkar, S. A., Wang, Y., Milam, L. A., Oeser, J. K., Printz, R. L., Lee, C. E., Stein, R., Hutton, J. C., & O'Brien, R. M. (2011). The pancreatic islet β-cell-enriched transcription factor Pdx-1 regulates *Slc30a8* gene transcription through an intronic enhancer. *Biochemical Journal*, *433*(1), 95–105.

Pound, L. D., Sarkar, S. A., Benninger, R. K. P., Wang, Y., Suwanichkul, A., Shadoan, M. K., Printz, R. L., Oeser, J. K., Lee, C. E., Piston, D. W., McGuinness, O. P., Hutton, J. C., Powell, D. R., & O'Brien, R. M. (2009). Deletion of the mouse *Slc30a8* gene encoding zinc transporter-8 results in impaired insulin secretion. *Biochemical Journal*, *421*(3), 371–376.

Pound, L. D., Sarkar, S. A., Ustione, A., Dadi, P. K., Shadoan, M. K., Lee, C. E., Walters, J. A., Shiota, M., McGuinness, O. P., Jacobson, D. A., Piston, D. W., Hutton, J. C., Powell, D. R., & O'Brien, R. M. (2012). The Physiological Effects of Deleting the Mouse Slc30a8 Gene Encoding Zinc Transporter-8 Are Influenced by Gender and Genetic Background. *PLoS ONE*, *7*(7), e40972.

Prasad, A. (2013). Discovery of Human Zinc Deficiency: Its Impact on Human Health and Disease. *Advances in Nutrition*, *4*(2), 176–190.

Prasad, A., Halsted, J. A., & Nadimi, M. (1961). Syndrome of iron deficiency anemia, hepatsplenomegaly, hypogonadism, dwarfism, and geophagia. *American Journal of Medicine*, *31*(4), 532–546.

Prasad, A., Miale, A., Farid, Z., Sandstead, H. H., Schulert, A. R., & Darby, W. J. (1963).

Biochemical studies on dwarfism, hypogonadism, and anemia. *Archives of Internal Medicine*, *111*, 407–428.

Pufahl, R. A., Singer, C. P., Peariso, K. L., Lin, S. J., Schmidt, P. J., Fahrni, C. J., Cizewski Culotta, V., Penner-Hahn, J. E., & O'Halloran, T. V. (1997). Metal ion chaperone function of the soluble Cu(I) receptor Atx1. *Science*, *278*(5339), 853–856.

Qin, Y., Dittmer, P. J., Park, J. G., Jansen, K. B., & Palmer, A. E. (2011). Measuring steady-state and dynamic endoplasmic reticulum and Golgi Zn2+ with genetically encoded sensors. *Proceedings of the National Academy of Sciences*, *108*(18), 7351–7356.

Radtke, F., Heuchel, R., Georgiev, O., Hergersberg, M., Gariglio, M., Dembic, Z., & Schaffner, W. (1993). Cloned transcription factor MTF-1 activates the mouse metallothionein I promoter. *The EMBO Journal*, *12*(4), 1355–1362.

Ramos, S., Schuldiner, S., & Kaback, H. R. (1976). The electrochemical gradient of protons and its relationship to active transport in Escherichia coli membrane vesicles. *Proceedings of the National Academy of Sciences*, *73*(6), 1892–1896.

Raulin, J. (1869). Etudes chimiques sur la végétation. *Ann Sci Nat Bot Biol Veg*, *11*, 92–299.

Rensing, C., Fan, B., Sharma, R., Mitra, B., & Rosen, B. P. (2000). CopA: An Escherichia coli Cu(I)-translocating P-type ATPase. *Proceedings of the National Academy of Sciences*, *97*(2), 652–656.

Reyes-Caballero, H., Campanello, G. C., & Giedroc, D. P. (2011). Metalloregulatory proteins: Metal selectivity and allosteric switching. *Biophysical Chemistry*, *156*(2–3), 103–114.

Rink, L. (2011). *Zinc in human health*.

Rosenzweig, A., & O'Halloran, T. V. (2000). Structure and chemistry of the copper chaperone proteins. *Current Opinion in Chemical Biology*, *4*(2), 140–147.

Rosenzweig, A., Wernimont, A. K., Huffman, D. L., Lamb, A. L., & O'Halloran, T. V. (2000). Structural basis for copper transfer by the metallochaperone for the Menkes/Wilson disease proteins. *Nature Structural Biology*, *7*(9), 766–771.

Russell, D., & Soulimane, T. (2012). Evidence for zinc and cadmium binding in a CDF transporter lacking the cytoplasmic domain. *FEBS Letters*, *586*(24), 4332–4338.

Rutherford, J. C., & Bird, A. J. (2004). Metal-responsive transcription factors that regulate iron, zinc, and copper homeostasis in eukaryotic cells. *Eukaryotic Cell*, *3*(1), 1–13.

Rutter, G., & Chimienti, F. (2015). SLC30A8 mutations in type 2 diabetes. *Diabetologia*, *58*(1), 31–36.

Salazar, G., Falcon-Perez, J. M., Harrison, R., Faundez, V., & Hastrup, H. (2009). SLC30A3 (ZnT3) Oligomerization by Dityrosine Bonds Regulates Its Subcellular Localization and Metal Transport Capacity. *PLoS ONE*, *4*(6), e5896.

Salazar, G., Love, R., Werner, E., Doucette, M. M., Cheng, S., Levey, A., & Faundez, V. (2004). The Zinc Transporter ZnT3 Interacts with AP-3 and It Is Preferentially Targeted to a Distinct Synaptic Vesicle Subpopulation. *Molecular Biology of the Cell*, *15*(2), 575–587.

Sandstead, H. (1995). Requirements and toxicity of essential trace elements, illustrated by zinc and copper. *American Journal of Clinical Nutrition*, *61*(3 SUPPL.), 621S–624S.

Sandstead, H., Penland, J. G., Alcock, N. W., Dayal, H. H., Chen, X. C., Li, J. S., Zhao, F., & Yang, J. J. (1998). Effects of repletion with zinc and other micronutrients on neuropsychologic performance and growth of Chinese children. *American Journal of Clinical Nutrition*, *68*(2 SUPPL.), 470S–475S.

Sandstead, H., & Smith, J. C. (2018). Deliberations and Evaluations of Approaches, Endpoints and Paradigms for Determining Zinc Dietary Recommendations. *The Journal of Nutrition*, *126*(suppl_9), 2410S–2418S.

Saxena, R., Voight, B. F., Lyssenko, V., Burtt, N. P., de Bakker, P. I. W., Chen, H., Roix, J. J., Kathiresan, S., Hirschhorn, J. N., Daly, M. J., … Purcell, S. (2007). Genome-Wide Association Analysis Identifies Loci for Type 2 Diabetes and Triglyceride Levels. *Science*, *316*(5829), 1331–1336.

Scott, D. A., & Fisher, A. M. (1938). The insulin and the zinc content of normal and diabetic

pancreas. *J. Clinical Invest.*, *17*(6), 725.

Seo, Y. A., Lopez, V., & Kelleher, S. L. (2011). A histidine-rich motif mediates mitochondrial localization of ZnT2 to modulate mitochondrial function. *American Journal of Physiology. Cell Physiology*, *300*(6), C1479-89.

Shingu, Y., Kudo, T., Ohsato, S., Kimura, M., Ono, Y., Yamaguchi, I., & Hamamoto, H. (2005). Characterization of genes encoding metal tolerance proteins isolated from Nicotiana glauca and Nicotiana tabacum. *Biochemical and Biophysical Research Communications*, *331*(2), 675–680.

Shusterman, E., Beharier, O., Shiri, L., Zarivach, R., Etzion, Y., Campbell, C. R., Lee, I.-H., Okabayashi, K., Dinudom, A., Cook, D. I., Katz, A., & Moran, A. (2014). ZnT-1 extrudes zinc from mammalian cells functioning as a Zn 2+ /H + exchanger. *Metallomics*, *6*(6), 1656–1663.

Sim, D. L. C., & Chow, V. T. K. (1999). The Novel Human HUEL (C4orf1) Gene Maps to Chromosome 4p12–p13 and Encodes a Nuclear Protein Containing the Nuclear Receptor Interaction Motif. *Genomics*, *59*(2), 224–233.

Sivashanmugam, A., Murray, V., Cui, C., Zhang, Y., Wang, J., & Li, Q. (2009). Practical protocols for production of very high yields of recombinant proteins using Escherichia coli. *Protein Science*, *18*(5), 936–948.

Sladek, R., Rocheleau, G., Rung, J., Dina, C., Shen, L., Serre, D., Boutin, P., Vincent, D., Belisle, A., Hadjadj, S., … Froguel, P. (2007). A genome-wide association study identifies novel risk loci for type 2 diabetes. *Nature*, *445*(7130), 881–885.

Solomons, N. W., Rosenberg, I. H., Sandstead, H. H., & Vo Khactu, K. P. (1977). Zinc deficiency in Crohn's disease. *Digestion*, *16*(1–2), 87–95.

Solomou, A., Meur, G., Bellomo, E., Hodson, D. J., Tomas, A., Li, S. M., Philippe, E., Herrera, P. L., Magnan, C., & Rutter, G. (2015). The zinc transporter Slc30a8/ZnT8 is required in a subpopulation of pancreatic α;-cells for hypoglycemia-induced glucagon secretion.

Journal of Biological Chemistry, *290*(35), 21432–21442.

Spada, S., Pembroke, T. J., & Wall, G. J. (2002). Isolation of a novel Thermus thermophilus metal efflux protein that improves Escherichia coli growth under stress conditions. *Extremophiles*, *6*(4), 301–308.

Stawikowski, M., & Fields, G. B. (2012). Introduction to peptide synthesis. *Current Protocols in Protein Science*, *1*(SUPPL.69), Unit 18.1.

Steel, L., & Cousins, R. J. (1985). Kinetics of zinc absorption by luminally and vascularly perfused rat intestine. *American Journal of Physiology-Gastrointestinal and Liver Physiology*, *248*(1), G46–G53.

Strickland, E. H. (1974). Aromatic contributions to circular dichroism spectra of proteins. *CRC Critical Reviews in Biochemistry*, *2*(1), 113–175.

Suzuki, T., Ishihara, K., Migaki, H., Ishihara, K., Nagao, M., Yamaguchi-Iwai, Y., & Kambe, T. (2005). Two Different Zinc Transport Complexes of Cation Diffusion Facilitator Proteins Localized in the Secretory Pathway Operate to Activate Alkaline Phosphatases in Vertebrate Cells. *Journal of Biological Chemistry*, *280*(35), 30956–30962.

Syring, K. E., Boortz, K. A., Oeser, J. K., Ustione, A., Platt, K. A., Shadoan, M. K., McGuinness, O. P., Piston, D. W., Powell, D. R., & O'Brien, R. M. (2016). Combined Deletion of *Slc30a7* and *Slc30a8* Unmasks a Critical Role for ZnT8 in Glucose-Stimulated Insulin Secretion. *Endocrinology*, *157*(12), 4534–4541.

Tamaki, M., Fujitani, Y., Hara, A., Uchida, T., Tamura, Y., Takeno, K., Kawaguchi, M., Watanabe, T., Ogihara, T., Fukunaka, A., … Watada, H. (2013). The diabetes-susceptible gene SLC30A8/ZnT8 regulates hepatic insulin clearance. *Journal of Clinical Investigation*, *123*(10), 4513–4524.

Tanaka, N., Kawachi, M., Fujiwara, T., & Maeshima, M. (2013). Zinc-binding and structural properties of the histidine-rich loop of *Arabidopsis thaliana* vacuolar membrane zinc transporter MTP1. *FEBS Open Bio*, *3*(1), 218–224.

Todd, W. R., Elvehjem, C. A., & Hart, E. B. (1934). Zinc in the nutrition of the rat. *American Journal of Physiology Legacy*, *107*(4), 146–156.

Tuschl, K., Clayton, P. T., Gospe, S. M., Gulab, S., Ibrahim, S., Singhi, P., Aulakh, R., Ribeiro, R. T., Barsottini, O. G., Zaki, M. S., Del Rosario, M. L., Dyack, S., Price, V., Rideout, A., Gordon, K., Wevers, R. A., "Kling" Chong, W. K., & Mills, P. B. (2012). Syndrome of Hepatic Cirrhosis, Dystonia, Polycythemia, and Hypermanganesemia Caused by Mutations in SLC30A10 , a Manganese Transporter in Man. *The American Journal of Human Genetics*, *90*(3), 457–466.

Valentine, R. A., Jackson, K. A., Christie, G. R., Mathers, J. C., Taylor, P. M., & Ford, D. (2007). ZnT5 variant B is a bidirectional zinc transporter and mediates zinc uptake in human intestinal Caco-2 cells. *The Journal of Biological Chemistry*, *282*(19), 14389–14393.

Vallee, B. L., & Falchuk, K. H. (1993). The biochemical basis of zinc physiology. *Physiological Reviews*, *73*(1), 79–118.

Vašák, M., & Meloni, G. (2011, October 7). Chemistry and biology of mammalian metallothioneins. *Journal of Biological Inorganic Chemistry*, Vol. 16, pp. 1067–1078.

Ventura, S., & Villaverde, A. (2006). Protein quality in bacterial inclusion bodies. *Trends in Biotechnology*, *24*(4), 179–185.

Vinkenborg, J. L., Nicolson, T. J., Bellomo, E. A., Koay, M. S., Rutter, G., & Merkx, M. (2009). Genetically encoded FRET sensors to monitor intracellular Zn2+ homeostasis. *Nature Methods*, *6*(10), 737–740.

Vivian, J. T., & Callis, P. R. (2001). Mechanisms of Tryptophan Fluorescence Shifts in Proteins. *Biophysical Journal*, *80*(5), 2093–2109.

Waldron, K. J., Rutherford, J. C., Ford, D., & Robinson, N. J. (2009). Metalloproteins and metal sensing. *Nature*, *460*(7257), 823–830.

Wang, F.-H., Qiao, K., Liang, S., Tian, S.-Q., Tian, Y.-B., Wang, H., & Chai, T.-Y. (2018). Triticum urartu MTP1: its ability to maintain Zn2+ and Co2+ homeostasis and metal selectivity

determinants. *Plant Cell Reports*, 1–14.

Wastney, M. E., Aamodt, R. L., Rumble, W. F., & Henkin, R. I. (1986). Kinetic analysis of zinc metabolism and its regulation in normal humans. *American Journal of Physiology-Regulatory, Integrative and Comparative Physiology*, *251*(2), R398–R408.

Watly, J., Simonovsky, E., Barbosa, N., Spodzieja, M., Wieczorek, R., Rodziewicz-Motowidlo, S., Miller, Y., & Kozlowski, H. (2015). African Viper Poly-His Tag Peptide Fragment Efficiently Binds Metal Ions and Is Folded into an α-Helical Structure. *Inorganic Chemistry*, *54*(16), 7692–7702.

Wei, Y., & Fu, D. (2005). Selective metal binding to a membrane-embedded aspartate in the Escherichia coli metal transporter YiiP (FieF). *Journal of Biological Chemistry*, *280*(40), 33716–33724.

Wei, Y., & Fu, D. (2006). Binding and transport of metal ions at the dimer interface of the Escherichia coli metal transporter YiiP. *Journal of Biological Chemistry*, *281*(33), 23492–23502.

Wenzlau, J. M., Juhl, K., Yu, L., Moua, O., Sarkar, S. A., Gottlieb, P., Rewers, M., Eisenbarth, G. S., Jensen, J., Davidson, H. W., & Hutton, J. C. (2007). The cation efflux transporter ZnT8 (Slc30A8) is a major autoantigen in human type 1 diabetes. *Proceedings of the National Academy of Sciences*, *104*(43), 17040–17045.

Wenzlau, J. M., Liu, Y., Yu, L., Moua, O., Fowler, K. T., Rangasamy, S., Walters, J., Eisenbarth, G. S., Davidson, H. W., & Hutton, J. C. (2008). A Common Nonsynonymous Single Nucleotide Polymorphism in the SLC30A8 Gene Determines ZnT8 Autoantibody Specificity in Type 1 Diabetes. *Diabetes*, *57*(10), 2693–2697.

Wijesekara, N., Dai, F. F., Hardy, A. B., Giglou, P. R., Bhattacharjee, A., Koshkin, V., Chimienti, F., Gaisano, H. Y., Rutter, G., & Wheeler, M. B. (2010). Beta cell-specific Znt8 deletion in mice causes marked defects in insulin processing, crystallisation and secretion. *Diabetologia*, *53*(8), 1656–1668.

Williams, R. J. P. (1987). The biochemistry of zinc. *Polyhedron*, *6*(1), 61–69.

Zalewski, P. D., Millard, S. H., Forbes, I. J., Kapaniris, O., Slavotinek, A., Betts, W. H., Ward, A. D., Lincoln, S. F., & Mahadevan, I. (1994). Video image analysis of labile zinc in viable pancreatic islet cells using a specific fluorescent probe for zinc. *Journal of Histochemistry & Cytochemistry*, *42*(7), 877–884.

Zaytuni, N., Uebe, R., Maes, M., Davidov, G., Baram, M., Raschdorf, O., Nadav-Tsubery, M., Kolusheva, S., Bitton, R., Goobes, G., Friedler, A., Miller, Y., Schüler, D., & Zarivach, R. (2014). Cation diffusion facilitators transport initiation and regulation is mediated by cation induced conformational changes of the cytoplasmic domain. *PLoS ONE*, *9*(3), e92141.

Zeytuni, N., Offer, T., Davidov, G., & Zarivach, R. (2012). Crystallization and preliminary crystallographic analysis of the C-terminal domain of MamM, a magnetosome-associated protein from Magnetospirillum gryphiswaldense MSR-1. *Acta Crystallographica. Section F, Structural Biology and Crystallization Communications*, *68*(Pt 8), 927–930.

Zeytuni, N., Uebe, R., Maes, M., Davidov, G., Baram, M., Raschdorf, O., Friedler, A., Miller, Y., Schüler, D., & Zarivach, R. (2014). Bacterial magnetosome biomineralization - A novel platform to study molecular mechanisms of human CDF-related type-II diabetes. *PLoS ONE*, *9*(5), e97154.

Zhang, T., Sui, D., & Hu, J. (2016). Structural insights of ZIP4 extracellular domain critical for optimal zinc transport. *Nature Communications*, *7*, 11979.

Zhang, X., Guan, T., Yang, B., Chi, Z., Wang, Z.-Y., & Gu, H. F. (2018). A novel role for zinc transporter 8 in the facilitation of zinc accumulation and regulation of testosterone synthesis in Leydig cells of human and mouse testicles. *Metabolism*, *88*, 40–50.

Zhao, Y., Feresin, R. G., Falcon-Perez, J. M., & Salazar, G. (2016). Differential Targeting of SLC30A10/ZnT10 Heterodimers to Endolysosomal Compartments Modulates EGF-Induced MEK/ERK1/2 Activity. *Traffic*, *17*(3), 267–288.

Zimmermann, M., Clarke, O., Gulbis, J. M., Keizer, D. W., Jarvis, R. S., Cobbett, C. S., Hinds, M. G., Xiao, Z., & Wedd, A. G. (2009). Metal Binding Affinities of *Arabidopsis* Zinc and Copper Transporters: Selectivities Match the Relative, but Not the Absolute, Affinities of their Amino-Terminal Domains,. *Biochemistry*, *48*(49), 11640–11654.

Zogzas, C. E., Aschner, M., & Mukhopadhyay, S. (2016). Structural elements in the transmembrane and cytoplasmic domains of the metal transporter SLC30A10 are required for its manganese efflux activity. *Journal of Biological Chemistry*, *291*(31), 15940–15957.

Zor, T., & Selinger, Z. (1996). Linearization of the Bradford Protein Assay Increases Its Sensitivity: Theoretical and Experimental Studies. *Analytical Biochemistry*, *236*(2), 302–308.

VIII. Appendices

Appendix I. Plasmid map of pM268 containing ZnT8cR cDNA.

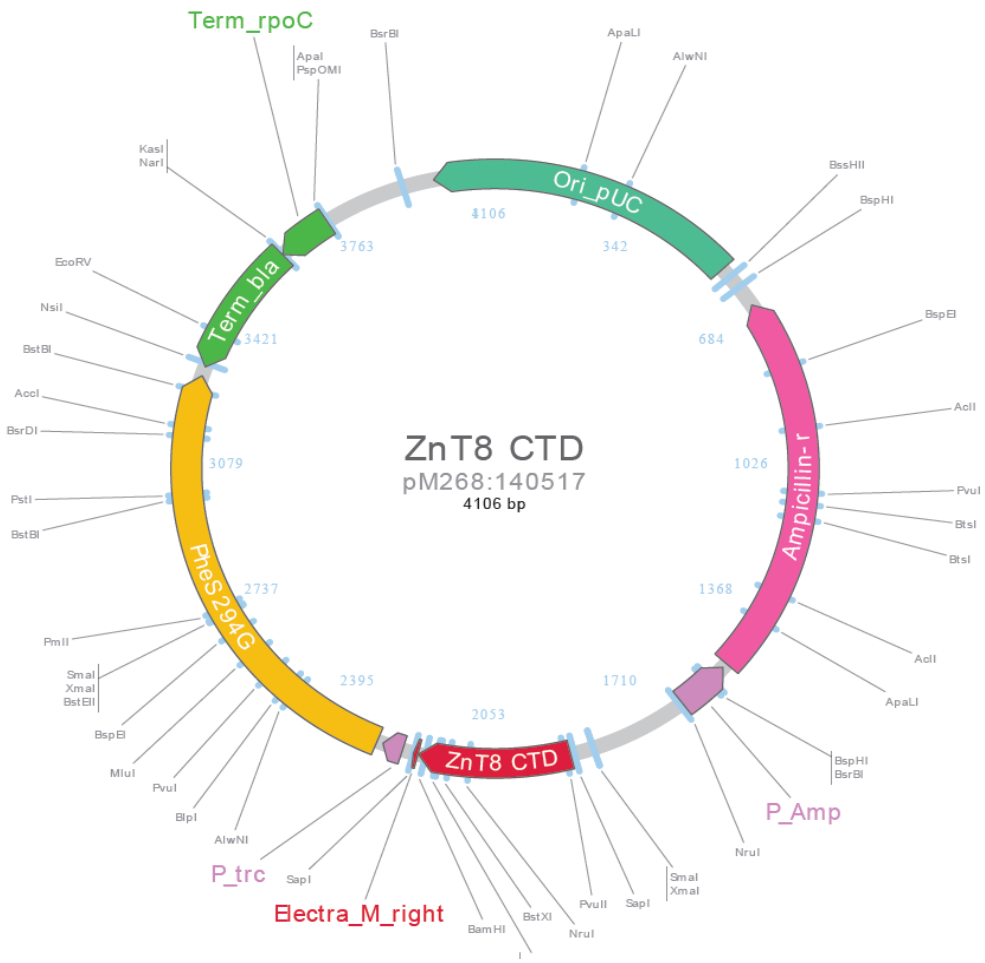

Appendix II. Plasmid map of pET6H. pET6H is derived from pET11d (Novagen), containing a 6xHis tag upstream of the gene of interest.

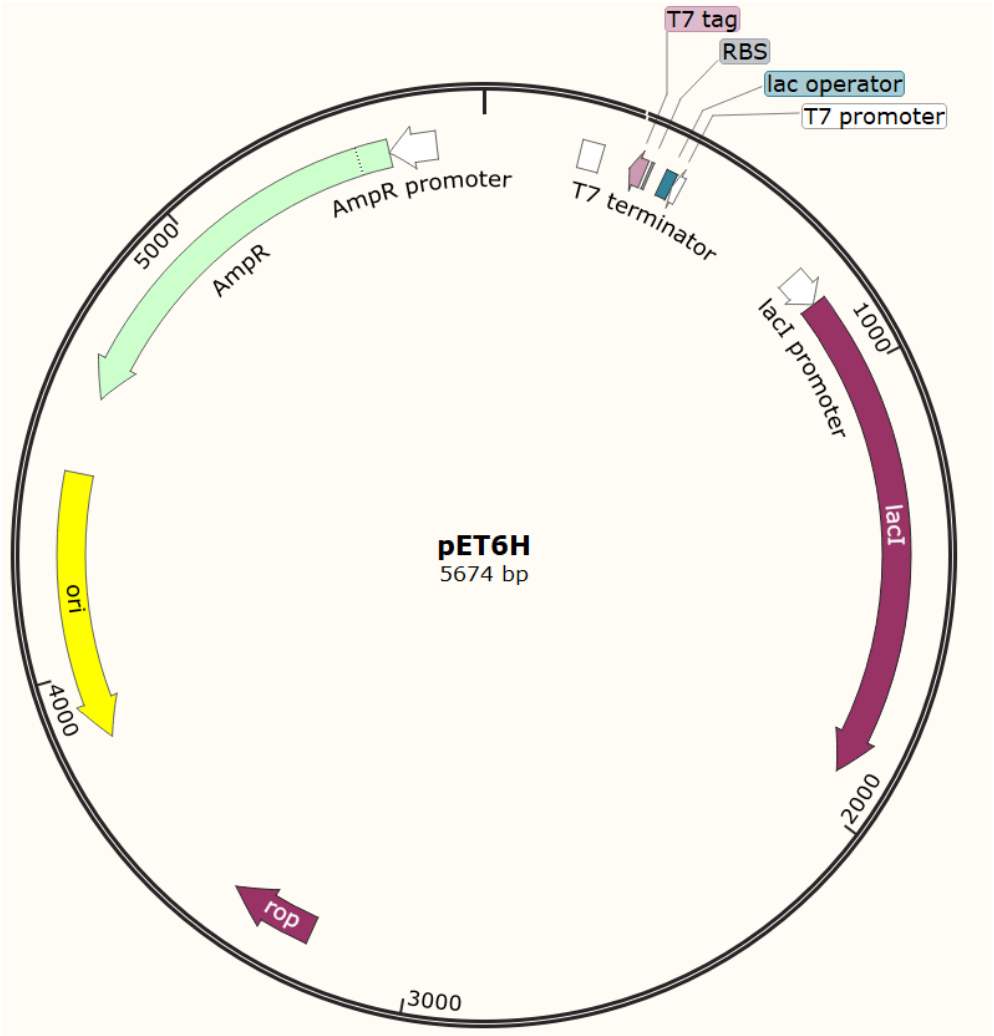

Appendix III. Protein encoded by pET6H-TEV-ZnT8cR. His tag highlighted in blue, TEV protease site in green, start of ZnT8c sequence in grey, and residue 325 in yellow.

```
                        atgcatcaccatcaccatcactcgaccgaaaacctgtat
                         M  H  H  H  H  H  H  S  T  E  N  L  Y
tttcagggcctgaaagactttagcattctgttgatggaaggtgtgccgaaaagcctgaac
 F  Q  G  L  K  D  F  S  I  L  L  M  E  G  V  P  K  S  L  N
tactctggtgtgaaagaactgattctggccgttgatggcgttctgagcgtccactccctg
 Y  S  G  V  K  E  L  I  L  A  V  D  G  V  L  S  V  H  S  L
catatctggagcctgacgatgaatcaagtcatcctgagcgcacatgttgcgaccgcagcg
 H  I  W  S  L  T  M  N  Q  V  I  L  S  A  H  V  A  T  A  A
agccgtgacagccaagtggtccgccgtgagatcgcgaaggctctgagcaagtccttcacc
 S  R  D  S  Q  V  V  R  R  E  I  A  K  A  L  S  K  S  F  T
atgcacagcctgaccattcagatggagtcgccggttgatcaggacccggattgtctgttc
 M  H  S  L  T  I  Q  M  E  S  P  V  D  Q  D  P  D  C  L  F
tgcgaggatccgtgcgactaa
 C  E  D  P  C  D  -
```

Appendix IV. Protein encoded by pET6H-TEV-ZnT8cW. His tag highlighted in blue, TEV protease site in green, start of ZnT8c sequence in grey, and residue 325 in yellow.

```
                          atgcatcaccatcaccatcactcgaccgaaaacctgtat
                           M  H  H  H  H  H  H  S  T  E  N  L  Y
tttcagggcctgaaagactttagcattctgttgatggaaggtgtgccgaaaagcctgaac
 F  Q  G  L  K  D  F  S  I  L  L  M  E  G  V  P  K  S  L  N
tactctggtgtgaaagaactgattctggccgttgatggcgttctgagcgtccactccctg
 Y  S  G  V  K  E  L  I  L  A  V  D  G  V  L  S  V  H  S  L
catatctggagcctgacgatgaatcaagtcatcctgagcgcacatgttgcgaccgcagcg
 H  I  W  S  L  T  M  N  Q  V  I  L  S  A  H  V  A  T  A  A
agccgtgacagccaagtggtccgccgtgagatcgcgaaggctctgagcaagtccttcacc
 S  W  D  S  Q  V  V  R  R  E  I  A  K  A  L  S  K  S  F  T
atgcacagcctgaccattcagatggagtcgccggttgatcaggacccggattgtctgttc
 M  H  S  L  T  I  Q  M  E  S  P  V  D  Q  D  P  D  C  L  F
tgcgaggatccgtgcgactaa
 C  E  D  P  C  D  -
```

Appendix V. Protein encoded by pET6H-WELQ-ZnT8cR. His tag highlighted in blue, WELQ protease site in green, start of ZnT8c sequence in grey, and residue 325 in yellow.

```
                                        atgcatcaccatcaccatcactgggaattg
                                         M  H  H  H  H  H  H  W  E  L
cagctgaaagactttagcattctgttgatggaaggtgtgccgaaaagcctgaactactct
 Q  L  K  D  F  S  I  L  L  M  E  G  V  P  K  S  L  N  Y  S
ggtgtgaaagaactgattctggccgttgatggcgttctgagcgtccactccctgcatatc
 G  V  K  E  L  I  L  A  V  D  G  V  L  S  V  H  S  L  H  I
tggagcctgacgatgaatcaagtcatcctgagcgcacatgttgcgaccgcagcgagccgt
 W  S  L  T  M  N  Q  V  I  L  S  A  H  V  A  T  A  A  S  R
gacagccaagtggtccgccgtgagatcgcgaaggctctgagcaagtccttcaccatgcac
 D  S  Q  V  V  R  R  E  I  A  K  A  L  S  K  S  F  T  M  H
agcctgaccattcagatggagtcgccggttgatcaggacccggattgtctgttctgcgag
 S  L  T  I  Q  M  E  S  P  V  D  Q  D  P  D  C  L  F  C  E
gatccgtgcgactaa
 D  P  C  D  -
```

Appendix VI. Full-length SLC30A8 cDNA sequences encoding wild-type (R325) ZnT8 and the common rs13266634 mutation causing W325.

```
SLC30A8-R325    ATGGAGTTTCTTGAAAGAACGTATCTTGTGAATGATAAAGCTGCCAAGATGTATGCTTTC    60
SLC30A8-W325    ATGGAGTTTCTTGAAAGAACGTATCTTGTGAATGATAAAGCTGCCAAGATGTATGCTTTC    60
                ************************************************************

SLC30A8-R325    ACACTAGAAAGTGTGGAACTCCAACAGAAACCGGTGAATAAAGATCAGTGTCCCAGAGAG    120
SLC30A8-W325    ACACTAGAAAGTGTGGAACTCCAACAGAAACCGGTGAATAAAGATCAGTGTCCCAGAGAG    120
                ************************************************************

SLC30A8-R325    AGACCAGAGGAGCTGGAGTCAGGAGGCATGTACCACTGCCACAGTGGCTCCAAGCCCACA    180
SLC30A8-W325    AGACCAGAGGAGCTGGAGTCAGGAGGCATGTACCACTGCCACAGTGGCTCCAAGCCCACA    180
                ************************************************************

SLC30A8-R325    GAAAAGGGGGCGAATGAGTACGCCTATGCCAAGTGGAAACTCTGTTCTGCTTCAGCAATA    240
SLC30A8-W325    GAAAAGGGGGCGAATGAGTACGCCTATGCCAAGTGGAAACTCTGTTCTGCTTCAGCAATA    240
                ************************************************************

SLC30A8-R325    TGCTTCATTTTCATGATTGCAGAGGTCGTGGGTGGGCACATTGCTGGGAGTCTTGCTGTT    300
SLC30A8-W325    TGCTTCATTTTCATGATTGCAGAGGTCGTGGGTGGGCACATTGCTGGGAGTCTTGCTGTT    300
                ************************************************************

SLC30A8-R325    GTCACAGATGCTGCCCACCTCTTAATTGACCTGACCAGTTTCCTGCTCAGTCTCTTCTCC    360
SLC30A8-W325    GTCACAGATGCTGCCCACCTCTTAATTGACCTGACCAGTTTCCTGCTCAGTCTCTTCTCC    360
                ************************************************************

SLC30A8-R325    CTGTGGTTGTCATCGAAGCCTCCCTCTAAGCGGCTGACATTTGGATGGCACCGAGCAGAG    420
SLC30A8-W325    CTGTGGTTGTCATCGAAGCCTCCCTCTAAGCGGCTGACATTTGGATGGCACCGAGCAGAG    420
                ************************************************************

SLC30A8-R325    ATCCTTGGTGCCCTGCTCTCCATCCTGTGCATCTGGGTGGTGACTGGCGTGCTAGTGTAC    480
SLC30A8-W325    ATCCTTGGTGCCCTGCTCTCCATCCTGTGCATCTGGGTGGTGACTGGCGTGCTAGTGTAC    480
                ************************************************************

SLC30A8-R325    CTGGCATGTGAGCGCCTGCTGTATCCTGATTACCAGATCCAGGCGACTGTGATGATCATC    540
SLC30A8-W325    CTGGCATGTGAGCGCCTGCTGTATCCTGATTACCAGATCCAGGCGACTGTGATGATCATC    540
                ************************************************************

SLC30A8-R325    GTTTCCAGCTGCGCAGTGGCGGCCAACATTGTACTAACTGTGGTTTTGCACCAGAGATGC    600
SLC30A8-W325    GTTTCCAGCTGCGCAGTGGCGGCCAACATTGTACTAACTGTGGTTTTGCACCAGAGATGC    600
                ************************************************************

SLC30A8-R325    CTTGGCCACAATCACAAGGAAGTACAAGCCAATGCCAGCGTCAGAGCTGCTTTTGTGCAT    660
SLC30A8-W325    CTTGGCCACAATCACAAGGAAGTACAAGCCAATGCCAGCGTCAGAGCTGCTTTTGTGCAT    660
                ************************************************************

SLC30A8-R325    GCCCTTGGAGATCTATTTCAGAGTATCAGTGTGCTAATTAGTGCACTTATTATCTACTTT    720
SLC30A8-W325    GCCCTTGGAGATCTATTTCAGAGTATCAGTGTGCTAATTAGTGCACTTATTATCTACTTT    720
                ************************************************************

SLC30A8-R325    AAGCCAGAGTATAAAATAGCCGACCCAATCTGCACATTCATCTTTTCCATCCTGGTCTTG    780
SLC30A8-W325    AAGCCAGAGTATAAAATAGCCGACCCAATCTGCACATTCATCTTTTCCATCCTGGTCTTG    780
                ************************************************************

SLC30A8-R325    GCCAGCACCATCACTATCTTAAAGGACTTCTCCATCTTACTCATGGAAGGTGTGCCAAAG    840
SLC30A8-W325    GCCAGCACCATCACTATCTTAAAGGACTTCTCCATCTTACTCATGGAAGGTGTGCCAAAG    840
                ************************************************************

SLC30A8-R325    AGCCTGAATTACAGTGGTGTGAAAGAGCTTATTTTAGCAGTCGACGGGGTGCTGTCTGTG    900
SLC30A8-W325    AGCCTGAATTACAGTGGTGTGAAAGAGCTTATTTTAGCAGTCGACGGGGTGCTGTCTGTG    900
                ************************************************************

SLC30A8-R325    CACAGCCTGCACATCTGGTCTCTAACAATGAATCAAGTAATTCTCTCAGCTCATGTTGCT    960
SLC30A8-W325    CACAGCCTGCACATCTGGTCTCTAACAATGAATCAAGTAATTCTCTCAGCTCATGTTGCT    960
                ************************************************************

SLC30A8-R325    ACAGCAGCCAGCCGGGACAGCCAAGTGGTTCGGAGAGAAATTGCTAAAGCCCTTAGCAAA    1020
SLC30A8-W325    ACAGCAGCCAGCTGGGACAGCCAAGTGGTTCGGAGAGAAATTGCTAAAGCCCTTAGCAAA    1020
                ************ ************************************************

SLC30A8-R325    AGCTTTACGATGCACTCACTCACCATTCAGATGGAATCTCCAGTTGACCAGGACCCCGAC    1080
SLC30A8-W325    AGCTTTACGATGCACTCACTCACCATTCAGATGGAATCTCCAGTTGACCAGGACCCCGAC    1080
                ************************************************************

SLC30A8-R325    TGCCTTTTCTGTGAAGACCCCTGTGACTAG            1110
SLC30A8-W325    TGCCTTTTCTGTGAAGACCCCTGTGACTAG            1110
                ******************************
```

Appendix VII. Alignment of primary sequences of *H. sapiens* ZnT8cR (residues 267-369) and the CTD of *T. thermophilus* CzrB (residues 199-284) used for 3D homology modelling in SWISS-MODEL. Identical residues are marked with a star.

```
ZnT8cR    LKDFSILLMEGVPKSLNYSGVKELILAV-DGV-LSVHSLHIWSLTMNQVILSAHVATAAS
CzrB(3byr)-------LMDEGLPPEEVERIRAFLQERIRGRALEVHDLKTRRAG-PRSFLEFHLVVRGD
                  **                      *  * ** *           *  *
ZnT8cR    R---DSQVVRREIAKALSKSFTMHSLTIQMESPVDQDPDCLFCEDPCD
CzrB(3byr)TPVEEAHRLCDELERALAQAFPGLQATIHVEPEG--------------
                     *   **   *     **  *
```

Appendix VIII. Longer induction time improves ZnT8c protein yield. Size exclusion chromatograms of affinity purified ZnT8cW protein expressed in SoluBL™ *E. coli* following 18 h (dotted line) or 42 h (solid line) induction with 0.5 mM IPTG at 16 °C at 200 rpm on an orbital shaker. Both samples had major peaks at 41 and 71 min, corresponding to proteins with mass >70 and ~34 kDa respectively. Similar results were obtained with ZnT8cR.

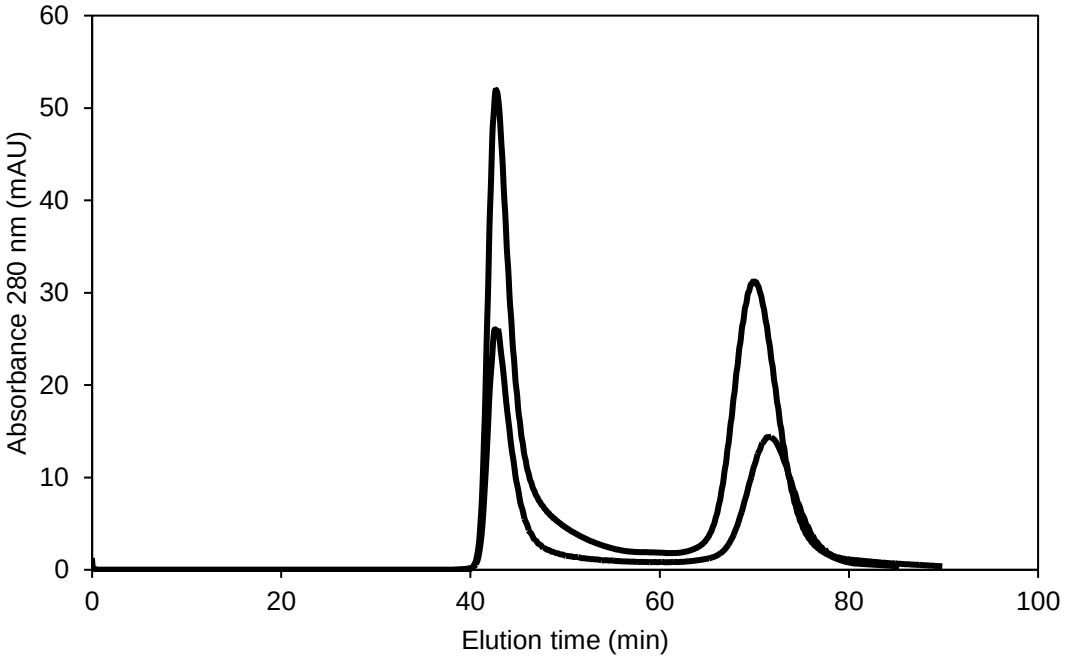

Appendix IX. Double colony selection expression tests using SoluBL21™ *E. coli*. Three or four single colonies were picked from LB agar plates inoculated with SoluBL21™ cells transformed with pET6H-TEV-ZnT8cR or pET6H-TEV-ZnT8cW. LB medium bacterial cultures were grown from these single colonies to an OD_{600} of 0.6 and then induced with 0.5 mM IPTG overnight at 16 °C at 200 rpm on an orbital shaker. Total protein expression was analysed by taking an aliquot from each sample and resuspending the bacterial pellet in 2x Laemmli sample buffer. Protein samples were separated by SDS-PAGE and stained using Coomassie R250. Lanes R_1-R_4 contain total protein extracted from bacteria expressing ZnT8cR. Lanes W_1-W_3 contain total protein extracted from bacteria expressing ZnT8cW. The image quality is poor – visually the R_2 and W_2 cultures gave the strongest signal. This experiment was not repeated (n = 1).

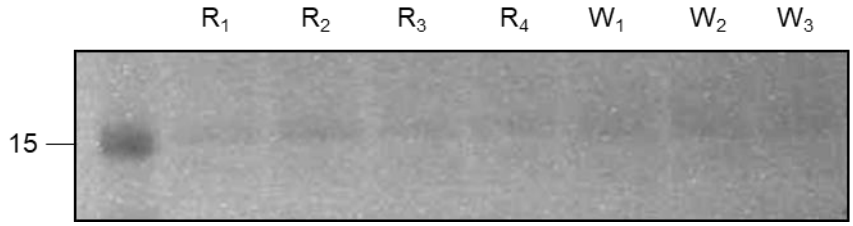

Appendix X. SoluBL21™ *E. coli* datasheet.

SoluBL21™

Competent *E. coli* Kits

amsbio

Cat. #	Contents	Quantity
C700200	SoluBL21™ Chemically Competent *E. coli*	10 x 50 µl
	SOC Medium	6.0 ml
	pUC19 Positive Control Plasmid	20 µl (500 pg/µl)
C700210	SoluBL21™ Electrocompetent *E. coli*	10 x 20 µl
	SOC Medium	6.0 ml
	pUC19 Positive Control Plasmid	20 µl (10 pg/µl)

Shipping	Shipped on Dry Ice
Storage	Store the SoluBL21 kit at -70°C. The SOC Medium may be stored at 4 °C. Stable for 6 months.

Related Products	Catalog #
SoluLyse™ Bacterial Protein Extraction Reagent (Phosphate Buffer)	L100125 (125 ml); L100500 (500 ml)
SoluLyse™ Bacterial Protein Extraction Reagent (Tris Buffer)	L200125 (125 ml); L200500 (500 ml)
EZ-Spread ™ Beads, Single-Use Tubes	C400050 (50 tubes)
EZ-Spread ™ Beads, Dispenser Bottle	C400100 (1 bottle)
TurboCells® Competent *E. coli*	C300020 (20 x 50 µl)
TurboCells® BL21(DE3) Competent *E. coli*	C302020 (20 x 50 µl)
TurboCells® BL21(DE3) pLysS Competent *E. coli*	C303020 (20 x 50 µl)
SmartCells™ Competent *E. coli*	C101020 (20 x 50 µl)

Introduction: The low cost and convenience of expressing mammalian proteins in *E. coli* make this host bacterium an important tool for life science applications. However, a major obstacle faced by scientists using *E. coli* expression strains, such as BL21(DE3), is the high percentage of mammalian proteins that are expressed in an insoluble form. Different approaches to dealing with protein insolubility in *E. coli*, such as lowering expression temperature, changing promoters, adding purification tags, using alternative media, or protein re-folding work only in some cases and at a high cost in time, effort, and complications. With the SoluBL21 Competent *E. coli*, Genlantis scientists have used a novel directed evolution approach to create a significantly improved BL21(DE3) host strain. With this mutant strain, users will significantly improve their chances of obtaining partially or fully soluble proteins in the majority of expression experiments. Even in cases where partial solubility is achieved, users can obtain sufficient amounts of protein by simply increasing the size of their culture. With the new Genlantis SoluBL21 strain, a major obstacle to soluble protein expression in *E. coli* has been overcome for many mammalian proteins. This significant improvement should enable users to make progress in a wide range of applications more quickly and far less expensively than in the past.

SoluBL21™ Strain: F- *ompT hsdS*$_B$ (r_B^- m_B^-) *gal dcm* (DE3)†	
DE3	Encodes T7 lysogen for T7 RNA polymerase for high-level transcription
ompT	Deficient in the OmpT protease, resulting in a higher yield of intact recombinant proteins
hsd SB (r_B^- m_B^-)	Improved transformation efficiencies and representations of methylated DNA

† *The SoluBL21 strain contains uncharacterized mutations obtained through special selection criteria. These mutations make the strain able to express insoluble proteins in soluble form, fully or partially, in most tests conducted.*

METHODS AND PROCEDURES

A. General Notes

The SoluBL21 transformation efficiency is ≥ 10^6 cfu/µg for chemically competent cells, and ≥ 10^{10} cfu/µg for Electrocompetent cells. We recommend testing efficiency by using 2 µl of the pUC19 Positive Control Plasmid per transformation reaction. Plate transformation mix on LB agar with 100 µg/ml carbenicillin.

B. Media Preparation

Protein expression in the SoluBL21 *E. coli* is optimized for use with M9 Minimal Media (M9). Prepare the M9 media as follows:

a. **Mix the M9 salts (at 1X) by combining, per liter:**

Na_2HPO_4	6 g
KH_2PO_4	3 g
NaCl	0.5 g
NH_4Cl	1 g
Water	up to 800 ml

b. **Filter sterilize or autoclave.**
NOTE: Alternatively, make a 10X stock of M9 salts, sterilize, and store at room temperature until needed. Dilute to 1X and proceed to step c. below.

c. **Add the following sterile components (per liter):**

100 mM $CaCl_2$	1 ml
1 M $MgSO_4$	1 ml
Glycerol	0.3% final
Sterile Water	up to 1L final

UK & Rest of World
184 Milton Park, Abingdon OX14 4SE, Oxon, UK
Tel: +44 (0) 1235 828 200
Fax: +44 (0) 1235 820 482

Switzerland
Centro Nord-Sud 2E
CH-6934 Bioggio-Lugano
Tel: +41 (0) 91 604 55 22
Fax: +41 (0) 91 605 17 85

Deutschland
Bockenheimer Landstr. 17/19
60325 Frankfurt/Main
Tel: +49 (0) 69 779099
Fax: +49 (0) 69 13376880

United States
23591 El Toro Rd. Suite #147
Lake Forest, CA 92630
Tel: + 1 800 987 0985
Fax: + 1 949 265 7703

amsbio
info@amsbio.com

Appendix XI. ZnT8cW dimers did not contain a dityrosine bond. A 7 µM sample of ZnT8cW did not elicit the strong emission indicative of a dityrosine bond.

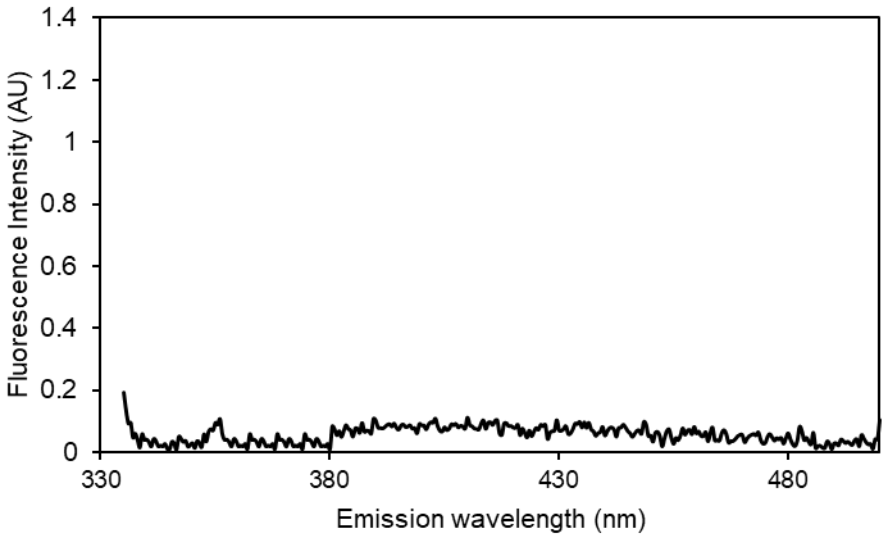

Appendix XII. Nano differential scanning fluorimetry (nDSF) measured the thermostability of the two ZnT8c variants. The first derivative of the 350/330 nm ratio accurately indicates the melting temperature of ZnT8cR (red, T_m = 43.3 ±0.1 °C) and ZnT8cW (green, T_m = 41.9 ±0.1 °C), both n = 3. This difference is significant (*p* = 0.01).

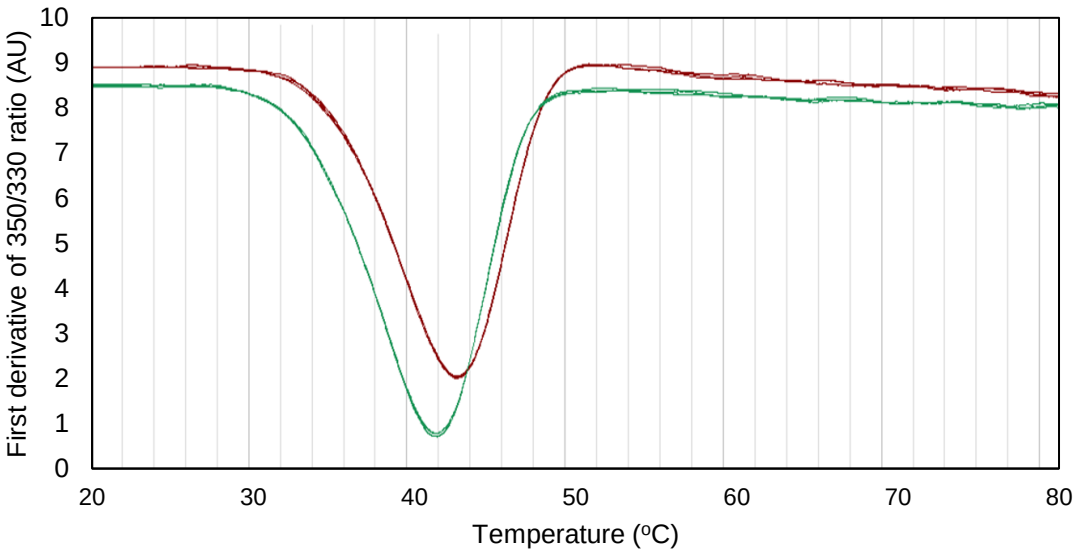

Appendix XIII. Grid scans of 80 x 20 µm oblong ZnT8cR crystal. Crystal did not diffract, so it cannot be known whether this was a protein or salt crystal.

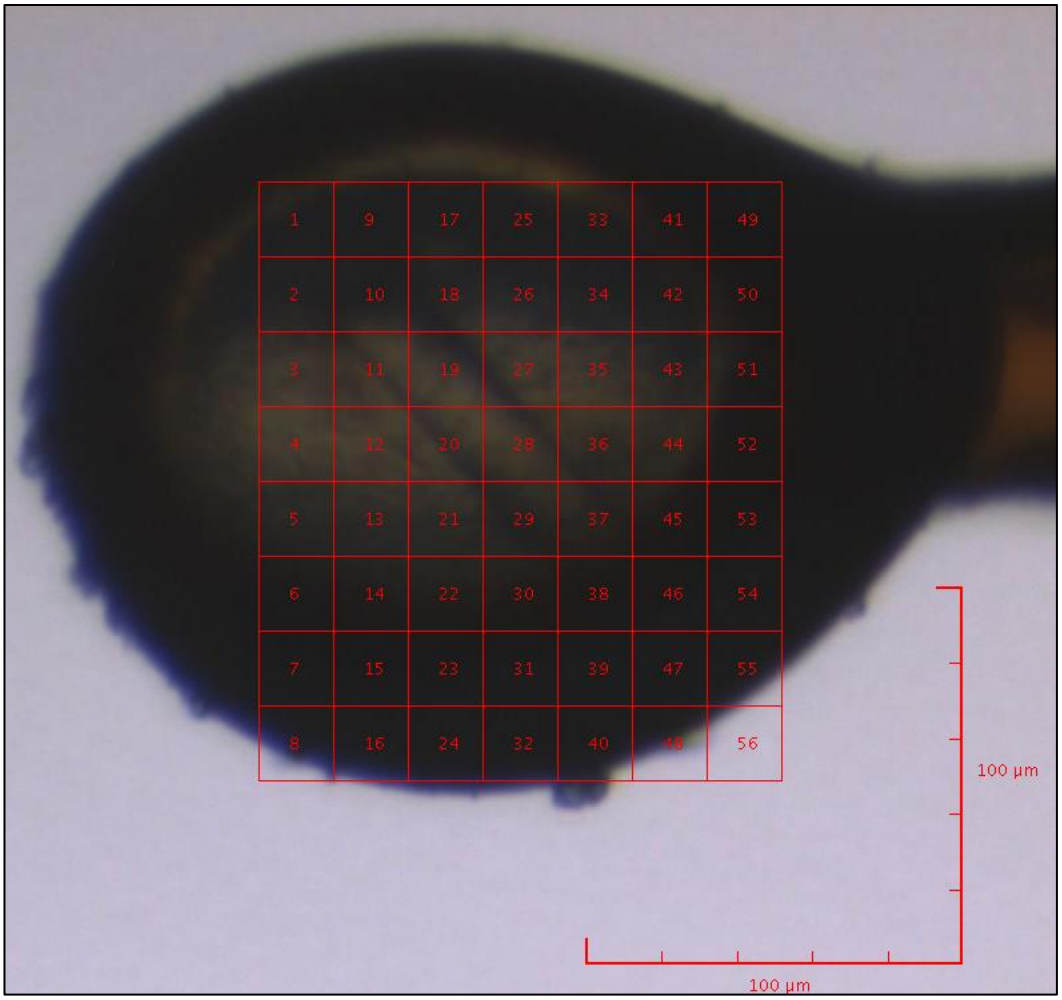

Appendix XIV. Grid scans of two drops containing approximate 5 x 5 µm square ZnT8cR crystals. Crystal did not diffract, so it cannot be known whether these were protein or salt crystals.

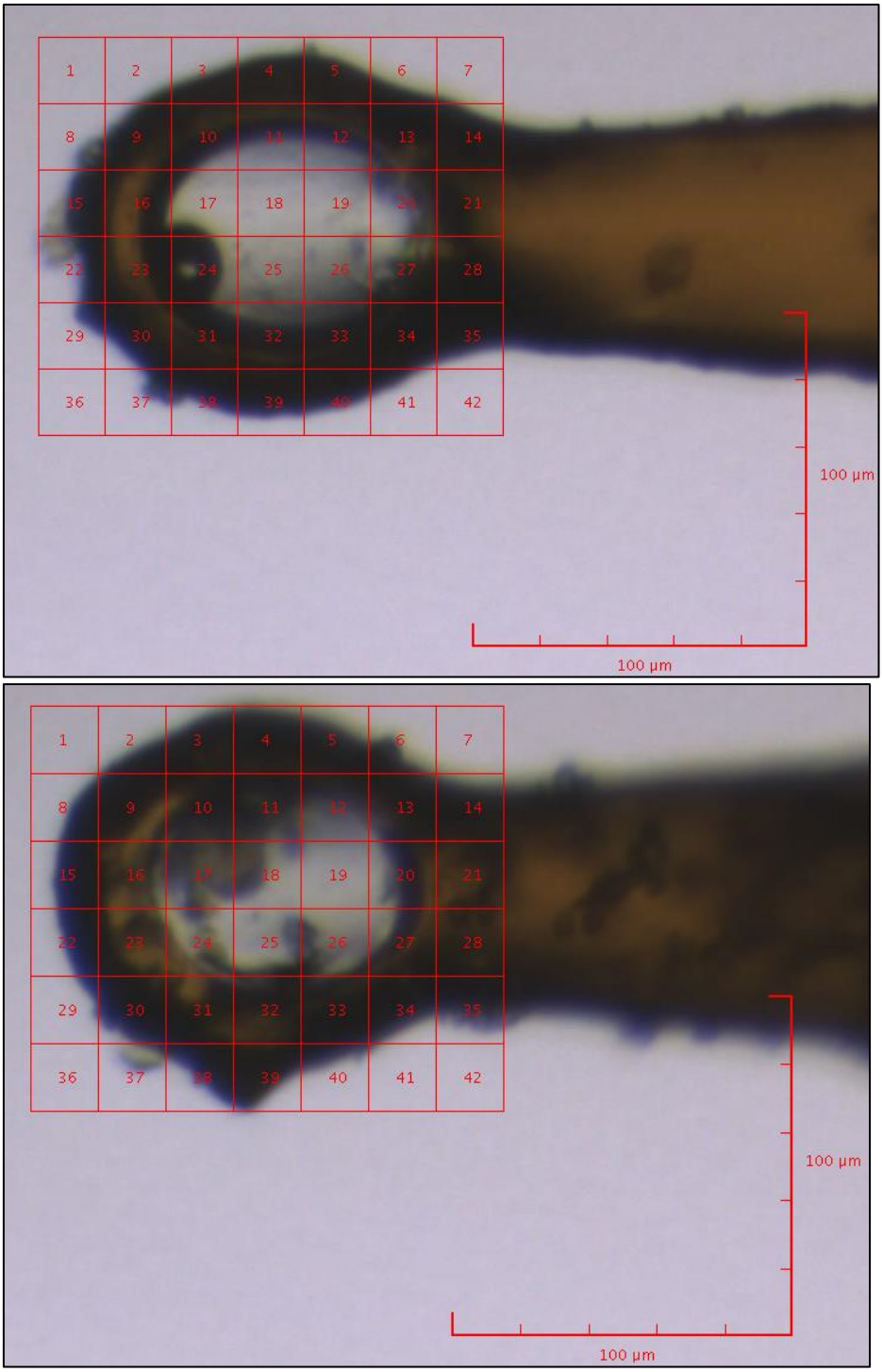

Appendix XV. ZnT8c UV absorbance is not altered by Ni^{2+} addition. Representative (n = 3) UV absorbance spectra of 35 µM of, *A*, ZnT8cR and, *B*, ZnT8cW in the absence of Ni^{2+} (blue), and with one (red) and two (green) molar equivalents of Ni^{2+}, revealed that addition of Ni^{2+} does not affect the broad peak at 320 nm. Spectra are buffer and dilution corrected.

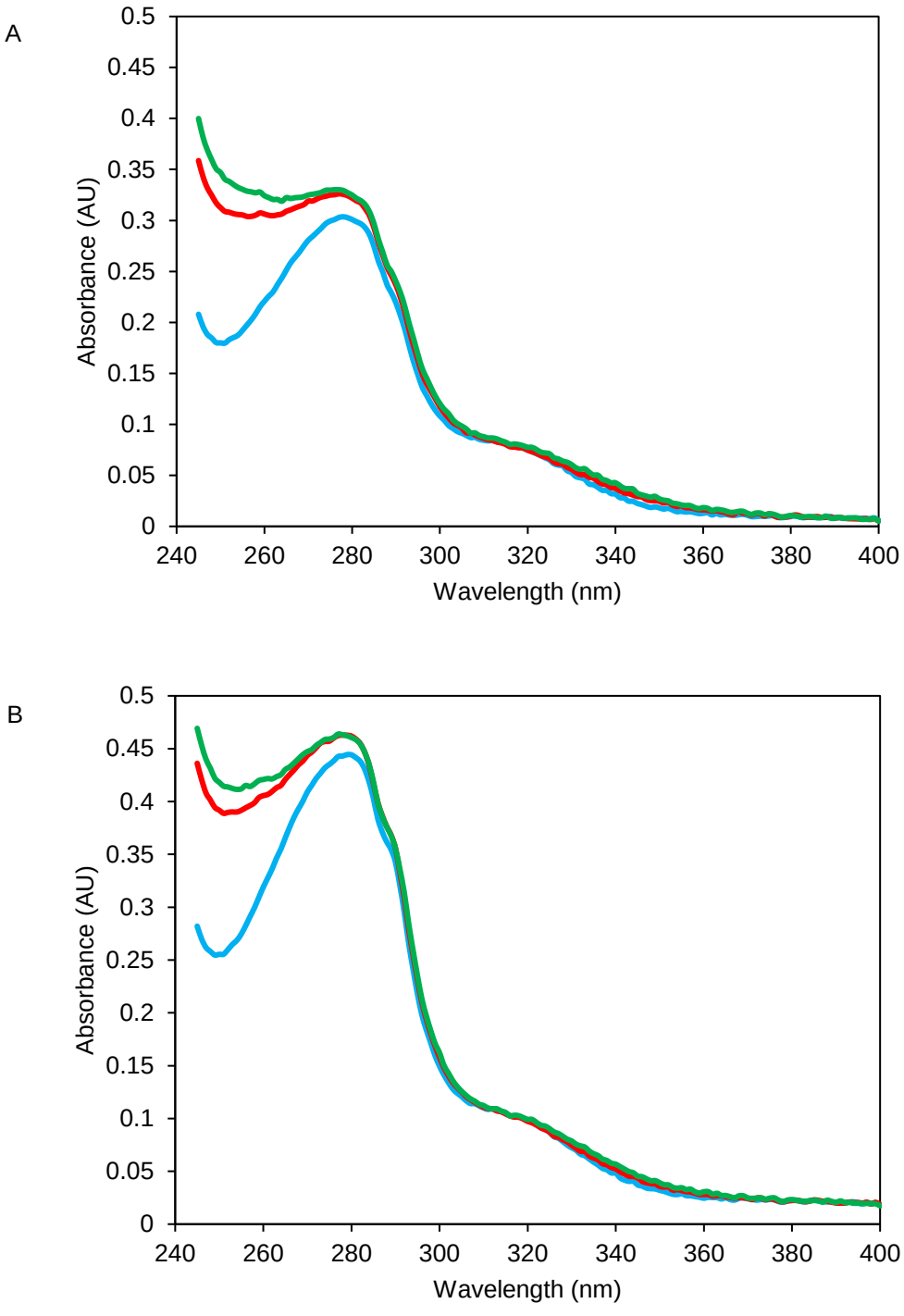

Appendix XVI. List of Publications

Parsons, Douglas S., Christer Hogstrand, and Wolfgang Maret. 2018. "The C-Terminal Cytosolic Domain of the Human Zinc Transporter ZnT8 and Its Diabetes Risk Variant." FEBS Journal 285(7):1237–50.

Carvalho, Sandra, Molina-López, Jorge, **Parsons, Douglas**, Corpe, Christopher, Maret, Wolfgang Hogstrand, Christeret al. 2017. "Differential Cytolocation and Functional Assays of the Two Major Human SLC30A8 (ZnT8) Isoforms." Journal of Trace Elements in Medicine and Biology 44:116–24.